LITHOSTRATIGRAPHY AND CLAY MINERALOGY OF PALEOCENE-EOCENE THERMAL MAXIMUM SEDIMENTS AT WILSON LAKE, NJ

By

CHRISTOPHER J. LOMBARDI

A thesis submitted to the

Graduate School-New Brunswick

Rutgers, The State University of New Jersey

in partial fulfillment of the requirements

for the degree of

Master of Science

Graduate Program in Geological Sciences

written under the direction of

Dr. Kenneth G. Miller

and approved by

_____

_____

_____

_____

New Brunswick, New Jersey

January, 2014

ABSTRACT OF THE THESIS

Lithostratigraphy and Clay Mineralogy of Paleocene-Eocene
Thermal Maximum Sediments at Wilson Lake, NJ

By: CHRISTOPHER J. LOMBARDI

THESIS DIRECTOR:

Dr. Kenneth G. Miller

The Marlboro Formation is an almost exclusively fine-grained and highly kaolinitic unit deposited during the Paleocene-Eocene Thermal Maximum (ca. 56 Ma). It presents a unique opportunity to study an exceptionally thick carbon isotope excursion and continental shelf sedimentation during a geologically brief episode of global warming. Moreover, the dominantly clayey-silt lithology is traceable over hundreds of kilometers within the Mid-Atlantic Coastal Plain physiographic province and has been drilled at numerous locations. Here, I report lithologic changes within the Marlboro Formation from a corehole at Wilson Lake, NJ to ascertain the environment of deposition and its implications for the isotopic record. Using differences in bedding character, quantified clay mineral identification, fine and coarse fraction grain size analysis, and core scanning x-ray fluorescence of major elements, I show that subtle facies changes are consistent with a shoaling depocenter that is aggrading above a modern shelf clinoform rollover.

Previous work has identified the continental shelf adjacent to the Amazon River as a possible analog for the sedimentary environment of the Marlboro Formation. Sedimentary processes and the morphology of the Amazon shelf may be similar to those that produced the Marlboro Formation. Enhanced physical weathering and continental runoff are inferred from the clay mineralogic changes in the PETM section, and are consistent with the PETM climate.

Furthermore, the Amazon experiences high rates of deposition in excess of those hypothesized for the New Jersey shelf. Particular clay minerals are also used to demonstrate increased sedimentation rates by measuring the extent of alteration caused by seawater. Rhythmic beds that have previously been interpreted as annual layers based on the periodic cycles in stable isotopes are here interpreted as sediment gravity flow deposits caused by wave-enhanced mud suspensions (fluid mud) like those documented on mud-rich shelves worldwide. The depositional model put forward here supports the extremely rapid onset to the carbon isotope excursion that has been proposed in the shallow marine environment.

Table of Contents

1. Introduction 1
2. Background in Clay Mineralogy 9
2.1 Structure of Clay Minerals 11
2.2 Origin of Clay Minerals 12
2.3 Geographic Distribution of Clay Minerals 15
2.4 Clay Peak Identification 16
2.5 Quantitative Analysis 17
3. Methods 20
3.1 Carbon Isotopes 20
3.2 Clay Mineral Analysis by X-ray Diffraction 20
3.3 Additional XRD at Rutgers 22
3.4 Grain Size Analysis 23
3.5 X-ray Fluorescence 24
3.6 Visual Descriptions 25
4. Results 27
4.1 Clay Mineral Stratigraphy 27
4.2 Saddle Ratio 28
4.3 W% Ratio 28
4.4 Clay Mineral Microstratigraphy 29
4.5 Grain size stratigraphy 29
4.6 Sortable Silt 30
4.7 X-ray Fluorescence 30
4.8 Laminae Enumeration 32
5. Discussion 34
5.1 Lithologic Succession at Wilson Lake 34
5.2 Vincentown Formation and Unit 1 Marlboro Formation 34
5.3 Unit 2 37
5.4 Unit 3 37
5.5 Sediment Distribution on the Amazon Shelf 38
5.6 Comparison to Amazon Shelf Processes 41
5.7 XRF Cyclicity 45

6. Conclusions 45
7. References 48

List of Figures

Figure 1. Map of Coreholes in the New Jersey Coastal Plain 56
Figure 2. Comparison of Regional Stratigraphy. 57
Figure 3. Vincentown, Marlboro, and Manasquan Fm. Core Photographs 58
Figure 4. Lithology of the Hornerstown, Vincentown, Marlboro, and Manasquan Formations 59
Figure 5. Clay Diffractogram 60
Figure 6. Example Grain Size Distribution. 61
Figure 7. 346-348 ft XRF Core Alignment. 62
Figure 8. Clay Mineral Stratigraphy 63
Figure 9. Clay microstratigraphy from 346-348 ft 64
Figure 10. Grain Size and Sortable Silt Depth Plot 65
Figure 11. Spectral Analysis of Iron. 66
Figure 12. Spectral Analysis of sample surface. 67
Figure 13. Barrel Sheet 310-320. 68
Figure 14. Barrel Sheet 320-330. 69
Figure 15. Barrel Sheet 330-340. 70
Figure 16. Barrel Sheet 340-350. 71
Figure 17. Barrel Sheet 350-360 72
Figure 18. Barrel Sheet 360-370. 73
Figure 19. Couplet Thickness Frequency Distribution 74
Figure 20. Determination of Depositional Units 75
Figure 21. Vincentown Formation / Marlboro Formation Contact 76
Figure 22. Regional Comparison of Clay and Isotopic Records 77
Figure 23. Mud-dominated Shelf Classification 78
Figure 24. Muddy Shelf Depositional Models 79
Figure 25. Isopach Map of Marlboro Formation in the Salisbury Embayment. 80
Figure 26. Amazon Shelf Sedimentary Facies 81
Figure 27. Amazon Shelf Processes 82

Figure 28. Convoluted bedding at Ancora 83

List of Tables

Table 1. XRF Correlation Matrix……..……84

1. Introduction

The earliest Eocene is of intense stratigraphic interest due to an abrupt carbon isotope excursion (CIE) and associated Paleocene-Eocene Thermal Maximum (PETM) that represents a major carbon cycle perturbation and response by climate. The CIE, a decrease found in the average $\delta^{13}C$ values of foraminifera, paleosols, bulk samples, etc., is preserved worldwide in deep-sea (-2.75‰; Kennett and Stott, 1991), shallow marine (-6‰; Wilson Lake, NJ)(Cramer et al., 1999; Zachos et al., 2006; Sluijs et al., 2007; Wright and Schaller, 2013; Fig. 1), and terrestrial records (-7.6‰; Koch et al., 1992; Bowen et al., 2001; Wing et al., 2005). The release of significant amounts of isotopically light carbon is believed to have caused the PETM climate, one of the warmest known intervals of the Cenozoic, with temperature increases of 5°C at equatorial latitudes (Zachos et al., 2003) and 5° to 8°C nearer the poles (Sluijs et al., 2006). A record of the CIE is preserved in New Jersey in the terrestrially derived clays and silts of the Marlboro Formation (e.g., Kopp et al., 2009).

The CIE is subdivided into intervals originally described from Ocean Drilling Program (ODP) Sites 690 and 1266 (Kennet and Stott, 1991; Röhl et al., 2007; Murphy et al., 2010). Lithologically, the deep-sea cores contain a clay layer that corresponds to a carbonate dissolution interval, with carbonate ooze only preserved above and below (Röhl et al., 2007). The isotopic signal of the CIE is divided in 4 parts. The “onset” is marked by the first decrease in $\delta^{13}C$ which is typically abrupt in deep-sea cores, but can be gradual in shallow settings (Sluijs et al., 2007; Wright and Schaller, 2013). This onset was used to place the stratotype for the Paleocene/Eocene boundary (Aubry et al., 2007). The “core,” is defined by the interval of sustained minimum values and is mostly confined to the dissolution interval in the deep sea (Röhl et al., 2007). By contrast, the “core” extends beyond the dissolution interval in shallow

marine settings. The steeply sloped “recovery I” and gradual “recovery II” phases culminate with the return to pre-CIE values. Much of the CIE’s expression depends on local sedimentation and the tempering effect of ocean-atmosphere carbon exchange.

Though the onset of the CIE appears geologically rapid, time constraints on the “core” and recovery phases are essential to interpreting the PETM. Initial time limits < 200 kyr were derived from the deep sea, but recent determinations of duration are shorter. Estimates from cycle stratigraphy in ODP Leg 208 cores show that the complete CIE is contained within < 9 precessional Milankovitch cycles, yielding ~170 kyr duration (Röhl et al., 2007). Likewise, reports from ODP Leg 171B, Site 1051 show a benthic foraminiferal extinction event and intermediate water warming occurring in 5000-7000 yrs after the onset, followed by a ~140 kyr recovery (Katz et al., 1999). The “core” is estimated to be on the order of 60-70 kyr at Sites 1266 and 690 (Röhl et al., 2007). At Site 1266 measurements of extraterrestrial ^{3}He concentration, a proxy for sedimentation rates, suggest a 113 kyr “core,” and total duration of ~230 kyr (Murphy et al., 2010). Identifying the magnitude of carbon released, the source, and the drawdown rate of the global carbon cycle, all depend on correct determination of the duration of the CIE.

Proposed mechanisms for the PETM need to accurately identify a carbon reservoir, isotopically depleted in ^{13}C, and of appropriate size that exchanges with the atmosphere and deep-sea on predicted timescales. One or more of the following mechanisms may have triggered or reinforced the PETM climate. Methane clathrate (-60‰) destabilization in the deep-sea has been put forward as a possible source, if warming oceans or the removal of sedimentary overburden triggered them to melt (Dickens et al., 1995). However, the estimated mass of Paleocene clathrates (1000 Gt C; Buffett and Archer, 2004) is only a fraction of that

needed to cause the CIE (4300 Gt C; Dickens et al., 1997). Emplacement of the North Atlantic Igneous Province may have caused the release of ^{12}C-enriched carbon by the sudden creation of thermogenic methane (1500 Gt C; $\delta^{13}C$= -35‰ to -50‰; Svensen et al., 2004). The absolute ages of these magma intrusions imaged in seismic sections, thought to contain carbon-rich strata, have $^{40}Ar/^{39}Ar$ dates that cluster around the PETM (Storey et al., 2007). The hypothesized desiccation of a small ocean by tectonic uplift and bacterial oxidation of organics could produce a CIE (5000 Gt C; Higgins and Schrag, 2006), but there is little evidence to support this hypothesis. Next, orbitally forced melting of circum-arctic and Antarctic permafrost has the potential to explain PETM warming as well as subsequent hyperthermals of the early Eocene (DeConto et al., 2012). Also, carbon-dioxide degassing associated with the emplacement of a kimberlite pipe cluster is a recent explanation (Patterson and Francis, 2013). Another large ^{12}C source, that of a bolide impact, also explains magnetic nannoparticles that can form in the ensuing condensate cloud and are found in the Marlboro Formation (Kent et al., 2003). Further work on these particles has also implicated a biologic origin in the presence of water column or sediment anoxia (Kopp et al., 2009; 2007). Either source could account for the presence of the magnetic particles, but the condensate cloud model accounts for aspects of particle size and arrangement the biogenic model may not (Wang et al., 2013).

Sediments belonging to the Marlboro Formation are found throughout the Salisbury Embayment (southeast Virginia, the Delmarva Peninsula, and southern New Jersey), though nomenclature varies between states. Upper Paleocene deposits are assigned to the Vincentown Formation in the northern part of the basin (i.e., NJ), but the the Aquia Formation in the southern part (Fig. 2). The Aquia Formation is typically shelly, glauconitic, quartz sand and silt (Kopp et al., 2009), whereas the Vincentown Formation in the subsurface is described as micaceous, glauconitic, quartzose, sandy clayey silt (Millville; Sugarman et al., 2005) to a clayey

glauconite-quartz sand in outcrop (Medford; Sugarman et al., 2010). Lower Eocene deposits are assigned to the Nanjemoy Formation, a glauconitic silty to clayey quartz sand (Kopp et al., 2009) in the south and the Manasquan Formation, a dark greenish gray carbonate-rich clay with sparse glauconite, in New Jersey (Sugarman et al., 2005).

At many New Jersey Coastal Plain (NJCP) sites, a thick (≤15 m) and very fine-grained unit is found between the Vincentown and Manasquan Formations. It was referred to as the Marlboro Clay (Kopp et al., 2009), a formation that was originally defined in Maryland (Glaser, 1971). The use of the term Marlboro Formation (Fig. 2) is adopted for New Jersey to facilitate comparison with Virginia, Maryland, and Delaware. The Marlboro Formation is a pink to gray kaolinitic clayey silt, which may be slightly sandy or micaceous updip, and with low carbonate content (<5%; Wright and Schaller, 2013). Outcrop sections in Virginia contain interbedded fine silts that are ripple cross-laminated, with some scour and fill channels present (Mixon et al., 2000). More basinward sites present a gray clayey silt that is superficially homogenous, but actually contains laminations and thin beds. The South Dover Bridge core in MD is reported to contain finely disseminated specks of pyrite (Self-Trail et al., 2012) that is consistent with the pyrite at Wilson Lake.

The contact between the underlying Aquia-Vincentown and Marlboro Formation is frequently interpreted as disconformable in outcrop, though many core sections appear gradational (Gibson et al., 2000). The base of the Eocene is defined by the onset of the CIE (Aubry et al., 2007) which is located at about 370 ft (112.78 m) within the Vincentown Formation at Wilson Lake B (Fig. 2). This, and the presence of Vincentown Formation lithology above the Marlboro Formation at some sites (Ancora and Millville; Sugarman et al., 2005; 2010),

makes them inextricably linked. The upper contact of the Marlboro Formation with overlying units is disconformable (e.g., Gibson et al., 2000).

The outer neritic response to transient PETM warming was first described in NJ at Bass River, by integrating sequence stratigraphy, nannofossil and microfossil biostratigraphy, lithostratigraphy, and clay mineralogy (Cramer et al., 1999). The sediments of the Marlboro Formation at Bass River are interpreted as preserving the $\delta^{13}C$ onset, core, and some of the recovery of the CIE, whereas the recovery is truncated or entirely absent at Wilson Lake A (Stassen et al., 2012). Still, the Wilson Lake A core has furnished several studies that facilitate correlation with other holes. Sluijs et al. (2007) have proposed that an isotopic precursor and *Apectodinium* acme at Wilson Lake, indicates bottom water warming may have preceded the largest carbon isotope shift. Stassen et al. (2012) described a change from permanent dysoxia to seasonal dysoxia in the Marlboro Formation from Wilson Lake A and Bass River based on changing benthic foraminiferal and dinocyst abundances. Zachos et al. (2006) reported paleotemperature from TEX_{86} and $\delta^{18}O$ suggesting sea surface temperatures (SST) increased from 25° to 33° C, though new data from Millville support slightly cooler temperatures (Makarova et al., 2013). Using the TEX_{86} results to approximate $\delta^{18}O$ changes suggests a possible decrease in sea surface salinity consistent with an increase in regional runoff and precipitation (Zachos et al., 2006; Makarova et al., 2013). Clay mineral records for nearby Clayton and downdip Bass River sites confirm environmental changes in the form of a kaolinite increase near the level of the CIE-onset (Gibson et al., 2000; Cramer et al., 1999).

The USGS Wilson Lake hole A recovered in 1999 was depleted by sampling, and the need for more core material prompted a new hole to be drilled. Wilson Lake Hole B (WL-B; Fig. 1) was drilled as a cooperative venture between the New Jersey Geologic Survey, Rutgers

University, and the Delaware Geologic Survey (DGS). Drilling began in May 2011 approximately 150 ft west of the USGS Wilson Lake hole A. Core description, core archiving, and drilling support was provided by Rutgers and DGS personnel. Project goals included the successful capture of the Paleocene-Eocene and Cretaceous-Paleogene boundaries, both met with >99% total recovery in the target intervals (Miller et al., in prep).

The Marlboro Formation (14.87 m thick), extending from 317.5 ft (96.77 m) to 366.30 ft (111.65 m) in WL-B (Figs. 3, 4), contains a kaolinitic clayey silt lithology typical of other cores recovered from New Jersey. During core splitting, thin beds bounded by darker laminations were first identified and described as couplets. Couplets consist of kaolinitic clayey silt beds, ~2 cm thick, which are bound by ~0.5 mm laminations of darker clay that is more evident in dried core. Swelling clays were recognized on the core surface during drilling, and shown to exude from the laminations when the cores were split for archive purposes. These laminations are also recognizable in older cores containing the Marlboro Formation. Wright and Schaller (2013) observed similarly rhythmic bedding in a core from Millville, NJ (ODP Leg 150X) and in an outcrop at Medford, NJ.

An alternative chronology for the PETM argues that the CIE in shelf sediments differs in timing and origin from the open ocean CIE. It is suggested that beds in the Marlboro Formation represent rapid, perhaps annual deposition, and $\delta^{18}O$ cycles across the layers reflect annual atmospheric $\delta^{18}O$ changes like those measured today (Wright and Schaller, 2013). This hypothesis requires that the CIE "core" lasted <1000 years in the continental shelf environment, with the onset occurring in <100 years, though it employs a divorced chronology that is reconcilable with deep-sea cores because of the long mixing time of the ocean (Wright and Schaller, 2013). A shorter CIE does not require injection of the same large quantities of carbon.

The clay mineral component of ocean sediment, including the Marlboro Formation, is related to the broad climate trends on nearby continents (Griffin et al., 1968), but nearshore clays can reflect local drainage changes. Mineralogic studies revealing the high kaolinite content of the Marlboro Formation were originally used to infer strong weathering and precipitation in the sediment source region during the time of deposition (Gibson et al., 1993). However, the $\delta^{18}O$ of the kaolinitic clays from Bass River, NJ indicate they formed prior to their deposition during the PETM (John et al., 2012). Exhumed Cretaceous laterite soils, from deltaic facies like the Raritan and Potomac Formations, are a likely source (Kopp et al., 2009). Kaolinite is also attributed to terrestrial sediment erosion in the shallow marine sections of the coeval Dababiya Quarry Member in Egypt (Berggren et al., 2012). Kaolinitic clays in nearshore and deep-sea deposits are too abundant and appear too abruptly relative to the onset to have been created by weathering during the PETM (John et al., 2012).

The Marlboro Formation has been incorporated into a depositional model that stresses high sedimentation rates in a suboxic environment. The "Appalachian Amazon" hypothesis (Kopp et al., 2009) suggests the Marlboro Formation was deposited on a tropical-river dominated shelf. Magnetic grains within the Marlboro Formation, though of disputed origin, are similar to those produced by magnetotactic bacteria on the Amazon shelf (Kopp et al., 2009). Their preservation has been interpreted as deposition in thick sedimentary suboxic zones (Kopp et al., 2009). High sedimentation rates and increased continental runoff are interpreted as a possible cause of increased paleoproductivity and suboxia in the water column (Lippert and Zachos, 2007). Suboxia in the inner/middle neritic shelf is a feature of the modern Amazon. The Marlboro Formation was deposited at rates high enough for the organic material (i.e., lignite) and biogenic iron minerals to be preserved.

The objective of this thesis is to describe detailed lithostratigraphic changes for the Marlboro Formation at Wilson Lake, and provide an interpretation of the depositional environment. No other coastal plain unit contains such a thickness of kaolinite and an understanding of its depositional history is crucial to contextualize an expanded (14.9 m) CIE record. Several NJCP cores of the Marlboro Formation, excluding Wilson Lake A, have clay mineralogic data. I analyzed Wilson Lake B sediments by XRD to enable further comparison among sites, describing the relative abundance of detrital clays and the degree of clay alteration around the Paleocene-Eocene boundary. Changes in energy and shoreline distance on the paleoshelf impact the silt grain size fraction which I compare for the Vincentown and Marlboro Formations. The rhythmic beds in the Marlboro Formation are investigated using their observed distribution in the core and changes in elemental concentrations, as measured by scanning X-ray Fluorescence (XRF). Collectively, these methods establish subtle changes in the kaolinitic clays at Wilson Lake indicative of distinct depositional phases. Three units are identified within the Marlboro Formation and compared to the stratigraphy and sedimentary processes of the Amazon Shelf subaqueous delta. Modern Amazon processes and morphology are an analog for the earliest Eocene New Jersey continental shelf.

2. Background in Clay Mineralogy

Sheet-like minerals of the clay mineral group are hydrous aluminosilicates that form mostly during chemical weathering. The term clay denotes not only a mineral distinction, but a size distinction, as any particle < 4 μm is "clay size." Between 2 and 4 μm, the abundance of common non-clay minerals such as physically abraded quartz, feldspar, etc. drops off sharply (Moore and Reynolds, 1997). When studying clays, particles < 2 μm are isolated from the total sample, representing only the minerals that formed at that size. Practical analysis of clay minerals encompasses other similarly sized sheet silicates of the mica and chlorite groups.

X-ray diffraction (XRD) permits the recognition of clay minerals by the predictable scattering of X-rays in a crystal structure. X-rays scatter from the interaction with the electrons around the nuclei of an atom. Electrons in the path of an X-ray absorb and reradiate energy at the same wavelength it was received, a property called coherent scattering (Moore and Reynolds, 1997). Every atom emitting spherical wavefronts of X-rays reinforces or negates the signal by constructive or destructive interference. Outgoing beams from a row of atoms advance as a line of diffracted rays whose angle is dependent on that of the incident beam. In three dimensions the diffracted beam becomes a cone of radiating beams. The strongest diffracted beam emerging from the intersection of the parallel set of beams in each cone is the one picked up and studied by the diffractometer (Moore and Reynolds, 1997).

The pattern produced by scattering in a mineral depends on the arrangement of atoms within the unit cell, unique to each mineral. The diagnostic feature of clay unit cells is the distance between layers. Using Bragg's Law (equation 1), the distance *d* between rows of atoms can be calculated trigonometrically. Bragg's Law establishes a relationship between the incident

angle of the incoming beam and the diffraction angle of the outgoing one, provided all incident beams are in phase.

Equation. 1 Bragg's Law: $2d \sin\theta = n\lambda$

Value θ represents the incident angle, known because the diffractometer is positioned to a chosen angle. The wavelength λ is known based on the method of X-ray production, and n represents how much distance there is between rows of atoms expressed as a whole number of wavelengths (Moore and Reynolds, 1997). Diffraction patterns are generated by recording the intensity of diffracted X-rays over an interval of angles θ. The emitter and receiver travel at angles to the mineral sample that relate directly to the layer spacing in the crystal structure. The angle and intensity at which peaks appear is characteristic of a specific mineral, and is related to overall abundance in the sample (Moore and Reynolds, 1997).

The series of basal spacings d(001), d(002), d(003), etc. produced on a diffractogram result from the position of atoms in clay sheets. Not all basal diffracting planes (00*l*) have the same intensity. Systematic absences and intensity variations are useful diagnostic features of each mineral. Ideally, only (00*l*) spacings contribute to the diffraction pattern, but misaligned clay particles alter the incident angle, and rigorous sample preparation is necessary to orient clay particles to the horizontal. The sharpness of a peak and proper identification depends on orientation, the quality of crystal formation, and the sufficient thickness of clay on each sample. Departure from the incident angle, caused by misaligned clay particles, produce phase differences that are more pronounced in thin samples, and peaks are broadened. Therefore, peaks get sharper as the clay sample gets thicker. Peak widths also become broader when smaller crystals become more abundant. The most common broad peaks are produced by the interstratification of different clay minerals, producing d(00*l*) that are found at the mean

average of the two individual spacings. The manifestation of background scattering also changes across a diffraction profile. Background intensity increases sharply at low 2θ angles (high d-spacings), caused by imperfect beam polarization at highly acute angles relative to the sample surface (Moore and Reynolds, 1997). Notably, this interferes with diffraction patterns of swelling clays, and produces the saddle referred to later.

2.1 Structure of Clay Minerals

Layered silicates are composed either of tetrahedral sheets linked at the corners, or octahedral sheets linked along edges. These tetrahedra are coordinated around cations of Si^{4+} (most frequent), Al^{3+}, or Fe^{3+} (least frequent). An oxygen is shared at three corners between the bases of neighboring tetrahedra, with a 4^{th} apical oxygen pointing away from the base (Moore and Reynolds, 1997). Octahedral sheets consist of edge-linked structures of oxygen (or hydroxyls) surrounding typical cations of Al^{3+}, Mg^{2+}, Fe^{2+}, and Fe^{3+}. The ratio of cations to anions determines if the mineral is considered dioctahedral or trioctahedral, a different sheet stacking arrangement caused by their respective charges.

The combination of a tetrahedral sheet and an octahedral sheet, with the apical oxygen replacing an anion at the base of the octahedral sheet, forms a 1:1 (T-O) layer silicate structure. Kaolinite and chlorite are 1:1 clays, and, lacking interlayer spaces, bond in an ongoing T-O pattern. A 2:1 (T-O-T) layer silicate is formed by the addition of an inverted tetrahedral sheet joining the other side of the octahedral sheet. The alignment of tetrahedral sheets in 2:1 clays further distinguishes different minerals. When layers stack together, cations in the top sheet are either vertically aligned or misaligned with cations in the lower sheet. Smectites have low layer charge leading to large distances between the layers and increased stacking disorder. The interlayer space of smectite attracts water and other cations, frequently potassium. Stronger

layer charges in illite collapses the hydrated interlayers forcing potassium cations between layers to coordinate into holes in the layer mesh.

Vacancies and cation substitutions common to the clay structure cause most clays to have negatively charged surfaces. To neutralize the charge the space between layers is often filled by partial octahedral sheets, potassium, sodium, and calcium cations, water molecules, ammonium ions, and organics (Moore and Reynolds, 1997). The edges of clay particles are also charged, and thus particles in water may align in a face-edge or edge-edge alignment. However, edges typically attract hydrogen or hydroxyl ions that negate this flocculation, or clumping of individual particles. The hydrogen content of water, or pH, effects flocculation/dispersion.

Clay floccules form more commonly by other means. The valence electrons in the outer anion layer of clays attract cations and water molecules that cling close to the surface. If the surrounding fluid has a higher concentration of cations, the attraction is greater and the fluid layer comes closer to the crystal. If clays become close enough they will flocculate due to van der Waals forces. Floccule formation in this way depends on the concentration of ions in the surrounding fluid, and the energy of the environment (Moore and Reynolds, 1997). Floccules are important for the ways they change clay behavior at the interface of fresh and salty water, changing energy environments, and how fast they are deposited.

2.2 Origin of Clay Minerals

Kaolinite is a 1:1 layer silicate, recognizable in diffractogram profiles by a repeat distance in the direction perpendicular to the (001) of 7.15 Å, and d(002) of 3.57 Å. Kaolinite is the most common clay mineral of warm, wet regions, and forms from acidic leaching processes (Moore and Reynolds, 1997). It is frequently found in lacustrine, deltaic, or lagoonal deposits (Moore and Reynolds, 1997). The Piedmont region of the Northeastern U.S. may have

contained significant kaolinite deposits originating from heavily weathered feldspathic soils (Moore and Reynolds, 1997).

Illite is a dioctahedral member of the 2:1 group, with a composition between muscovite and smectite. Basal spacings are d(001)= 10 Å, d(002)= 5 Å, and d(003)=3.33 Å. Illite is the most abundant clay mineral in sedimentary rocks. It is produced by pedogenesis, weathering, metamorphism, and diagenetic processes. It is rarely pure and commonly interstratified with smectite (Moore and Reynolds, 1997).

Glauconite is a poorly defined, Fe-rich mineral with many chemical similarities to illite, including the same approximate peak locations. It is found across a wide array of latitudes, but only forms in the modern world on outer shelves and continental slopes. Glauconite requires a reducing environment near the sediment-water boundary and the presence of organic matter to form. Detrital sediment accumulation is very low in these locations (Moore and Reynolds, 1997).

Smectite may be a dioctahedral or trioctahedral 2:1 clay. It has d(001)= 17.7 Å and d(002)= 8.5 Å when fully expanded by water or ethylene glycol. Air-dried peaks are broader, and shifted to d(001)= 15 Å , and d(003)= 5 Å. Smectite is known to form in large bentonite deposits from alteration of volcanic glass, and in environments with either slowly moving water or infrequent rain (i.e. swamps, arid regions). It may also form in soils from illite, kaolinite, and chlorite, but this transformation is not well understood (Moore and Reynolds, 1997). Because the smectite structure incorporates low-charge cations in place of aluminum in the crystal structure, the smectite layers often carry a charge that attracts water into the interlayer spaces. Smectite is considered to have a high shrink-swell capacity (Moore and Reynolds, 1997).

Vermiculite is compositionally similar to biotite, a 2:1 di- or trioctahedral mineral, and has d-spacings similar to smectite at d(001)=14.4 Å, d(003)= 4.8 Å. Vermiculite is less common than other clay minerals but may form from biotite, muscovite, or chlorite. It frequently is transformed to, and hard to differentiate from, smectite, with a moderate shrink-swell capacity compared to smectite. Vermiculite is frequently found in well-drained soils of humid regions, in areas with micaceous parent rocks. It should be noted that while abundant in some terrestrial and fluvial systems, it is not found in adjacent coastal areas (Moore and Reynolds, 1997). Either it is purely a transitional phase that does not persist in seawater, or it may only be a distinct mineral when crystal sizes are greater than average clays.

Chlorite has both di- and trioctahedral forms, and was classified as a 2:1:1 layer silicate in the past, now commonly grouped as 2:1. Peaks are at d(001)= 14.1 Å, d(002)= 7.07 Å, d(003)= 4.72 Å, and d(004)= 3.52 Å. Chlorite formation is not fully understood, because it is intermediate to many other clays. Chlorite is found in metamorphic greenschist facies, shales, soils, newly formed after carbonate in sandstones, and in geothermal environments. There are few methods to differentiate primary from detrital chlorite (Moore and Reynolds, 1997).

Interstratified mixtures of two different clay minerals are common, often in ordered rather than random stacks. In fact, illite/smectite is more common as a mixed-layered clay than individual illite or smectite alone. Smectite is known to transition to illite given burial, time, and heat, but these reactions are most important at depths of several kilometers (Moore and Reynolds, 1997). An illite to smectite transition is documented in acid environments produced by the oxidation of pyrite (Moore and Reynolds, 1997). The smectitization of illite may be common in marine environments, discussed in the following section. I/S peaks manifest as a mean average of constituent peaks. Glycolated, the d(001) is expected to be ~13 Å.

2.3 Geographic Distribution of Clay Minerals

Clays in the deep-sea tend to resemble those in nearby terrigenous soils. Generally, kaolinite and smectite are more abundant in the ocean at warmer low latitudes where chemical weathering and tropical soil formation influences the sediment load of rivers. Chlorite and illite are more abundant at cooler higher latitudes (Griffin et al., 1968). However, some anachronistic clay deposits point to the importance of diagenesis in shallowly buried sediments.

The long record of clay deposition in the Atlantic basin has implications for those found on continental margins. The major clay minerals deposited in the opening Atlantic basin have presumably been connected to changing sea level, the distance to the nearest margin, and sedimentation rate (Thiry and Jacquin, 1993). Neritic kaolinite deposits suggest strong terrigenous input, and are frequently incorporated in prograding delta facies. Kaolinite in the basal sediments of the early Atlantic are largely found in turbidite deposits along with traces of chlorite, illite, illite-smectite, and variable smectite.

Smectite is the most common phase of the later, deeper Atlantic, but does not appear to conform to patterns of changing sea level or margin distance. Proposed mechanisms for smectite enrichment in the deep-sea include differential settling, volcanic ash-fall alteration, authigenesis, or the transformation of detrital sediment. Nearshore concentrations may increase due to increasing soil erosion or differential settling, because smectite minerals are smaller than other clays (Patchineelam and Figueiredo, 2000). However, deep-sea smectites are frequently found in places with no nearshore counterpart, and during intervals of low terrigenous input. Additionally, smectite often peaks in nearshore sequences approaching a peak transgressive surface, and decreases just above it (Thiry and Jacquin, 1993). Thiry and

Jacquin (1993) concluded that the exposure of detrital clays to seawater, in environments with slow rates of deposition, causes the transformation into smectite.

2.4 Clay Peak Identification

Qualitative identification of clay minerals from a diffraction pattern begins by identifying the position of characteristic basal (00*l*) reflections (Fig. 5). Confirmation is then provided by peak position, intensity, shape, and breadth. All peaks belonging to each specific mineral are more or less evenly spaced on a diffraction profile. Initial identification is made based on the 001 peak, with higher angle peaks for corroboration. Line breadth, the mean width of a peak at half its height above background, should be the same for all peaks of a given mineral. Breadth is controlled by crystal thickness (Moore and Reynolds, 1997). Intensity, or height, of each line is related mainly to the abundance of that mineral relative to all other clays in that sample, but partially to the reflective power unique to each mineral.

Illite and glauconite have near overlapping peaks, but differ in intensity. Neither respond to glycolation or heating. Glauconite may be discerned based on a higher 001/003 ratio compared to illite (Moore and Reynolds, 1997). I002/I001 is another useful comparison to see changes in illite species.

Chlorite's strongest peaks at 002 and 004 partly overlap with kaolinite 001 and 002, respectively, but we can change the intensity of kaolinite peaks to aid identification. I use the fact that kaolinite becomes amorphous to x-rays after heating to determine which phase is present. To determine the maximum intensity of chlorite 002, and its contribution to the kaolinite 001 peak, the ratio of kaolinite 002 to chlorite 004 is used to scale kaolinite 001 before assigning quantitative values. Chlorite peak (004) had to be deconvoluted from overlapping

Kaolinite (002) in the process. The intensity of kaolinite is also reduced by a 0.8 multiplier because of it's enhanced diffraction over other minerals.

Vermiculite peaks do not shift significantly with glycolation, though they have moderate swelling potential. The 001 peak is typically strong so it may be detected in small quantities. Other 00*l* reflections overlap with vermiculite making it difficult to positively identify. Sepiolite, palygorskite, and halloysite are fibrous minerals with weak diffraction patterns in the low angle interval near mixed-layered clays and vermiculite.

Pure smectite is also a strong reflector and can be measured even when scarce. Glycolated samples alter the shape and location of diffractogram, producing a clearer peak. Air dried samples will be shifted significantly to larger angles. Illite/smectite responds to ethylene glycol solvation as significantly as pure smectite. Glycolated peaks show up in the region between 16 and 17.7° 2θ. Determination of illite/smectite is aided by the heated sample, where smectite has disappeared.

Specific minerals can be differentiated from within these categories, as well as proportions of coordinating cations and electron configuration, through countless combinations of solute saturations and heating. These finer points are not covered here for simplicities sake, and because the techniques were not utilized.

2.5 Quantitative Analysis

Intensity is related to relative abundance in the diffractogram (Fig. 5) of oriented clay slides on the assumption that all phyllosilicate minerals can be recognized in a sample. The ratio of one minerals' strongest 00*l* to the sum of all primary 00*l*, approximates the % composition. XRD is an established method for quantitative analysis, but is not as precise or accurate as other

tools of modern geology. Moore and Reynolds (1997) set a ±5% criterion as good precision for minerals present in large quantities (>20%). Replicate analysis shows this to be consistent with work shown here. Mineral quantities may only be as accurate as ±20% for minor components (<20%). Nevertheless, minor components may still show accurate trends regardless of their absolute abundance.

Every effort is made to ensure samples are homogenous through their thickness. Consistent sample preparation is necessary for meaningful quantitative analysis. Because the incident beam is absorbed logarithmically, minerals nearer the surface of the sample will be overrepresented. This usually pertains to the smallest size fraction of clays, the smectites. Samples are dried quickly by gentle heating to reduce particle size segregation.

Samples that are too thin will have weak intensities at high angles, where interlayered clays diffract. The ideal amount of clay on a prepared slide is said to have infinite thickness. In this context, infinite thickness means that adding to the sample thickness will not cause any further increase in diffraction intensity. In general, sample density about 15 mg/cm^2 can be considered infinitely thick. Similarly, X-ray beam slit sizes and glass slide sample length should be calibrated to each other to avoid the loss of intensity at high angles (Moore and Reynolds, 1997). Small slit sizes for clay specific analysis helps avoid this problem.

As well as relative percentage plots for each clay mineral, the Saddle ratio (Inoue et al., 1989) provides additional information about interlayered illite/smectite R0. The saddle on a diffractogram is the distance between base line and the bottom of the valley left of the illite/smectite peak. The height ratio of saddle/I001 changes based on the amount of smectite composing I/S, ranging from fully 100% smectite to a minimum ~45%. Because illite appears to transform to smectite given sufficient time and contact with seawater at the sediment water

interface, the saddle ratio may be used as an indicator of relative sedimentation rates (Inoue et al., 1989).

The weathering percent (W%) ratio is another application of clay abundances to view the proportion of clays based on source weathering material. W is derived from the formula W = K / (K + 2C), where K and C are the intensities of kaolinite and chlorite respectively. Higher chlorite content suggests the contribution of freshly weathered parent rocks of igneous or metamorphic origin. Kaolinite in the W ratio of marine sediments indicates the erosion of continental regolith, which may be prompted by tectonic uplift or changing sea level. The ratio is helpful in seeing this relationship because it is useful even if the proportion of one clay is small.

3. Methods

3.1 Carbon Isotopes

Bulk $\delta^{13}C$ and $\delta^{18}O$ isotopes were analyzed at the Rutgers stable isotope lab by J.D. Wright. This thesis utilizes isotopic samples from the Vincentown, Marlboro, and Manasquan Formations. Values reported in Wright and Schaller (2013) are measured at 0.2 ft (0.061 m) intervals from 360.0-370.0 ft (109.73-112.78 m) and every ~1 ft (30 cm) from 304.5-359.5 ft (92.81-109.58 m) and 370.5-381.5 ft (112.93-116.28 m).

3.2 Clay Mineral Analysis by X-ray Diffraction

All quantitatively analyzed clays were selected and sampled at Rutgers University, and then transported to the University of Mons, Belgium. Processing and scanning by XRD was done with instruction and guidance from C. Dupuis. Later analyses targeting narrow intervals of core material were performed at Rutgers University using methods modified from those used at Mons.

The Marlboro Formation (Figs. 3, 4) spans the interval 317.50-366.30 ft (96.77-111.65 m), with the Vincentown Formation continuing down to ~390 ft (118.87 m). Samples were taken at 2 ft (61 cm) intervals from 318.80-378.50 ft (97.17-115.37m), with additional samples taken every ~0.5 ft (~15 cm) from 360.04-369.5 ft (109.74-112.67 m). Two samples from the overlying Manasquan Formation were taken at 314.90 ft (95.98 m) and 305.15 ft (93.01 m). Pie-shaped slices about 10 cm^3, the minimum volume for this type of clay analysis, were cut using a razor blade from the working core half. A quarter cylinder of core from 342.47-342.69 ft (104.38-104.45 m; 6.6 cm) containing 4 laminae and 4 beds was also extracted to be sampled later. All sample surfaces were removed at a depth of ~1 mm to reduce risk of drilling mud contamination and exclude post-drilling gypsum precipitate. Along with Wilson Lake core

material, four outcrop samples were produced by dividing a 2 cm thick outcrop sample along horizontal planes.

Samples for X-ray diffraction were prepared via the oriented glass slide method, similar to descriptions in Moore and Reynolds (1997). Samples were dried overnight in 60°C oven and then deflocculated with deionized distilled water (DI). The mixture was then titrated with a 10% HCl solution until the reaction stopped. The silt and clay fraction was stirred into suspension, decanted into centrifuge tubes, and spun at 6,000 rpm for 15 minutes. Supernatant fluid that included dissolved salts was decanted and replaced by more DI water. The sample was returned to a beaker and placed in a stirring machine for 10 minutes to disperse remaining clay aggregates. Centrifuge and mixing steps were repeated as before. After the second mixing, beakers were evaluated for a stable suspension of clay with no visible flocculation. Beakers were set aside to allow particle settling for 1 hour 35 minutes. Meanwhile, glass slides were preheated on a 40°C heating tray. When only clay remained in the upper 4 cm of solution, determined by Stoke's Law, a syringe was inserted 2 cm into the liquid for extraction. The suspension was deposited on each slide and left to air dry within ~ 1 hour. Consistency was achieved by spreading the sample evenly over each slide and creating a meniscus of standard height.

Three slides were produced for each sample to be analyzed 1) air dried, 2) saturated overnight with ethylene glycol, and 3) heated to 490° C for 2 hours (Fig. 5). A Siemens Diffraktometer D5000 Kristalloflex scanned natural and heated slides from 4.000° to 14.000° 2θ, at a step interval of 0.020° for 2.5 seconds each. Glycolated samples were run at a step interval of 0.020° for 2.5 seconds each from 4.000° to 29.000° 2θ. Samples were spun during scanning to average out differences in thickness and slide coverage.

Peak heights were measured relative to background, and correction multipliers were applied as needed for kaolinite (0.8) and illite/smectite (1-2) depending on the peak breadth. Peak positions were checked against literature and the comprehensive list in Brindley and Brown (1980).

3.3 Additional XRD at Rutgers

Sample preparation techniques needed to be modified to run samples on the Rutgers University Chemistry Department Phillips XPert. The new technique was devised for maximum consistency between all slides. Unlike Mons samples where horizontal clay orientation was assured by suspension settling, Rutgers samples are bound to be less well-oriented because they were done on smear slides. Reliable quantification depends on all minerals being equally well oriented. Replicate analysis confirmed precision comparable to the original oriented glass slide method. Accuracy of % relative abundance could only be corroborated to previous results from this interval, but they are within the expected error range. Samples were still dried quickly to prevent size sorting and the preferential representation of smectite. Rutgers samples were analyzed without glycolation, so the abundance of smectite is expected to be lower.

Initial clay analyses provided 2 ft (61 cm) stratigraphic resolution for the Marlboro Clay, but time did not permit evaluation at a smaller scale. The interval 346-348 ft (105.46-106.07 m) was selected for further investigation, and sampled continuously as 2 mm thick chips of core material. Samples were powdered and material was split for stable isotopes and clay mineral analysis. For clays, one slide per sample was prepared between 280-360 mm from the top of the core section. The volume of sediment required was less than a full spatula scoop, but was not weighed precisely. Sediment was transferred to a 2.5 cm diameter glass slide and worked into a slurry with a scant drop of defflocculant and water mixture. Two slides were rubbed

together to ensure even coverage and then slid quickly apart for a consistent thickness among all samples. Slides were placed on a heating plate to dry for < 30 seconds. All samples were kept in an oven at 60° C until just before XRD analysis.

3.4 Grain Size Analysis

Grain size distributions (Fig. 6) were generated using a Beckman Coulter LS 13 320 Laser Diffraction Particle Size Analyzer. Thirty samples were processed and taken to the University of Pennsylvania Department of Earth and Environmental Science laboratory of B. Horton. The Wilson Lake core was sampled at approximately 2 ft (61 cm) intervals between 321 and 378 ft (97.8-115.2 m). Between 1.50-3.00 g were dried and disaggregated in 35 ml distilled deionized water with ~0.2 g sodium-metaphosphate. Sample vials were vigorously shaken before ≤ 1 mL was transferred to the machine. Computer software monitored the required amount of sample by laser obscuration. Each sample was sonicated and analyzed in duplicate. Output was given as the volume of sample that passes through micron-scale channel size ranges, normalized to 100%.

Results were interpreted not just by mean grain size changes, but for changes within the silt size fraction. Some grain size fractions are more prone to sorting by energy changes in the environment. McCave et al. (1995) proposed a particle behavior boundary at 10 µm due to the prevalence of sediment cohesion below 10 µm, and individual particle interactions above. Silts and clays below 10 µm are more prone to aggregation by Van der Waals forces. The range 10-63 µm is the sortable silt fraction that is expected to change proportionally to current speed. The ratio of the cohesive to incohesive sediment fraction should aid in grain size analysis by responding positively to current increases (McCave et al., 1995).

3.5 X-ray Fluorescence

Core-scanning XRF is a non-destructive method used to estimate relative elemental abundances in split soft sediment cores. I use XRF to identify and interpret features in the Wilson lake core (Fig. 7). Only a limited amount of material was analyzed to evaluate the applicability of this technique for lithostratigraphy. Though the data were collected in high detail, their implications for the Marlboro Formation are limited.

The result of XRF scanning is a near continuous record responding to the atoms at the surface of the core. Incident X-rays cause excited electrons to move from inner atomic shells to outer shells. The inner shell vacancy is thereby filled by an electron from an outer shell that emits surplus energy as a secondary X-ray. The energy and wavelength of the secondary X-ray is indicative of the atomic number of the atom it left (Lyle et al., 2012).

XRF will also respond to changes in the porosity and water content of unconsolidated sediment, thus consistent sample preservation is essential (Lyle et al., 2012). Sample distance from the emitter has a known effect on the intensity of XRF, so scanning distances are usually quite small. In addition, a prolene film may be put on the split core to improve signal transmission. XRF is applied here semi-quantitatively, with data presented as counts per unit time per unit area. Volume to weight elemental conversions are possible but not without known device calibration (Weltje and Tjallingii, 2008).

Due to practical limitations of shipping 15 m of sediment core across country, a representative 2 ft (61 cm) section was sent to the Large Lakes Observatory at University of Minnesota Duluth. XRF Lab Manager A. Lingwall scanned the core for 45 major element concentrations at 0.5 mm intervals. Element counts were plotted with respect to core photographs looking for any visible correlation to visible features. A correlation matrix was also

used to understand the relationship between elements and the preservation of the core (Table 1). Select element-element ratios were plotted to assess changes with depth. Changes to single element and element-element ratios with depth may be the result of changing sediment provenance, biologic activity, redox conditions, etc., as previously described in deep-sea cores (Croudace et al, 2006; Rothwell et al., 2006, Thomson et al., 2006).

Spectral density analysis was performed on several element profiles to investigate elemental cyclicity in the range of couplet thickness. Elements were run in Analyseries through Periodogram and BTukey algorithms, and for the removal of linear trends. Filtering was justified by the presence of a peak near the period 0.5 (2.0 cm), and a Gaussian filter at a frequency of 0.5 and bandwidth 0.25 (covering the range 1.3-4.0 cm) was applied. In addition to single elements, Analyseries was applied to the machine calibration data of distance to sample surface, as well as coherent and incoherent scattering.

3.6 Visual Descriptions

The few notable visual features of the Marlboro Formation at Wilson Lake are below the resolution of our fresh core photographs. I measured the position of core features at the millimeter scale from the Marlboro Formation upper unconformity through the top of the underlying Vincentown Formation, and annotated depth and descriptions of features on core photographs. Depths are from the working half of the split core with the archive half present to ensure completeness in lieu of sample removal. Recorded features consist mainly of the elevated ridges associated with swelling clay laminae as visible on the core split face, but also include notes on horizontal core breaks, color, surface gypsum precipitation, nodules, and oxidation. Depths of laminations are compiled in a spreadsheet that includes a rating of each one's prominence at the time of description. Mean couplet thickness and standard deviations

are calculated on a per foot basis where present in the Marlboro Formation. Comparison of laminae distribution to other core analysis gives some indication of their origin.

4. Results

4.1 Clay Mineral Stratigraphy

The mineral assemblage recognized at Wilson Lake is composed of kaolinite, interlayered illite-smectite, illite (with the possible inclusion of mica at overlapping ° 2θ), chlorite, and vermiculite (Fig. 5). Kaolinite, illite, and illite/smectite are the most prevalent, and trends in their relative percent are described below (Fig. 8). Relative percent chlorite and vermiculite do not vary greatly, and are not discussed in detail.

Results from Vincentown Formation samples at 367.44-378.50 ft (112.00-115.37 m) consist of components from greatest to least, as follows: illite 33-40%, illite/smectite 28-39%, kaolinite 15-22%, chlorite 4-9%, and vermiculite 3-7%. Upward from the base of the Marlboro Formation at ~366.3 ft (111.65 m), there is a dramatic initial shift in relative clay abundance towards higher kaolinite, and lower illite/smectite between sample depths 364.92 and 366.00 ft (111.23-111.56 m). From 360.43-364.45 ft (109.86-111.08 m) kaolinite sharply decreases to an intermediate value, before increasing again. Overall, the samples 338.30-366 ft (103.11-111.56 m; Unit 1 on Fig. 8) are composed of: kaolinite 30-50%, illite 22-42%, illite/smectite 7-36%, chlorite 3-9%, vermiculite 2-7%. The sample at 337.74 ft (102.94 m) is sharply lower in kaolinite (27%), and has relative increases in illite/smectite and chlorite. At or above 334.23 ft (101.87 m) there is a clear trend of kaolinite decrease, and illite/smectite increase upward. The highest sample within the Marlboro Formation, 318.80 ft (97.17 m), consists of 40% illite/smectite, 25% kaolinite, 25% and illite. Kaolinite is mostly absent above the contact. The Manasquan Formation consists of 60-76% illite/smectite, 23-31% illite, 0-1% kaolinite, 0-2% chlorite, and 0-4% vermiculite.

4.2 Saddle Ratio

The height of the illite/smectite peak does not rise above the saddle for much of the Marlboro Formation (Fig. 8). Regardless, Wilson Lake has stratigraphic changes in the percent smectite in illite/smectite (I/S) near the upper and lower contacts of the Marlboro Formation. From the lowest sample at 378.50 to 363.04 ft (115.37 to 110.65 m) saddle values range from 0.67 to 0.85, or about 57 to 52% smectite in I/S. The value rises to a maximum ratio about 1 m above the $\delta^{13}C$ excursion level, equivalent to the minimum 45% smectite required to be classified as illite/smectite.

The saddle ratio decreases again near the top of the Marlboro Formation (saddle= 0.95). The sample at 324.62 ft (98.94 m), only ~10 cm above the highest occurrence of the swelling clay laminae, contains ~50% smectite in I/S. The percent smectite in I/S increases steadily to 60% in the 4 samples before the upper contact (317.50 ft; 96.77 m). Manasquan Formation samples 305.15 and 314.90 ft (93.12 and 96.16 m) contain percent smectite in I/S as 78 and 67, respectively (Fig. 8).

4.3 W% Ratio

The weathering ratio is highly variable throughout the study interval due to the very low chlorite content. In the Vincentown Formation it fluctuates between ~58 and 75% (Fig. 8). In the Marlboro Formation it is between ~70 and 90%. Consequently, Marlboro Formation clays may be described as more weathered. As with kaolinite, W% falls to low or zero values in the Manasquan Formation (Fig. 8).

4.4 Clay Mineral Microstratigraphy

Only kaolinite, illite, and illite/smectite were positively identified in the closely sampled interval of the 346-348 ft (105.46-106.07 m) core segment. Kaolinite ranges from 52-64%, illite from 32-47%, and illite/smectite from 1-4%. The two major components, kaolinite and illite, fluctuate inversely with each other, and the minor illite/smectite behaves independently (Fig. 9). The sampled interval traverses 4 laminae, the 2 lower ones being noticeably thicker. At approximately the same level as the 2 lower laminae, illite/smectite content peaks to ~4%. These 2 data points coincide with increases in kaolinite and decreases in illite. The difference in clay composition between laminae and couplet beds though relatively minor, is measurable.

4.5 Grain size stratigraphy

The most prominent grain size feature is the change from the silty sand of the Vincentown Formation to the clayey silt of the Marlboro Formation (Fig. 10). There is a trend towards greater sand abundance in the upper meter of the Vincentown Formation, composed mostly of glauconite. Mean grain size in the Vincentown Formation (Fig. 10) is ~86 µm, increasing from ~62 µm at 378.50 ft (115.37 m) to ~150 µm at 367.00 ft (111.86 m). Mode Vincentown Formation grain size is ~116 µm for samples from 370.95-378.50 ft (113.07-115.37 m), increasing to ~168 µm at 367.00 ft (111.86 m). The Marlboro Formation itself displays very little change in grain size. Just above the Marlboro Formation contact, the mean grain size decreases to ~36 µm. Mode value for all Marlboro Formation samples (Fig. 10) range from ~5.9 µm to ~7.1 µm.

Mean values for many of the most clay-rich samples appear spurious, resulting from user error with the Coulter Counter. Grain size distributions for these samples show a bimodal plot with a peak in the mud size range and another >200 µm. These same samples have the

highest obscuration values, and their mean averages are not considered an accurate reflection of grain size. Presented data (Fig. 10) have been filtered to remove results above 200 μm and normalized to 100%. Mode values are preferred because values are similar between high and low obscuration samples.

4.6 Sortable Silt

The sortable silt ratio ([10-63 μ] / [<63 μ], brackets [ ] denoting cumulative volume % within specified range) is distinctly different for the Vincentown Formation and Marlboro Formation (Fig. 10). High Vincentown Formation values (0.45-0.57) occur below low (0.19-0.29) Marlboro Formation values with the change occurring at 362.95-364.90 ft (110.63-111.22 m). The sample at 364.90 ft (111.22 m) has an intermediate value (0.43) between Vincentown and Marlboro Formations. Decreasing values upsection in the Vincentown Formation lead the change to clayey silt lithology of the Marlboro Formation. Marlboro Formation samples do not show an obvious trend, but those in the upper 10 ft (321.15-331.95 ft, 97.89-101.18 m) are marginally coarser grained. A 3rd order polynomial trend line (Fig. 10) shows the slight increase upsection.

4.7 X-ray Fluorescence

X-ray Fluorescence (XRF) results were plotted in alignment with core photographs, but do not successfully show a match between laminae, couplets, and single elemental plots (Fig. 7). Several broad trends are discernible using XRF depth plots and a correlation matrix of abundant elements. Data are presented (Table 1) using Pearson's r correlation coefficient ranging from -1 (inverse relationship) to 1 (normal relationship), with 0 indicating no correlation. The data set for sample surface, a measure of distance from XRF scanner to core surface, appears to strongly influence some results. Silicon, aluminum, and potassium plots show a linear decreasing trend

with depth and a major spike at ~50 cm. Pearson's r values between silicon, aluminum, and potassium are high, generally ≥ 0.9 (Table 1). Sulfur and calcium plots have a 0.93 r to each other and a linearly increasing trend with depth, but also strongly negative values with silicon, aluminum, and potassium. All of these elements have strong r coefficients (≥ ±0.7) to sample surface.

Iron and iron-based ratios generally lack the sample surface correlation, showing no linear trend (Fig. 7). Iron has a moderate relationship with Compton and Rayleigh scattering (r for Mo inc=0.66, Mo Coh=0.65), but even stronger values for silicon, potassium, chromium, rubidium, and lead (Table 1). The iron curve shows distinct peaks at two nodule beds, possibly siderite concretions, and other minor features (Fig. 7).

The primary interest of gathering XRF data was to determine if it could identify the rhythmic beds in the core. However, the total XRF scanning length is longer than the length of the core when all segments are closely fit together indicating the inclusion of core gaps in the scan. Inclusion of gaps complicates alignment of scan to core photographs. Some prominent core gaps, as well as two nodule beds in this section, are used as tie-points to correct some of the offset between data and photo. Spectrum density analysis using the Analyseries program avoids some incongruities of data to photo matching. Filtered data of iron (Fig. 11) and manganese have strong powers near the average bed thickness of 2 cm. Iron has 3 peaks of decreasing intensity from ~2.35, 1.88, and 1.56 cm (Fig. 11). Manganese peak intensity is increasing from 2.42, 1.98, and 1.78 cm. However, these periods were identified in narrowly filtered data (see methods). Unfiltered data tend to be dominated by peaks corresponding to 6.8, 13.5, 16.6, and 58.8 cm. Additionally, power recognition around 2 cm is seen in filtered data for sample surface (Fig. 12), incoherent, and coherent scattering. The 2 cm cyclicity cannot

be reliably ascribed to a variation in elemental concentration due to the effects of sample surface. The distance between the X-ray emitter and the surface of the core overprints a signal that was caused by the misalignment of core segments that have shifted at laminae locations.

4.8 Laminae Enumeration

There are approximately 545 laminations in the Marlboro Formation at Wilson Lake. I labeled each laminae with a depth and confidence ranking, with low-confidence reserved for the very faint. Low confidence laminae, which can be confused with ridges left by the core-splitting process, were excluded. There are possibly 25 more laminae than counted. Because the Wilson Lake cores were divided in 2 ft (61 cm) increments immediately after drilling, the Marlboro Formation interval was bisected at ~25 locations. No laminae were positively identified at the top or bottom of each core section, and at most 25 laminae may have been obscured. I estimate the total laminae count does not exceed 570.

Laminae are not evenly spaced throughout the core (Figs. 13-18). Otherwise, 15 m of core with laminations every 2 cm (Fig. 19) would contain ~750 couplets (> 570 max). Indeed, there are regions of greater/lesser occurrence that coincide with decreases/increases in couplet thickness (Figs. 15-19). From 365-366 ft (111.25-111.56 m), laminae appear at the lowest level of the Marlboro Formation (Fig. 18) and couplets are of consistent thickness (Fig. 20 column d). Between 364-365 ft (110.95-111.25 m; Fig. 18), near where illite-smectite peaks to its highest level after the CIE, laminae are almost entirely absent. They return with greater visibility and consistent couplet thickness during 340-364 ft (103.63-110.95 m, Figs. 16-18). Couplet population has greater mean thickness and higher standard deviations (fewer laminae; Fig. 19) in intervals from 330-336.5 ft (100.58-102.57 m), and 338-340 ft (103.02-103.63 m; Fig. 15). Some thin intervals around 333 ft (101.50 m) and 331 ft (100.89 m; Fig. 15) are distinctly more

laminated than adjacent core. Despite some short gaps, couplets are once again consistent, but appear fainter, for the uppermost laminated interval (325-330 ft; 99.06-100.58 m; Fig. 14).

The average distance between successive laminae is used to calculate average couplet thickness. Mean average is 2.34 cm, and is greater than the 2.0 cm mode value. A frequency distribution histogram (Fig. 19) shows the positive skew and higher mean average is caused by the unlaminated intervals.

5. Discussion

The Paleocene-Eocene boundary is determined by initiation of the CIE (Aubry et al., 2007) which occurs at ~370 ft (112.78 m). The lithostratigraphic and clay mineralogic record is correlated to the carbon isotope record provided by J.D. Wright. Pre-CIE values of the Vincentown Formation range from approximately -1 to 1‰. The initiation of the excursion is shown to be a decreasing upward $\delta^{13}C$ trend (Fig. 21) which begins at 369.5 ft (112.62 m) and continues to 365.8 (111.50 m) ft. Values continue to decrease to -5‰ by ~356.5 ft (108.7 m), and maintain strongly negative values for the rest of the Marlboro Formation. The CIE is truncated by the upper unconformity at 317.75 ft (96.85 m; Fig. 3) separating the Marlboro and Manasquan Formations.

5.1 Lithologic Succession at Wilson Lake

Within the Marlboro Formation at Wilson Lake, I have identified three lithologic units (Fig. 20 column e). These distinctions are based on core descriptions, the presence of bedding, and clay mineral XRD results. Unit 1 consists of 9.24 m of consistently laminated, high-kaolinite, high-saddle ratio clays from 336.00-366.30 ft (102.41-111.65 m). Unit 2 consists of 3.40 m of irregularly laminated, decreasingly kaolinitic clays from 324.80-336.00 ft (99.01-102.41 m). Unit 3 consists of 2.24 m of non-laminated, high-illite/smectite, low-saddle ratio clays from 317.50-324.80 ft (96.77-99.01 m). Other data sets are considered in this context below.

5.2 Vincentown Formation and Unit 1 Marlboro Formation

Kaolinitic clays occur above and below the CIE and are increasingly important upsection in the Vincentown Formation. The occurrence of kaolinite below the CIE is also described at other locations in New Jersey. Gibson et al. (1993) and Gibson et al. (2000) reported a slight

increase in kaolinite (≤ 9%) upward through the Vincentown Formation, based on 4 samples spanning 24.9 ft (7.6 m) from Clayton, NJ, and 3 samples spanning 15.1 ft (4.6 m) from the GL-917 drillhole (slightly upbasin from Clayton; Figs. 1, 22). Wilson Lake B has a similar trend (Fig. 20) of increasing percent kaolinite from the lowest sample 378.5 ft (115.37 m; 16% kaolinite) to 367.44 ft (112.00 m; 20% kaolinite). The presence of kaolinite in the Vincentown Formation suggests a kaolinite-rich source region was undergoing physical erosion beginning before the CIE. Evidence from the $\delta^{18}O$ of clays at Bass River indicates they represent the weathering and transport of Cretaceous laterite soils (John et al., 2012). The kaolinite present in the Marlboro Formation was not formed by chemical weathering in the PETM climate.

The lithologic contact between the Vincentown and Marlboro Formations (366.30 ft; 111.65 m) occurs in a narrow interval based on dominant lithology and the change from olive-gray to white-gray colored clay. However, clay minerals and grain size indicate the lithologic change is more protracted (Fig. 21). The rapid percent kaolinite increase from 19% to 44% at Wilson Lake occurs between samples at 367.44 ft (112.00 m) and 366.00 ft (111.56 m), at least 0.2 ft below the large (-2‰) shift in the $\delta^{13}C$, but above the onset at ~370 ft (112.78 m). The deposition of highly kaolinitic clay begins at the lithologic contact. The occurrence of kaolinite at Wilson Lake is consistent with increased physical weathering and an increased hydrologic cycle (Kopp et al., 2009) that begins in the Vincentown Formation below the onset of the CIE, and before the larger negative shift in $\delta^{13}C$.

The saddle ratio for the lowest ~1 m of Unit 1 of the Marlboro Formation (363.04-366.30 ft; 110.65-111.65 m) is unchanged from the Vincentown Formation values of 0.67 to 0.85 (52-57% smectite in interlayered illite/smectite; Figs. 8, 20). The high content of smectite layers (low saddle ratio) for the Vincentown and lower Marlboro Formations indicates

intermediate burial rates (vs. slow in the overlying Manasquan Formation). Above 363.04 ft, and for most of the Marlboro Formation, the saddle ratio increases to 1.0 (~45% smecite in interlayered illite/smectite). This suggests a change from intermediate to rapid burial rates ~1m into the Marlboro Formation.

Grain size also changes gradually across the lower contact. The Marlboro Formation below ~364 ft (110.95 m) is siltier than above and, progressing upward, contains decreasing glauconite. Mode grain size at 364.9 ft (111.22 m; 9.4 μm) is higher than in the rest of the Marlboro Formation (Fig. 10), and includes very fine sand and glauconite. Unit 1 of the Marlboro Formation appears otherwise consistent in terms of clay mineralogy and couplet thickness (Fig. 20). Carbon isotopes maintain low values ~-5‰ throughout Unit 1 (Fig. 20).

A sharp decrease in the % kaolinite near the top of Unit 1 can be correlated to a similar decrease (Fig. 20, 22) in the Clayton, NJ core (Gibson et al., 2000). The clay XRD sample at 337.74 ft (102.94 m) measures only 27% kaolinite compared to adjacent samples (~40% kaolinite; 338.3 ft [103.11 m] and 334.23 ft [101.87 m]). The low % kaolinite interval is not correlated to Bass River. Bass River has a condensed interval of comparatively slower accumulation that corresponds approximately with the “core” of the CIE (Stassen et al., 2012b). All of the Wilson Lake sediments that are preserved below the erosional unconformity are correlated to the “core.” The brief kaolinite decrease may not be recorded at Bass River, or samples may not have identified it.

The low kaolinite sample at 337.74 ft (102.94 m) within Unit 1 (Fig. 20) may be associated with temporarily decreased detrital clay and freshwater input. Stassen et al. (2012) report an ecological change from Wilson Lake A that is near, and may overlap the abrupt kaolinite decrease at Wilson Lake B (Fig. 22). A sharp decrease in the abundance of low-salinity

tolerant taxa in their samples at Wilson Lake hole A (WL-A) at 335.27 ft (102.19 m) and 336.85 ft (102.67 m) suggests not as much freshwater was being carried on to the shelf. A maximum offset of 5.4 ft (1.8 m) between the two drillholes (Fig. 22) is obtained from the sharp -2‰ isotopic change that occurs between 360.89-362.53 ft (110.0-110.5 m) at WL-A, and 365.5-366.8 ft (111.40-111.80 m) at WL-B, as well as gamma log correlation (Fig. 4). A decrease in river discharge composed of freshwater and kaolinitic sediments may account for the mineralogic and ecologic change.

5.3 Unit 2

Unit 2 is recognized by increased couplet thickness and short non-laminated intervals (~10-30 cm) that represents a transitional unit between Units 1 and 3 (Fig. 20). Couplet variability increases above ~336 ft (102.41 m) and Unit 2 is decreasingly kaolinitic upcore. The kaolinite change is interpreted as a decrease in freshwater and detrital clay to the Wilson Lake site. The assemblage of clays could change because of oceanographic shifts bringing more saline water across the shelf, but because illite/smectite alteration also increases in Unit 3, above, lower sedimentation rates and freshwater bypass are the preferred explanation. At the same level, carbon isotopes start increasing and reach -4‰ by the top of Unit 2. Sedimentation rates are interpreted as high during Unit 2 because the saddle ratio is unchanged from Unit 1.

5.4 Unit 3

Swelling clay laminations are entirely absent above 324.8 ft (99.01 m, Fig. 3), marking the base of Unit 3 (Fig. 20). Though units 2 and 3 becomes decreasingly kaolinitic at shallower depths, a return to lower saddle ratios (higher %S in I/S clays) only begins above the highest couplet occurrence (Unit 3; Fig. 20). The clay mineral assemblage in Unit 3 looks similar to that at the bottom Unit 1 and at the top of the Vincentown Formation. The resurgence of high %

smectite in illite/smectite above the last lamination indicates increasing clay alteration, possibly due to lower sedimentation rates or a change in the sediment pathway to this region of the paleoshelf. Associating the unlaminated clay with a mineralogic change demonstrates that couplets are a primary feature of deposition. Their occurrence at Wilson Lake, Millville (Wright and Schaller, 2013), in outcrop at Medford (Wright and Schaller, 2013), and in the South Dover Bridge, MD core (Self-Trail et al., 2012) indicate that they are not a feature caused by drilling.

5.5 Sediment Distribution on the Amazon Shelf

Kopp et al. (2009) compared the Marlboro Formation to a tropical river-dominated shelf based on the geographic extent of fine-grained sediment and the preservation of biogenic magnetofossils. Shelf morphology adjacent to mud-laden rivers is correlated with physical and oceanographic features such as mean wave height, tidal range, shelf width, and annual sediment load (Fig. 23; Walsh and Nittrouer, 2009). Environmental indicators reported for the Marlboro Formation indicate conditions were similar to the shelf adjacent to the Amazon River, suggesting they may have similarities in morphology, depositional processes, and sedimentation rates.

Mud-dominated shelves like the Amazon typically capture sediment just below wave-base, and are sculpted for hundreds of kilometers by along-shore ocean currents. The middle shelf depositional setting at Wilson Lake (Zachos et al., 2006), the lack of sandy deposits, and the minimum water depths inferred from benthic foraminifera in the Marlboro Formation (Stassen et al., 2012b) are similar to both Marine Dispersal Dominated (MDD) and Subaqueous Delta Clinoform (SDC) systems (Fig. 24) as defined by Walsh and Nittrouer (2009). Both shelf types are affected by high sediment supply, wide shelves, and distal shelf accumulation, but differ in the role of wave versus tidal forces (Fig. 23). MDD shelves tend to be affected by wave

height more than other factors, resulting in the possibility of multiple depositional foci over a wide range of water depths. The Columbia and Eel Rivers were used to develop the MDD model, where sediment accumulation is frequently in deeper water, and several several active depocenters are present that change through time. SDC shelves have comparatively greater sediment supply or tidal range (Walsh and Nittrouer, 2009). Large tidal range enables the region of highest deposition to be disconnected from the river source, unlike a standard delta. The Amazon shelf is the archetype for SDC systems, and displays high deposition on the foresets of active clinoforms (Fig. 24). Other shelf morphologies are typically too shallow or narrow compared to the Salisbury Embayment. I apply the SDC model to the Marlboro Formation because of the evidence for a wide New Jersey paleoshelf and the clinoform shape of preserved Marlboro Formation thickness (Fig. 25). In modern settings, there are continental shelves that are gradational between SDC and MDD forms, and the Marlboro Formation does not need to fit exclusively into either category.

Descriptions I have made of the Marlboro Formation at Wilson Lake are similar to those of mud facies reported on the northwest Amazon shelf. The suspended load of sediments on the Amazon Shelf is 85-95% silt and clay (Gibbs, 1976), compared to 80-99% in Marlboro Formation sediments at Wilson Lake. Sands on the Amazon Shelf are confined to the several hundred kilometers around the river mouth, where they are preserved in tidally influenced interbedded mud and sand layers about 10 cm thick (Fig. 26; Kuehl et al., 1996). Interbedded strata give way to faintly laminated muds northwest of the river mouth. Laminations described in shallow cores there are thin (~1 mm) coarse-silts found at 1-20 cm intervals in an otherwise homogenous mud. Sediments arrive at this area, beyond the Cabo Norte Shoal, primarily by advective transport of brackish-water surface plumes (Fig. 27; Sommerfield et al., 1995). Grain size is limited to ≤16 μm (Kuehl et al., 1986b). The Marlboro Formation at Wilson Lake, devoid

of significant coarse particles and far from the hypothesized paleo-Potomac, paleo-Susquehana, and paleo-Hudson river sources (Kopp et al., 2009), is similarly laminated and fine grained.

Kaolinite and smectite are separated from each other with increasing distance across and along the Amazon shelf. Both clays maintain proportions ~30% close to the river source, but as distance increases parallel to the coastline and further offshore, kaolinite decreases to ~20-25%, and smectite increases to >40% (Patchineelam and Figueiredo, 2000). Kaolinite tends to flocculate immediately at the salinity front just beyond the river mouth, where it is prohibited from northwestward movement by the Cabo Norte Shoal (Fig. 27). It does travel a shorter distance to the southeast, becoming a major component in the interbedded mud and sand, as well as the mottled mud, facies (Patchineelam and Figueiredo, 2000; Kuehl et al., 1986b). On the other hand, smectite requires more saline water to flocculate and may be transported across the shoal in suspension (Patchineelam and Figueiredo, 2000). Once there, it tends to flocculate and travel offshore in large quantities.

Based on the relationship of mineral content and distance to the river mouth on the Amazon shelf, I consider two explanations for the percent kaolinite changes at Wilson Lake. The upward decrease in percent kaolinite in the Marlboro Formation could reflect an increasing distance and paleodepth in Units 2 and 3. A relative sea-level rise is inferred during the PETM based on benthic foraminiferal biofacies in the NJCP (Harris et al., 2010; Stassen et al., 2012a,b). However, if Units 2 and 3 were deposited at greater paleodepths, I would expect a decrease in average grain size from Unit 1. Instead, mode grain size stays the same upward through the Marlboro Formation, and the sortable silt ratio indicates a slight coarsening.

Alternatively, the change in percent kaolinite in Marlboro Formation clay is related to the preferential flocculation of kaolinite and the subsequent transport patterns of floccules.

Higher nearshore flocculation and settling of kaolinite, as predicted by the Amazon model (Patchineelam and Figueiredo, 2000), is consistent with higher percent kaolinite reported updip in the Salisbury Embayment (Gibson et al., 2000). However, Wilson Lake was located on the middle shelf far from river sources. Thus, a change in the clay input, from either the river or across-shelf transport, is the favored hypothesis. Based on the Amazon model of clay distribution and the determination that kaolinite is a physical weathering product (John et al., 2012), I suggest that the percent kaolinite decrease upsection at Wilson Lake resulted from a decrease in freshwater to this area of the paleoshelf. This may indicate that the hydrologic cycle, intensified during the PETM (Kopp et al., 2009), was slowing down. Alternatively, the transport of freshwater and kaolinitic clays may have largely bypassed the paleo-shelf near Wilson Lake.

The clay mineralogy of the laminated mud facies (Fig. 26) on the Amazon shelf does not match the sediments at Wilson Lake. The northwest Amazon shelf is the area of highest salinity and smectite deposition. The lack of kaolinite is attributed to the presence of the Cabo Norte Shoal (Fig. 26), which affects the transport of sediment by the North Brazil Current and traps kaolinite near the river mouth (Patchineelam and Figueiredo, 2000). The Salisbury Embayment topography may have allowed the transport of kaolinite further into the basin. The Amazon study focuses only on clay minerals in the upper meters of sediment, thus no Amazon record exists to explore mineralogic changes in longer cores, like those from the New Jersey Coastal Plain.

5.6 Comparison to Amazon Shelf Processes

Kaolinite is not dominant in the laminated mud facies of the Amazon shelf, but it is abundant where another important process, fluid mud formation, is occurring. The presence of

fluid mud cannot be unequivocally demonstrated for the Marlboro Formation paleoshelf, but it may explain features including the lack of bioturbation, rhythmic 2 cm beds, convoluted bedding at Ancora (Fig. 28; Harris, 2010), and the rapid burial of an upright lignite fragment at Wilson Lake (366.5 ft, 111.71 m). Fluid mud is a nearbed layer of suspended sediment, typically >10 g/L and 1-2 m thick, lacking mechanical strength and capable of transporting sediment great distances across and along the shelf (Kineke et al., 1996). Generally, fluid mud forms in seasonal cycles in topset regions around the 10 m isobath of the Amazon shelf (Fig. 27; Kineke et al., 1996). More than 90% of suspended sediment on the Amazon shelf is within fluid mud, where it is incorporated near the river mouth at the bottom salinity front from riverine sediment (Kineke and Sternberg, 1995). These shallow nearshore areas do not permanently trap sediment because they are prone to strong mixing and the frequent resuspension of the top ~1 m (Kineke and Sternberg, 1995). Rather, outer topsets and foresets receive the majority of inner topset muds (Kineke and Sternberg, 1995).

The pathway from fluid mud reservoirs to foreset beds is responsible for very high sedimentation rates on the Amazon shelf, and may control the dominant clay mineralogy. The southeast Amazon shelf supplies most sediment to topset and foreset beds in suspension, resulting in lower accumulation rates (>1 cm/yr; Fig. 27; Kineke et al., 1996) coinciding with kaolinitic sediments (≤ 38%; Patchineelam and Figueiredo, 2000). Higher accumulation rates (>10 cm/yr) occur in the northwest where sediments cross the Cabo Norte Shoal, presumably in suspension, and are then transported across shelf as fluid mud (Kineke et al., 1996). Saltier water enhances the deposition of smectitic clays (>40%) to the north (Patchineelam and Figueiredo, 2000). The particular pathway of fluid mud trapping, transport, and deposition causes zones of highest smectite accumulation, not kaolinite, to correspond with the faintly laminated mud facies (Fig. 26; Kuehl et al., 1986). Unit 1 of the Marlboro Formation is similar to

the faintly laminated mud facies, receiving sediment as fluid mud, but with a more kaolinitic source.

Areas of highest smectite deposition have sedimentation rates (>10 cm/yr) in excess of those suggested for the Marlboro Formation (Wright and Schaller, 2013). However, couplets are only found in the kaolinitic portion of the Marlboro Formation, with thicknesses similar to the annual sedimentation on the southeast Amazon shelf (>1 cm/yr). If fluid mud is responsible for the couplets in the Marlboro Formation at Wilson Lake, it supports rapid deposition, and a short shallow marine timescale for the CIE (Wright and Schaller, 2013). Transport of fluid muds from inner topset to outer topset/foreset beds in the northwest Amazon shelf are reported to be discrete events recurring at intervals of 0.5-3 yrs (Sternberg et al., 1996; Kuehl et al., 1996).

The rapidly deposited muds of the Amazon shelf form a subaqueous delta with a clinoform morphology. Based on their similarities, I suggest the Marlboro Formation was part of a subaqueous delta in the Salisbury Embayment, and may have had characteristic topsets, foresets, and bottomsets (Fig. 24). Grain size uniformity in Units 1-3 implies that shoreline distance was static, so sediment was likely feeding the aggradation of a subaqueous delta. In the Amazon this coincides with a subtle facies progradation from foreset (40-60 m isobaths) to outer topset (20-40 m isobaths). This is shallower than recent estimates from benthic foraminifera for the Marlboro Formation depths of ~110 m from nearby Ancora (Harris et al., 2010). As the delta built upward nearer the rollover point, it would likely expose sediments to more storm action and wave energy than below. Unit 1 has a consistent clay assemblage and couplet thickness that may represent a foreset with high sedimentation (>1 cm/yr Amazon equivalent) and potential to preserve bedding. Unit 2 is marked by higher couplet variability, consistent with gradually increasing percent illite/smectite, and a change toward topset

deposition compared to the Amazon shelf. Unit 3 has high percent illite/smectite, higher percent smectite in illite/smectite, and a lack of laminations that suggest it was frequently reworked in a shallow topset.

Clinoform style deposition is consistent with environmental and sedimentary records from NJ cores. An environmental progression from long-term stratification to seasonal stratification was identified at Bass River and Wilson Lake A by Stassen et al. (2012). Water column mixing should be more common at updip locations as well as upcore. Envisioning the Marlboro Formation undergoing clinoform deposition also affects how the CIE is represented at different locations in an across-shelf transect (Fig. 24). Wilson Lake does not exhibit a recovery as noted at the Bass River corehole (Stassen et al., 2012), and mud may have been bypassing the area during that time. Likewise, the lower portion of the CIE record at Bass River and the paleoecologic zonations of Stassen et al. (2012) are described as condensed relative to Wilson Lake (Fig. 22). If the base of the Marlboro Formation at Bass River is compose of a distal foreset or bottomset, sedimentation may have been an order of magnitude less. Additionally, the presence of convoluted bedding (Fig. 28; Harris, 2010) at Ancora is consistent with a more steeply sloped depositional plane such as a foreset.

The recognition of 3 Units in the Marlboro Formation at Wilson Lake indicates a dynamic shelf analogous to the Amazon. As such, no single location in the Salisbury Embayment need necessarily preserve an uninterrupted Marlboro Formation (Kopp et al., 2009). Regardless of the preferred time scale for sedimentation rates at Wilson Lake, hiatuses may occur at long or short intervals. Deposition and erosion on the Amazon shelf are shown to fluctuate on 100 to 1000 yr time scales, due to the rapid sedimentation (≥10 cm/yr) relative to subsidence (15-22 cm/ky; Nittrouer et al., 1996). There are no major erosive surfaces in the Marlboro Formation at

Wilson Lake. Yet, the sharp kaolinite decrease in Unit 1 of Wilson Lake and in nearby Clayton, along with cessation of couplets at the Unit 2/3 boundary, represent two abrupt stratigraphic changes within the homogenous looking muds.

5.7 XRF Cyclicity

Cyclicity with a period ~2 cm in the Marlboro Formation may be explained by the signal of the laminae. However, this connection should be made cautiously. Laminae may be too thin for detection, depending on the interval, ranging from 0.4-0.6 mm. The scanning interval of these XRF, 0.5 mm, may not be detecting the swelling clays in a way that can be replicated. Breaks in the core, horizontal to the original orientation of the core, are often but not always aligned with laminae. These breaks are certainly detectable by the XRF in the plot of sample distance, and possibly the coherent and incoherent scattering. It is difficult to subtract out these effects since they contribute to each element profile in different proportions, and should not be eliminated altogether because many do correspond to laminae. If the spectral analysis returns a power at ~2 cm that is reinforced by core breaks and chemical signature, it may be identifying, but is not helping explain either factor.

6. Conclusions

Increasing proportions of kaolinite found in the Vincentown and Marlboro Formations are consistent with increased physical weathering and an intensified hydrologic cycle. The presence of a more altered variety of illite/smectite in the Vincentown Formation and the lowest meter of the Marlboro Formation indicates deposition was slower than in the rapidly deposited kaolinite and illite-rich clays that compose most of the Marlboro Formation. Kaolinite abundance in the Salisbury Embayment was probably at its highest levels when riverine input was great and salinity low, in the same way freshwater and kaolinite are linked on the Amazon

shelf today. Given the lack of clay data at other sites, the upsection kaolinite decrease near the top of the Marlboro Formation at Wilson Lake cannot be tied to basin-wide mineralogic changes. It is possibly the result of a reduction in freshwater and river input, and the slowing of the hydrologic cycle, or a phase of sediment bypass where kaolinite-rich clays are being transported to more distal foreset regions of the shelf.

Couplets and swelling clay laminations continue to be enigmatic features of the Marlboro Formation, but they may be genetically similar to the laminated mud facies on the Amazon shelf. Further work comparing the Amazon shelf cores to those from Wilson Lake and Millville, NJ could test this connection, as well as evaluating clay mineral changes through a modern subaqueous delta clinoform. A careful chemical analysis comparing laminations and drilling mud could also exclude the possibility that they were the result of contamination. Regardless of the composition of the swelling clay interlaminations, couplets at Wilson Lake only occur in the rapidly deposited, high-kaolinite interval and are attributed to a rapid sedimentary process.

Differences between the modern analog and the New Jersey paleoshelf are highlighted by the impact local seafloor structure and dominant ocean currents have on the mineralogic and lithofacies variations reported for the Amazon shelf. Still, modern mud-dominated shelves fall into a narrow range of categories, with known attributes, that can be compared to the Marlboro Formation. The subaqueous delta clinoform and marine dispersal dominated types represent two possible end-members to explain Marlboro Formation deposition. Both models should be considered when evaluating paleodepth, sedimentation rates, and the expression of the CIE at individual sites or in an across shelf transect. I have shown that clinoform deposition is consistent with the condensed and expanded onsets of the CIE reported between different sites

along one dip line. The validity of the clinoform model could be further investigated for foreset and bottomset sections along multiple dip lines in the Salisbury Embayment, and by measuring changing clay mineral abundance closer to the paleo-river source.

Fluid mud is a common feature of mud-dominated shelves today. Most Amazon River sediment is trapped in these nearshore reservoirs for weeks to months before being deposited distally to mid-shelf. Yet, the resulting sedimentary structures from this type of density-driven flow are not widely described in the literature. Fluid mud deposits are the preferred interpretation for Marlboro Formation bedding because they are expected to be fairly homogenous, fine-grained, lacking bioturbation, and the primary sediment source to a subaqueous delta foreset.

Finally, the sedimentation rates discussed for the Amazon shelf need not be applied directly to Wilson Lake. Uncertainties in river source location, drainage basin size, and accommodation space creation on the paleoshelf prohibit predictions based solely on sedimentology. The Amazon rates are useful for making relative comparisons, and predicting areas of highest and lowest sedimentation. Due to the dynamic shelf processes at work, long term sedimentation rates for the Amazon, beyond the century scale, are also unknown. The fluid mud connection with the Marlboro Formation suggests a yearly timescale for the emplacement of each bed.

7. References

Aubry, M.-P., Ouda, K., Dupuis, C., Berggren, W.A., and Van Couvering, J.A., 2007, The Global Standard Stratotype-section and Point (GSSP) for the base of the Eocene Series in the Dababiya section (Egypt): Episodes, v. 30, no. 4, p. 271–286.

Berggren, W.A., Alegret, L., Aubry, M.-P., Cramer, B.S., Dupuis, C., Goolaerts, S., Kent, D. V., King, C., Knox, R.W.O'B., Obaidalla, N., Ortiz, S., Ouda, K.A.K., Abdel-Sabour, A., Salem, R., Senosy, M.M., Soliman, M.F., Soliman, A., 2012, The Dababiya corehole, Upper Nile Valley, Egypt: Preliminary results: Austrian Journal of Earth Sciences, v. 105, no. 1, p. 161–168.

Bowen, G.J., Koch, P.L., Gingerich, P.D., Norris, R.D., Bains, S., and Corfield, R.M., 2001, Refined Isotope Stratigraphy Across the Continental Paleocene-Eocene Boundary on Polecat Bench in the Northern Bighorn Basin, *in* Paleocene-Eocene Stratigraphy and Biotic Change in the Bighorn and Clarks Fork Basins, Wyoming, University of Michigan Papers on Paleontology, v. 33, p. 73–88.

Brindley, G.W., and Brown, G., 1980, Crystal structures of clay minerals and their X-ray identification, *in* Mineralogical Society Monograph; no. 5, Mineralogical Society, London, England.

Buffett, B., and Archer, D., 2004, Global inventory of methane clathrate: sensitivity to changes in the deep ocean: Earth and Planetary Science Letters, v. 227, no. 3-4, p. 185–199, doi: 10.1016/j.epsl.2004.09.005.

Cramer, B.S., Aubry, M.-P., Miller, K.G., Olsson, R.K., Wright, J.D., and Kent, D.V., 1999, An exceptional chronologic, isotopic, and clay mineralogic record of the latest Paleocene thermal maximum, Bass River, NJ, ODP 174AX: Bull. Soc. geol. France, v. 170, no. 6, p. 883–897.

Croudace, I.W., Rindby, A., and Rothwell, R.G., 2006, ITRAX: description and evaluation of a new multi-function X-ray core scanner: Geological Society, London, Special Publications, v. 267, no. 1, p. 51–63, doi: 10.1144/GSL.SP.2006.267.01.04.

DeConto, R.M., Galeotti, S., Pagani, M., Tracy, D., Schaefer, K., Zhang, T., Pollard, D., and Beerling, D.J., 2012, Past extreme warming events linked to massive carbon release from thawing permafrost: Nature, v. 484, no. 7392, p. 87–91, doi: 10.1038/nature10929.

Dickens, G.R., Castillo, M.M., and Walker, J.C.G., 1997, A blast of gas in the latest Paleocene: Simulating first-order effects of massive dissociation of oceanic methane hydrate: Geology, v. 25, no. 3, p. 259–262, doi: 10.1130/0091-7613(1997)025<0259.

Dickens, G.R., Neil, J.R.O., Rea, D.K., and Owen, R.M., 1995, Dissociation of oceanic methane hydrate as a cause of the carbon isotope excursion at the end of the Paleocene: Paleoceanography, v. 10, no. 6, p. 965–971.

Gibbs, R.J., 1976, Amazon River sediment transport in the Atlantic Ocean: Geology, v. 4, p. 45–48.

Gibson, T.G., Bybell, L.M., and Owens, J.P., 1993, Latest Paleocene Lithologic and Biotic Events in Neritic Deposits of Southwestern New Jersey: Paleoceanography, v. 8, no. 4, p. 495–514.

Gibson, T.G., Bybell, L.M., and Mason, D.B., 2000, Stratigraphic and climatic implications of clay mineral changes around the Paleocene/Eocene boundary of the northeastern US margin: Sedimentary Geology, v. 134, no. 1-2, p. 65–92, doi: 10.1016/S0037-0738(00)00014-2.

Glaser, J.D., 1971, Geology of mineral resources of southern Maryland: Maryland Geological Survey Report of Investigations Volume 15: Maryland Geological Survey, p. 1-85.

Griffin, J.J., Windom, H., and Goldberg, E.D., 1968, The distribution of clay minerals in the World Ocean: Deep-Sea Research, v. 15, p. 433–459.

Harris, A.D., 2010, Integrated Sequence Stratigraphy of the Paleocene-Lowermost Eocene, New Jersey Coastal Plain: Implications for Eustatic and Paleoceanographic Change, Ph.D. Thesis, p. 183

Harris, A.D., Miller, K.G., Browning, J.V., Sugarman, P.J., Olsson, R.K., Cramer, B.S., and Wright, J.D., 2010, Integrated stratigraphic studies of Paleocene – lowermost Eocene sequences, New Jersey Coastal Plain: Evidence for glacioeustatic control: Paleoceanography, v. 25, p. 1–18, doi: 10.1029/2009PA001800.

Higgins, J.A., and Schrag, D.P., 2006, Beyond methane: Towards a theory for the Paleocene–Eocene Thermal Maximum: Earth and Planetary Science Letters, v. 245, no. 3-4, p. 523–537, doi: 10.1016/j.epsl.2006.03.009.

Inoue, A., Bouchet, A., Velde, B., and Meunier, A., 1989, Convenient Technique for Estimating Smectite Layer Percentage in Randomly Interstratified Illite/Smectite Minerals: Clays and Clay Minerals, v. 37, no. 3, p. 227–234.

John, C.M., Banerjee, N.R., Longstaffe, F.J., Sica, C., Law, K.R., and Zachos, J.C., 2012, Clay assemblage and oxygen isotopic constraints on the weathering response to the Paleocene-Eocene thermal maximum, east coast of North America: Geology, v. 40, no. 7, p. 591–594, doi: 10.1130/G32785.1.

Katz, M.E., Pak, D.K., Dickens, G.R., and Miller, K.G., 1999, The Source and Fate of Massive Carbon Input During the Latest Paleocene Thermal Maximum: Science, v. 286, no. 5444, p. 1531–1533, doi: 10.1126/science.286.5444.1531.

Kennett, J.P., and Stott, L.D., 1991, Palaeoceanographic warming, Abrupt deep-sea and benthic extinctions at the end changes of the Palaeocene: Nature, v. 353, p. 225-229.

Kent, D.V., Cramer, B.S., Lanci, L., Wang, D., Wright, J.D., and Van der Voo, R., 2003, A case for a comet impact trigger for the Paleocene/Eocene thermal maximum and carbon isotope excursion: Earth and Planetary Science Letters, v. 211, no. 1-2, p. 13–26, doi: 10.1016/S0012-821X(03)00188-2.

Kineke, G.C., and Sternberg, R.W., 1995, Distribution of fluid muds on the Amazon continental shelf: Marine Geology, v. 125, no. 3-4, p. 193–233, doi: 10.1016/0025-3227(95)00013-O.

Kineke, G.C., Sternberg, R.W., Trowbridge, J.H., and Geyer, W.R., 1996, Fluid-mud processes on the Amazon continental shelf: Continental Shelf Research, v. 16, no. 516, p. 667–696.

Koch, P.L., Zachos, J.C., and Gingerich, P.D., 1992, Correlation between isotope records in marine and continental carbon reservoirs near the Paleocene/Eocene boundary: Nature, v. 358, p. 319–322.

Kopp, R.E., Raub, T.D., Schumann, D., Vali, H., Smirnov, A.V., and Kirschvink, J.L., 2007, Magnetofossil spike during the Paleocene-Eocene thermal maximum: Ferromagnetic resonance, rock magnetic, and electron microscopy evidence from Ancora, New Jersey, United States: Paleoceanography, v. 22, no. 4, p. 1-7, doi: 10.1029/2007PA001473.

Kopp, R.E., Schumann, D., Raub, T.D., Powars, D.S., Godfrey, L.V., Swanson-Hysell, N.L., Maloof, A.C., and Vali, H., 2009, An Appalachian Amazon? Magnetofossil evidence for the development of a tropical river-like system in the mid-Atlantic United States during the Paleocene-Eocene thermal maximum: Paleoceanography, v. 24, no. 4, p. 1-18, doi: 10.1029/2009PA001783.

Kuehl, S.A., DeMaster, D.J., and Nittrouer, C.A., 1986a, Nature of sediment accumulation on the Amazon continental shelf: Continental Shelf Research, v. 6, p. 209–235.

Kuehl, S.A., Nittrouer, C.A., and Allison, M.A., 1996, Sediment deposition, accumulation , and seabed dynamics in an energetic fine-grained coastal environment: Continental Shelf Research, v. 16, no. 516, p. 787–815.

Kuehl, S., Nittrouer, C.A., and DeMaster, D.J., 1986b, Distribution of sedimentary structures in the Amazon Subaqueous delta: Continental Shelf Research, v. 6, no. 1, p. 311–336.

Kurtz, A.C., Kump, L.R., Arthur, M. A., Zachos, J.C., and Paytan, A., 2003, Early Cenozoic decoupling of the global carbon and sulfur cycles: Paleoceanography, v. 18, no. 4, p. 1-14, doi: 10.1029/2003PA000908.

Lippert, P.C., and Zachos, J.C., 2007, A biogenic origin for anomalous fine-grained magnetic material at the Paleocene-Eocene boundary at Wilson Lake, New Jersey: Paleoceanography, v. 22, no. 4, p. 1-8, doi: 10.1029/2007PA001471.

Lyle, M., Lyle, A.O., Gorgas, T., Holbourn, A., Westerhold, T., Hathorne, E., Kimoto, K., and Yamamoto, S., 2012, Data report: raw and normalized elemental data along the Site U1338 splice from X-ray fluorescence scanning, *in* Proceedings of the Integrated Ocean Drilling Program, Volume 320/321, 1-19.

Makarova, M., Miller, K.G., Wright, J.D., Rosenthal, Y., Babila, T., and Browning, J.V., 2013, Abstract: Paleoenvironmental changes associated with the PETM, Millville (ODP Leg 174AX), New Jersey coastal plain: American Geophysical Union Annual Meeting, p. 1–2.

McCave, I.N., Manighetti, B., and Robinson, S.G., 1995, Sortable silt and fine sediment size/composition slicing: Parameters for palaeocurrent speed and paleoceanography: Paleoceanography, v. 10, no. 3, p. 593–610.

Miller, K.G., Sugarman, P.J., Van Fossen, M., Liu, C., Browning, J.V., Queen, D., Aubry, M., Burckle, L.D., Goss, M., and Bukry, D., 1994, 1. Island Beach Site Report, *in* Proceedings of the Ocean Drilling Program, Initial Reports, Vol. 150X, p. 5-59.

Miller, K.G., Browning, J.V., Sugarman, P.J., McLaughlin, P.P., Kominz, M.A., Olsson, R.K., Wright, J.D., Cramer, B.S., Pekar, S.F., and Van Sickel, W., 2002, 174AX Leg Summary: Sequences, Sea Level, Tectonics, and Aquifer Resources: Coastal Plain Drilling, *in* Proceedings of the International Drilling Program, Initial Reports Volume 174AX (Suppl.), p. 1–38.

Miller, K.G., Sugarman, P.J., Browning, J.V., McLaughlin, P.P., Baluyot, R.D., Karakaya, S., Lombardi, C.J., McCreary, S., Monteverde, D.H., Smith, T., Babila, T., Martin, L., Catherine, C., Esmeray, S., Miller, R., Bord, D., Feigenson, M.D., Curran, J., in prep, Wilson Lake Hole B Report, p. 1–30.

Mixon, R.B., Pavlides, L., Powars, D.S., Froelich, A.J., Weems, R.E., Schindler, J.S., Newell, W.L., Edwards, L.E., and Ward, L.W., 2000, Geologic Map of the Fredericksburg 30’ x 60' Quadrangle, Virginia and Maryland: United States Geological Survey Geologic Investigations Series Map I-2607 scale 1:100,000, 2 sheets.

Moore, D., and Reynolds, R., 1997, X-ray Diffraction and the Identification and Analysis of Clay Minerals: Oxford University.

Murphy, B.H., Farley, K.A., and Zachos, J.C., 2010, An extraterrestrial 3He-based timescale for the Paleocene–Eocene thermal maximum (PETM) from Walvis Ridge, IODP Site 1266: Geochimica et Cosmochimica Acta, v. 74, no. 17, p. 5098–5108, doi: 10.1016/j.gca.2010.03.039.

Nittrouer, C.A., Kuehl, S.A., Figueiredo, A.G., Mead, A.A., Sommerfield, C.K., Rine, J.M., Faria, L.E.C., and Silveira, O.M., 1996, The geological record preserved by Amazon shelf sedimentation: Continental Shelf Research, v. 16, p. 817–841.

Nittrouer, C.A., Sharara, M.T., and Demaster, D.J., 1983, Variations of Sediment Texture on the Amazon Continental Shelf: Journal of Sedimentary Research, v. 53, no. 82, p. 179–191.

Patchineelam, S.M., and Figueiredo, A.G. de, 2000, Preferential settling of smectite on the Amazon continental shelf: Geo-Marine Letters, p. 37–42.

Patterson, M.V., and Francis, D., 2013, Kimberlite eruptions as triggers for early Cenozoic hyperthermals: Geochemistry, Geophysics, Geosystems, v. 14, no. 2, p. 448–456, doi: 10.1002/ggge.20054.

Röhl, U., Westerhold, T., Bralower, T.J., and Zachos, J.C., 2007, On the duration of the Paleocene-Eocene thermal maximum (PETM): Geochemistry Geophysics Geosystems, v. 8, no. 12, p. Q12002, doi: 10.1029/2007GC001784.

Rothwell, R.G., 2006, New Techniques in Sediment Core Analysis, Geological Society Special Publication v. 267, p. 1-269.

Self-Trail, J.M., Powars, D.S., Watkins, D.K., and Wandless, G. A., 2012, Calcareous nannofossil assemblage changes across the Paleocene–Eocene Thermal Maximum: Evidence from a shelf setting: Marine Micropaleontology, v. 92-93, p. 61–80, doi: 10.1016/j.marmicro.2012.05.003.

Sluijs, A., Brinkhuis, H., Schouten, S., Bohaty, S.M., John, C.M., Zachos, J.C., Reichart, G.-J., Sinninghe Damsté, J.S., Crouch, E.M., and Dickens, G.R., 2007, Environmental precursors to rapid light carbon injection at the Palaeocene/Eocene boundary: Nature, v. 450, no. 7173, p. 1218–21, doi: 10.1038/nature06400.

Sluijs, A., Schouten, S., Pagani, M., Woltering, M., Brinkhuis, H., Damsté, J.S.S., Dickens, G.R., Huber, M., Reichart, G.-J., Stein, R., Matthiessen, J., Lourens, L.J., Pedentchouk, N., Backman, J., Moran, K., & the Expedition 302 Scientists., 2006, Subtropical Arctic Ocean temperatures during the Palaeocene/Eocene thermal maximum: Nature, v. 441, no. 7093, p. 610–613, doi: 10.1038/nature04668.

Sommerfield, C.K., Nittrouer, C.A., and Figueiredo, A.G., 1995, Stratigraphic evidence of changes in Amazon shelf sedimentation during the late Holocene: Marine Geology, v. 125, p. 351–371.

Stassen, P., Thomas, E., and Speijer, R.P., 2012a, Restructuring outer neritic foraminiferal assemblages in the aftermath of the Paleocene-Eocene thermal maximum: Journal of Micropalaeontology, v. 31, no. 1, p. 89–93, doi: 10.1144/0262-821X11-026.

Stassen, P., Thomas, E., and Speijer, R.P., 2012b, The progression of environmental changes during the onset of the Paleocene-Eocene thermal maximum (New Jersey Coastal Plain): Austrian Journal of Earth Sciences, v. 105, no. 1, p. 169–178.

Sternberg, R.W., Cacchione, D.A., Paulson, B., and Drake, D.E., 1996, Observations of sediment transport on the Amazon subaqueous delta: Continental Shelf Research, v. 16, no. 5, p. 697–715.

Storey, M., Duncan, R. A., and Swisher, C.C., 2007, Paleocene-Eocene thermal maximum and the opening of the Northeast Atlantic: Science, v. 316, no. 5824, p. 587–9, doi: 10.1126/science.1135274.

Sugarman, P.J., Miller, K.G., Browning, J.V., Aubry, M.-P., Brenner, G.J., Bukry, D., Butari, B., Feigenson, M.D., Kulpecz, A.A., McLaughlin, P.P., Jr., Mizintseva, S., Monteverde, D.H., Olsson, R., Pusz, A., Rancan, H., Tomlinson, J., Uptegrove, J., and Velez, C.C., 2010, Medford Site, *in* Miller, K.G., Sugarman, P.J., Browning, J.V., and et al., eds., Proceedings of the Ocean Drilling Program, Initial reports, Volume 174AX (supplement): College Station, TX, p. 1-93.

Sugarman, P.J., Miller, K.G., Browning, J.V., McLaughlin, P.P., Jr., Brenner, G.J., Buttari, B., Cramer, B.S., Harris, A., Hernandez, J., Katz, M.E., Lettini, B., Misintseva, S., Monteverde, D.H., Olsson, R.K., Patrick, L., Roman, E., Wojtko, M.J., Aubry, M.-P., Feigenson, M.D., Barron, J.A., Curtin, S., Cobbs, G., Cobbs, G., III, Bukry, D., and Huffman, B., 2005, Millville Site, *in* Miller, K.G., Sugarman, P.J., Browning, J.V., et al., eds., Proceedings of the Ocean Drilling Program, Initial reports, Volume 174AX (Suppl.): College Station, TX, Ocean Drilling Program, p. 1-94.

Svensen, H., Planke, S., Malthe-Sørenssen, A., Jamtveit, B., Myklebust, R., Eidem, T.R., and Rey, S.S., 2004, Release of methane from a volcanic basin as a mechanism for initial Eocene global warming: Nature, v. 429, p. 542–545, doi: 10.1038/nature02575.1.

Thiry, M., and Jacquin, T., 1993, Clay mineral distribution related to rift activity, sea-level changes and paleoceanography in the Cretaceous of the Atlantic Ocean: Clay Minerals, v. 28, p. 61–84.

Thomson, J., Croudace, I.W., and Rothwell, R.G., 2006, A geochemical application of the {ITRAX} scanner to a sediment core containing eastern Mediterranean sapropel units: Geological Society, London, Special Publications, v. 267, no. 1, p. 65–77, doi: 10.1144/GSL.SP.2006.267.01.05.

Walsh, J.P., and Nittrouer, C.A., 2009, Understanding fine-grained river-sediment dispersal on continental margins: Marine Geology, v. 263, p. 34–45, doi: 10.1016/j.margeo.2009.03.016.

Wang, H., Kent, D.V., and Jackson, M.J., 2013, Evidence for abundant isolated magnetic nanoparticles at the Paleocene-Eocene boundary: Proceedings of the National Academy of Sciences of the United States of America, v. 110, no. 2, p. 425–30, doi: 10.1073/pnas.1205308110.

Watts, A.B., and Thorne, J., 1984, Tectonics, global changes in sea level and their relationship to stratigraphical sequences at the US Atlantic continental margin: Marine and Petroleum Geology, v. 1, no. 1977, p. 319–339.

Weltje, G.J., and Tjallingii, R., 2008, Calibration of XRF core scanners for quantitative geochemical logging of sediment cores: Theory and application: Earth and Planetary Science Letters, v. 274, no. 3-4, p. 423–438, doi: 10.1016/j.epsl.2008.07.054.

Wing, S.L., Harrington, G.J., Smith, F.A., Bloch, J.I., Boyer, D.M., and Freeman, K.H., 2005, Transient floral change and rapid global warming at the Paleocene-Eocene boundary: Science, v. 310, no. 5750, p. 993–6, doi: 10.1126/science.1116913.

Wright, J.D., and Schaller, M.F., 2013, Evidence for a rapid release of carbon at the Paleocene-Eocene thermal maximum: Proceedings of the National Academy of Sciences of the United States of America, no. 23, p. 1–6, doi: 10.1073/pnas.1309188110.

Zachos, J.C., Schouten, S., Bohaty, S., Quattlebaum, T., Sluijs, A., Brinkhuis, H., Gibbs, S.J., and Bralower, T.J., 2006, Extreme warming of mid-latitude coastal ocean during the Paleocene-Eocene Thermal Maximum: Inferences from TEX86 and isotope data: Geology, v. 34, no. 9, p. 737, doi: 10.1130/G22522.1.

Zachos, J.C., Wara, M.W., Bohaty, S., Delaney, M.L., Petrizzo, M.R., Brill, A., Bralower, T.J., and Premoli-Silva, I., 2003, A transient rise in tropical sea surface temperature during the Paleocene-Eocene thermal maximum: Science, v. 302, no. 5650, p. 1551–4, doi: 10.1126/science.1090110.

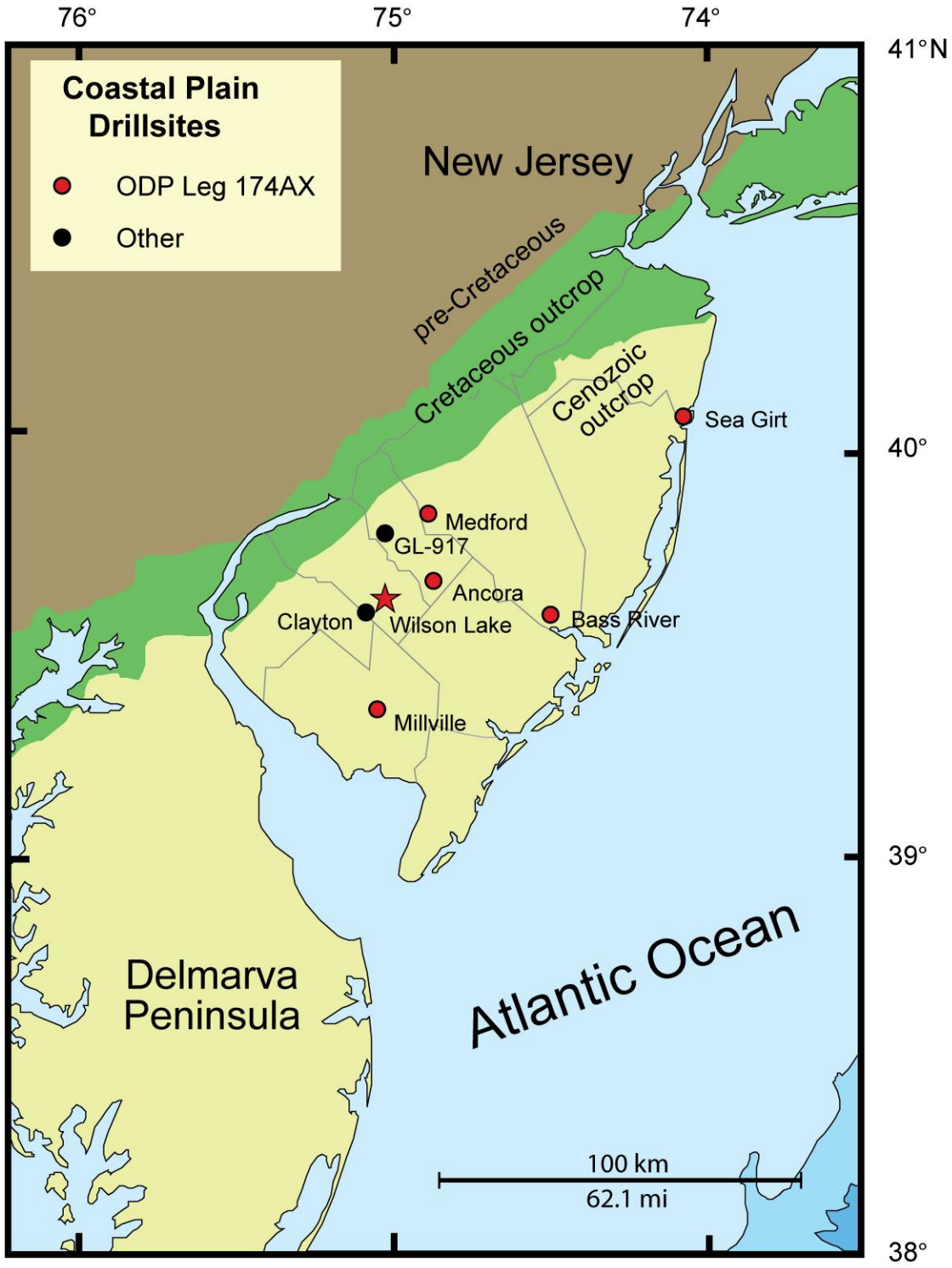

Figure 1. Map of Coreholes in the New Jersey Coastal Plain.

Shown are sites where the Marlboro Formation has been recovered in New Jersey, and the subject of this study (Wilson Lake) is starred. The strike of the outcropping strata, between pre-Cretaceous and Cretaceous, approximates the strike of all coastal plain strata. County lines (gray) are included for context.

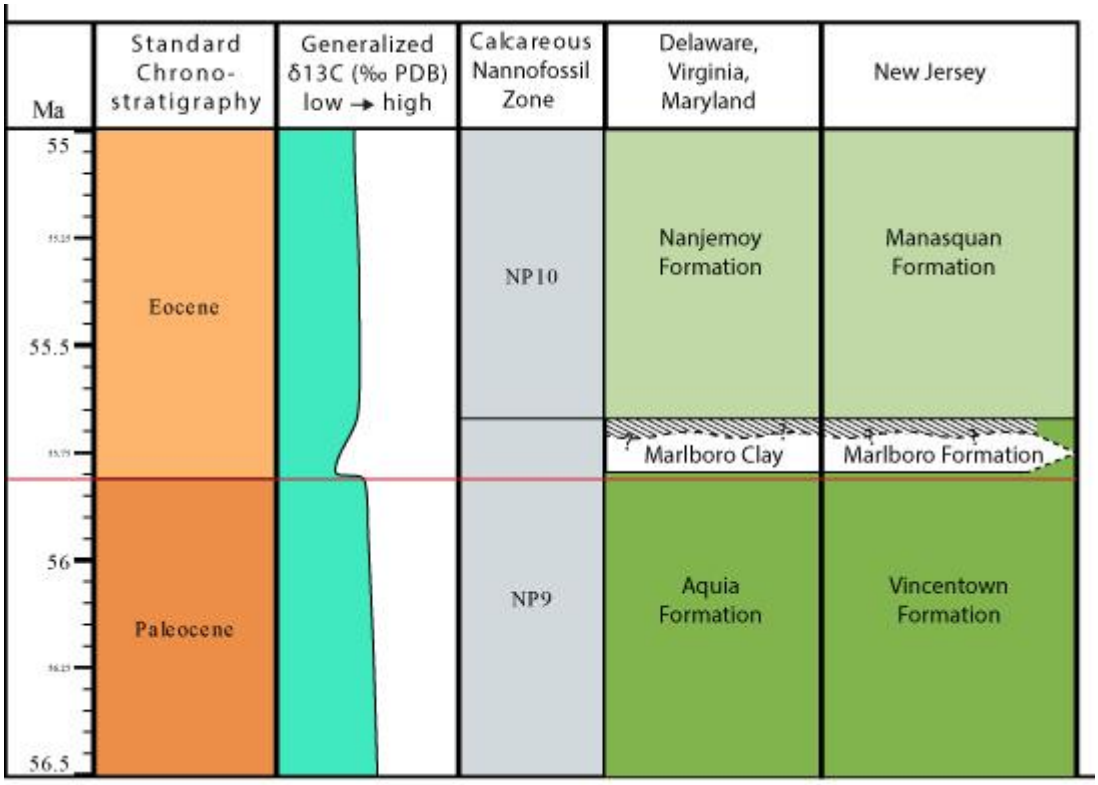

Figure 2. Comparison of Regional Stratigraphy.

The red line traces the level of the onset of the Carbon Isotope Excursion and the Paleocene-Eocene boundary as defined by Aubry et al. (1997). Lithostratigraphic nomenclature differs in the Northern and Southern parts of the basin, with the exception of the Marlboro Clay and Formation (both units having Formation status). The Marlboro Formation is not present at all New Jersey coreholes, and two locations document Vincentown lithology both above and below it. Modified after Gibson et al. (2000) to reflect the recognition of the Marlboro Formation in New Jersey.

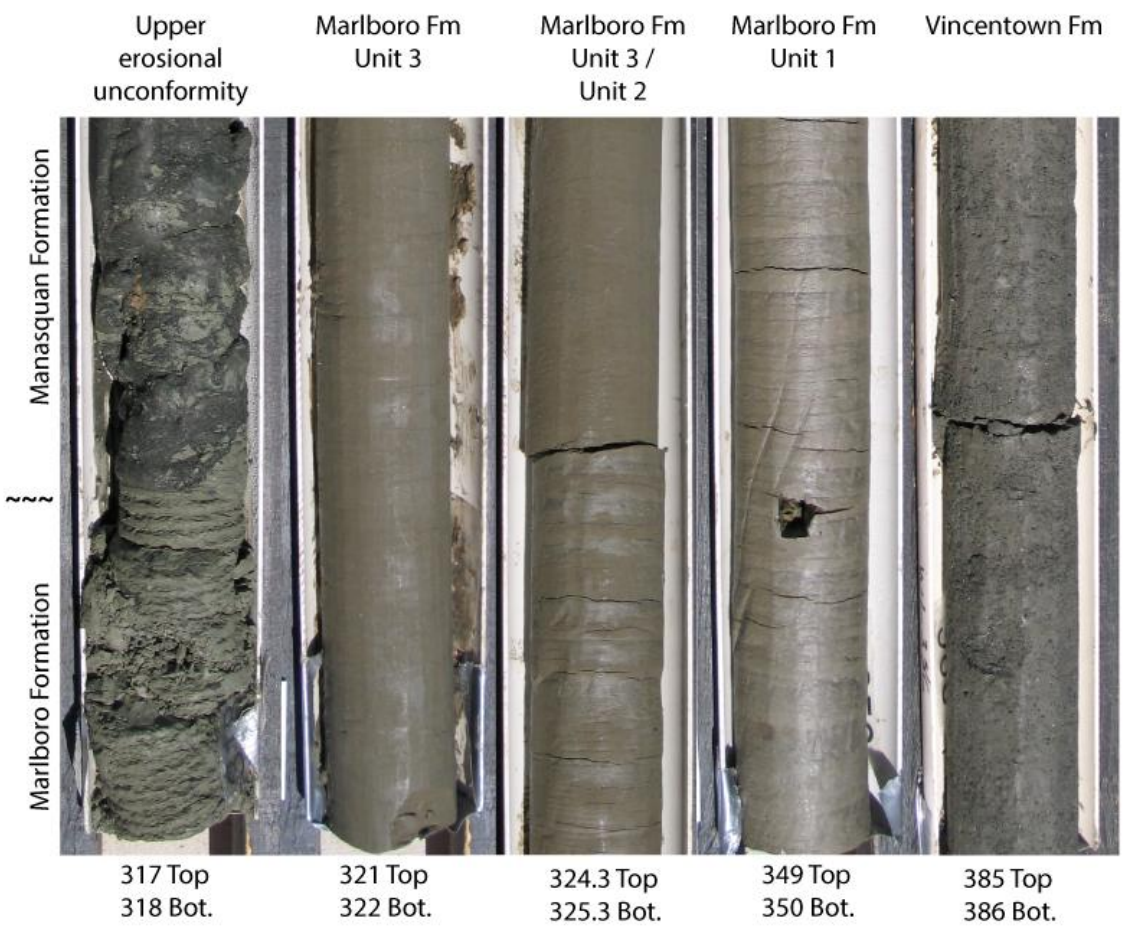

Figure 3. Vincentown, Marlboro, and Manasquan Fm. Core Photographs.

Note the visible coarse sediment fraction in the Vincentown and Manasquan Formations, compared to the clayey silt of the Marlboro Formation. The Marlboro Formation cores also appear lighter where more kaolinitic (Unit 1) and glossy where laminated (Unit 1 and 2).

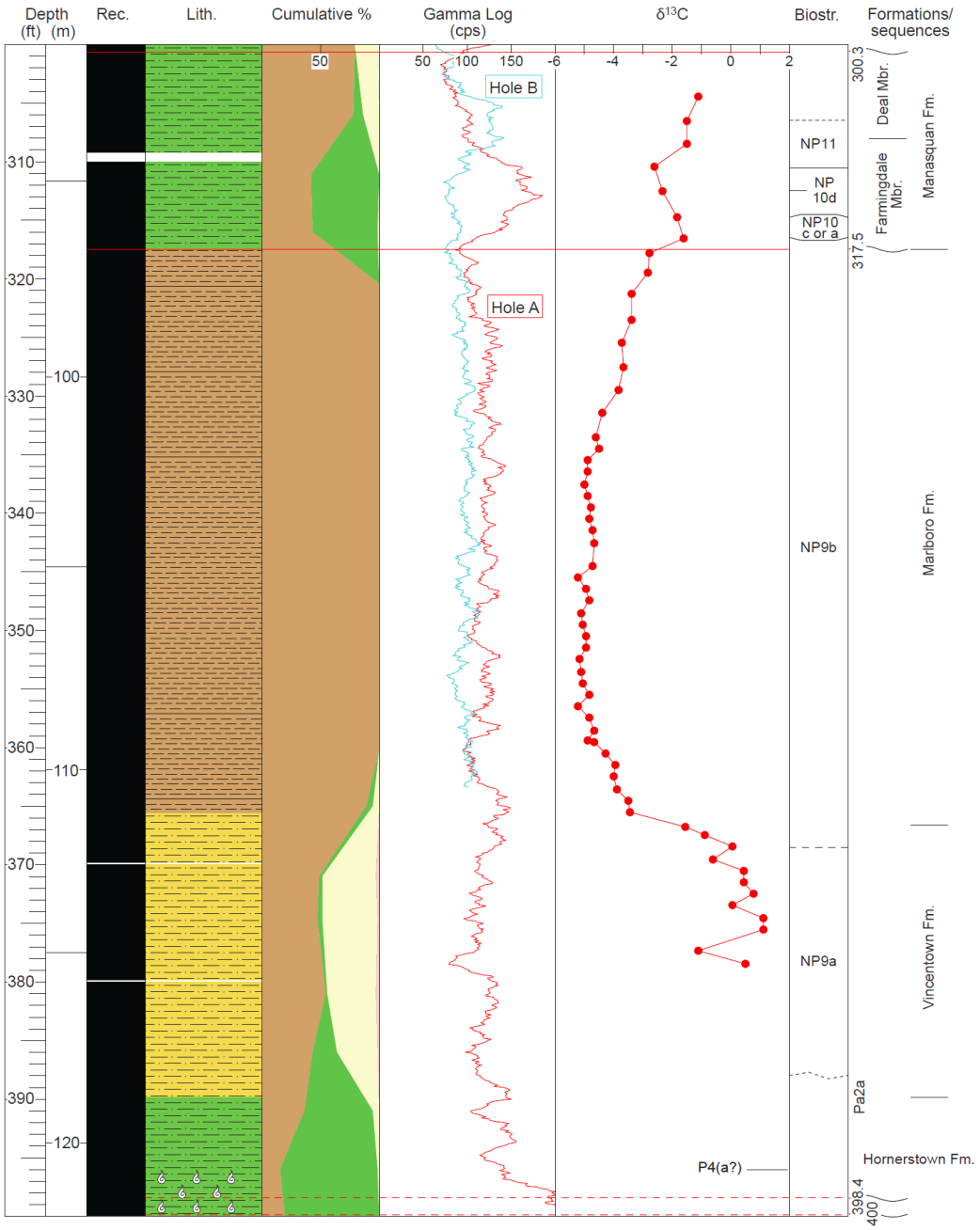

Figure 4. Lithology of the Hornerstown, Vincentown, Marlboro, and Manasquan Formations.

Left column shows depth below surface in feet and meters. Black column is core recovery, white denoting coring gaps. Lithology column shows predominantly glauconitic silty sands as green, quartzose silty sands as yellow, and clayey silts as brown. The cumulative percent lithology denotes brown as clay and silt sized particles, green as glauconite sand particles, and yellow/tan as fine sand. Gamma logs are red for Wilson Lake hole B, and blue for Wilson Lake hole A. Carbon isotopes in red shows sample locations as circles. Calcareous nannofossil zones are reported next to common lithostratigraphic nomenclature for the NJ coastal plain. Unconformities are displayed as red horizontal solid and dashed lines. From the Wilson Lake Site Report, Miller et al. (in prep).

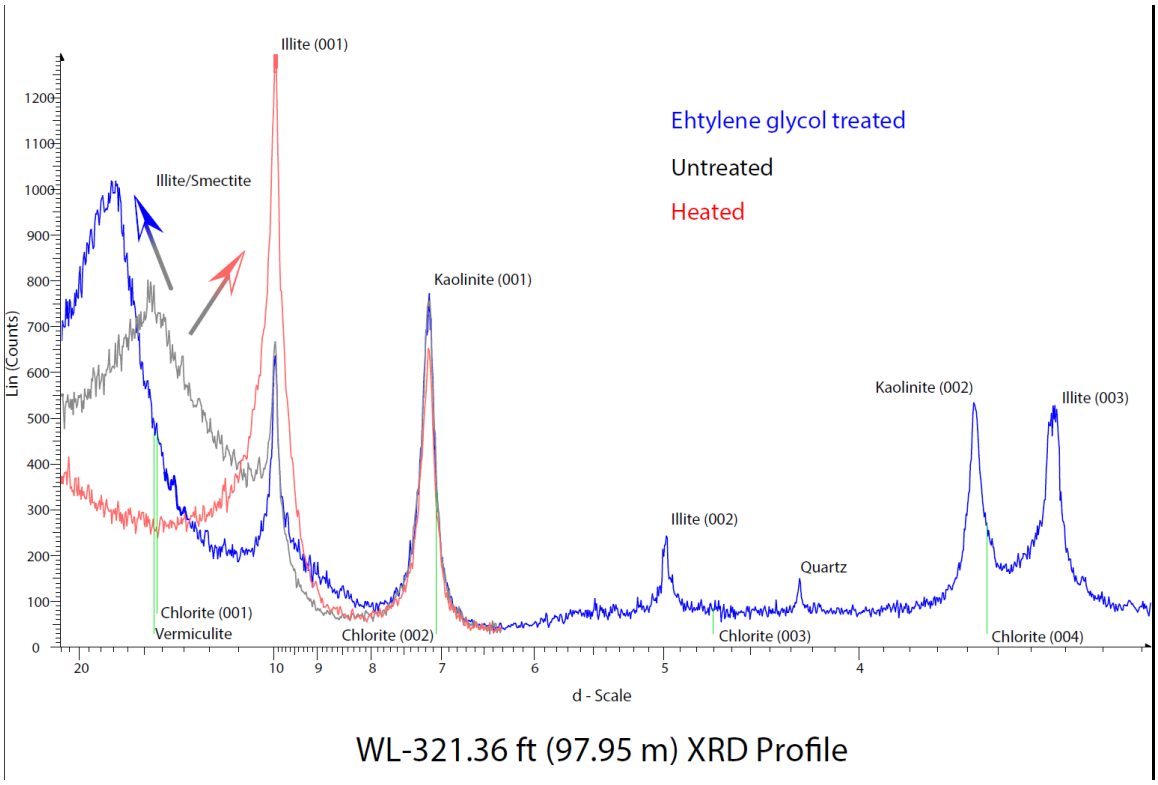

Figure 5. Clay Diffractogram.

Plot of XRD results from 3 differently prepared slides from one core sample. All peaks remain stationary between treatments except illite/smectite. Shifting of peaks (arrows) allows positive identification of different types of swelling, interlayered clays. Chlorite and vermiculite, not abundant here, positions are indicated (green). Trace amounts are recognized in the strongest peak chlorite(004) after deconvoluting from the overlapping kaolinite curve. Peaks were measured at chlorite and vermiculite locations above a projected background curve, even when obscure, to identify any possible trends.

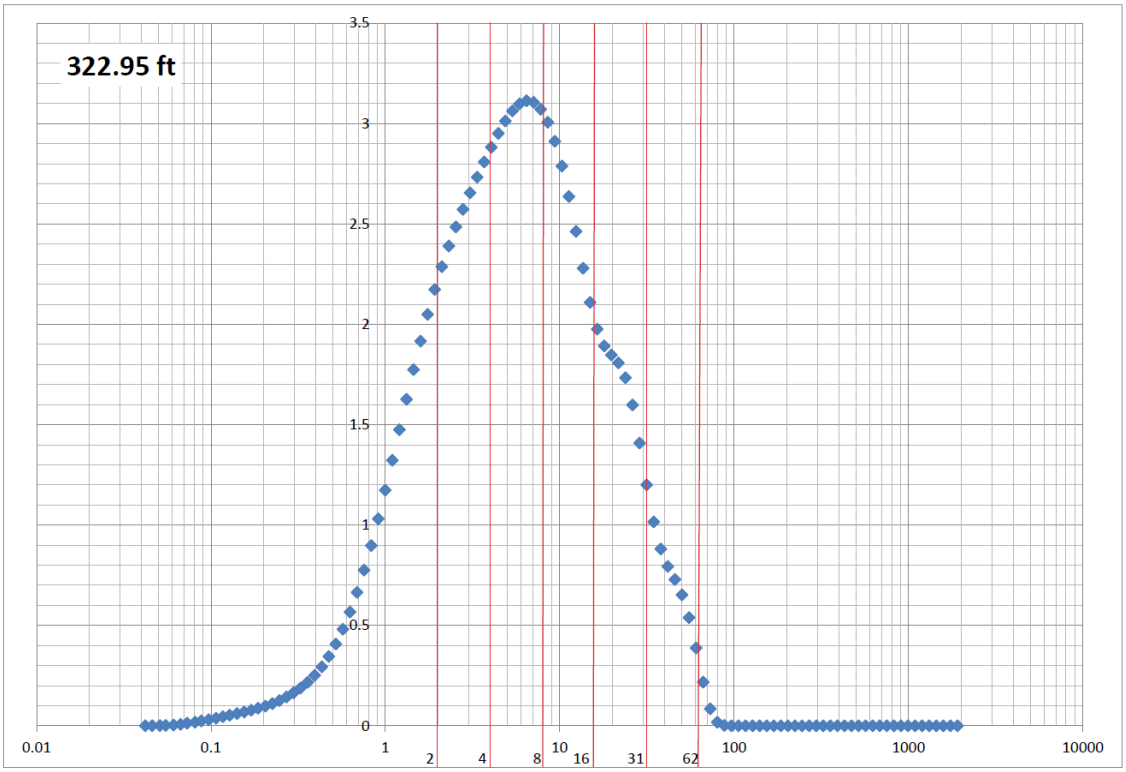

Figure 6. Example Grain Size Distribution.

X-axis is grain size diameter plotted logarithmically with red lines denoting common size divisions at 2 (upper clay boundary for XRD analysis), 4 (upper clay boundary), 8 (upper boundary of very fine silt), 16 (upper boundary of fine silt), 31 (upper boundary medium silt), and 62 (upper boundary coarse silt). Y-axis is percent volume. Sample 322.95 ft.

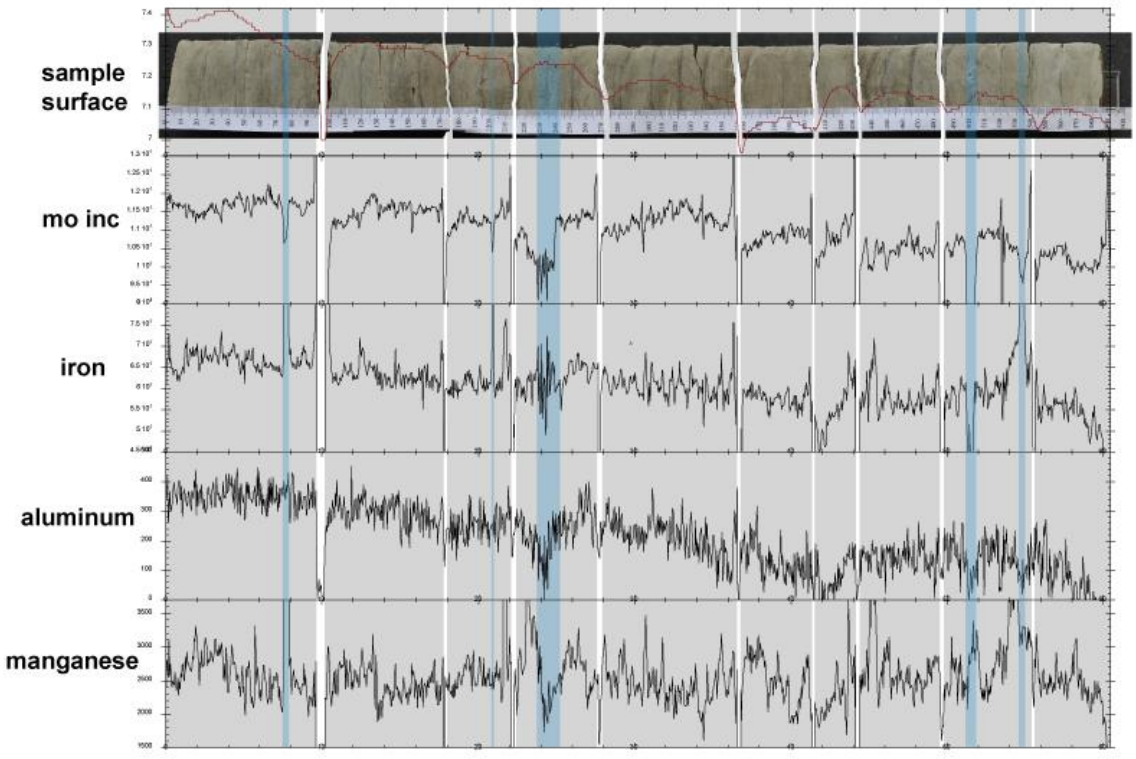

Figure 7. 346-348 ft XRF Core Alignment.

Example of notable elemental plots. Depicted from top to bottom are Sample Surface, Mo Inc, Iron, Aluminum, and Manganese. Sample surface, a proxy for core thickness, overprints many of the elemental profiles. Blue shading denotes coarse sand size nodules present.

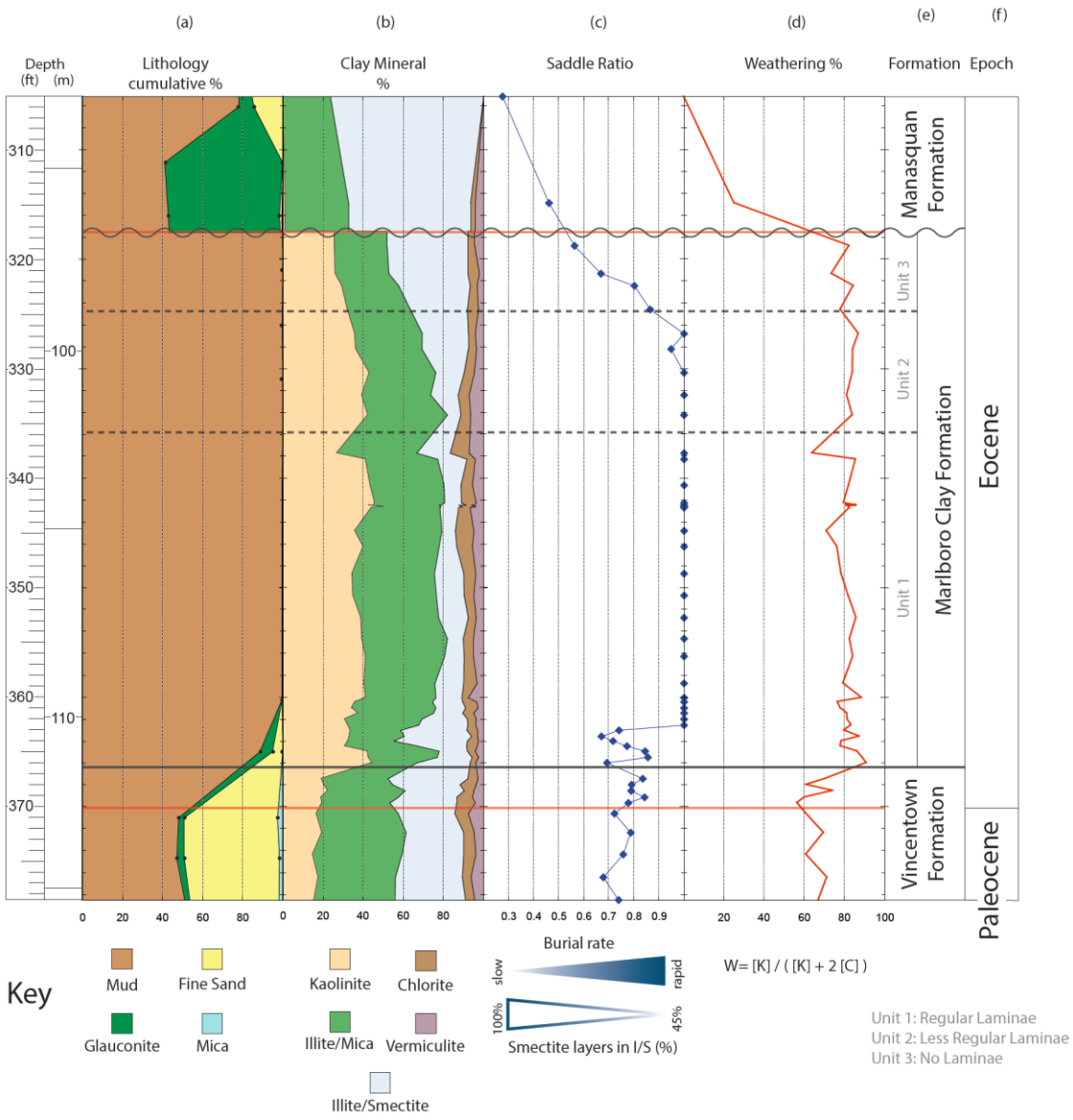

Figure 8. Clay Mineral Stratigraphy.

Cumulative lithology column (a) identifies the fine-grained Marlboro Formation between solid black horizontal line below and a wavy horizontal line above. Clay minerals (b) show the trend of increased kaolinite deposition caused by increased physical weathering starting in the Vincentown Formation and increasing dramatically in the Marlboro Formation. The base of Unit 1 is also shown to be transitional in terms of Saddle Ratio (c) and % illite/smectite. Relative clay mineral % (b) identifies an abrupt change near the base of Unit 2 possibly related to a freshwater decrease to the Wilson Lake paleo-shelf. Unit 3 (e) is identifiable by lower saddle ratios indicating reworked or slowly deposited illite/smectite. The contribution of illite and illite-like minerals (mica, glauconite) is relatively consistent among clay sized particles as shown in I002/I001 peak ratios.

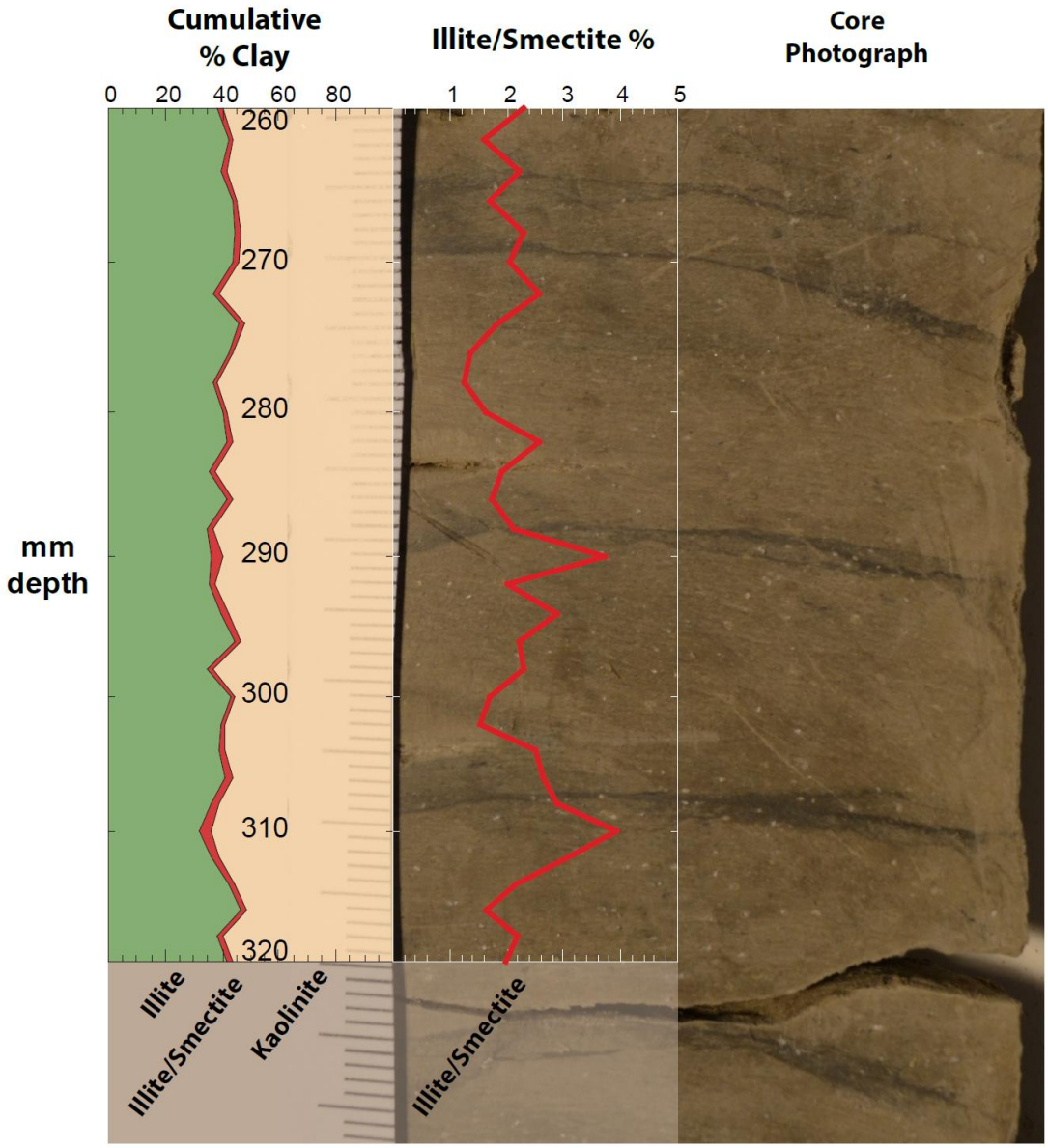

Figure 9. Clay microstratigraphy from 346-348 ft.

Plots of cumulative % clay and % illite/smectite overlay a close-up photograph of the interval 260-320 mm below the top of the 346-348 ft (105.46-106.07 m) core section. Samples were taken continuously as chips 2 mm in length and includes at least 3 of the 0.5-1 mm thick swelling clay laminations. The % smectite shows a minor increase in samples nearest to the laminae.

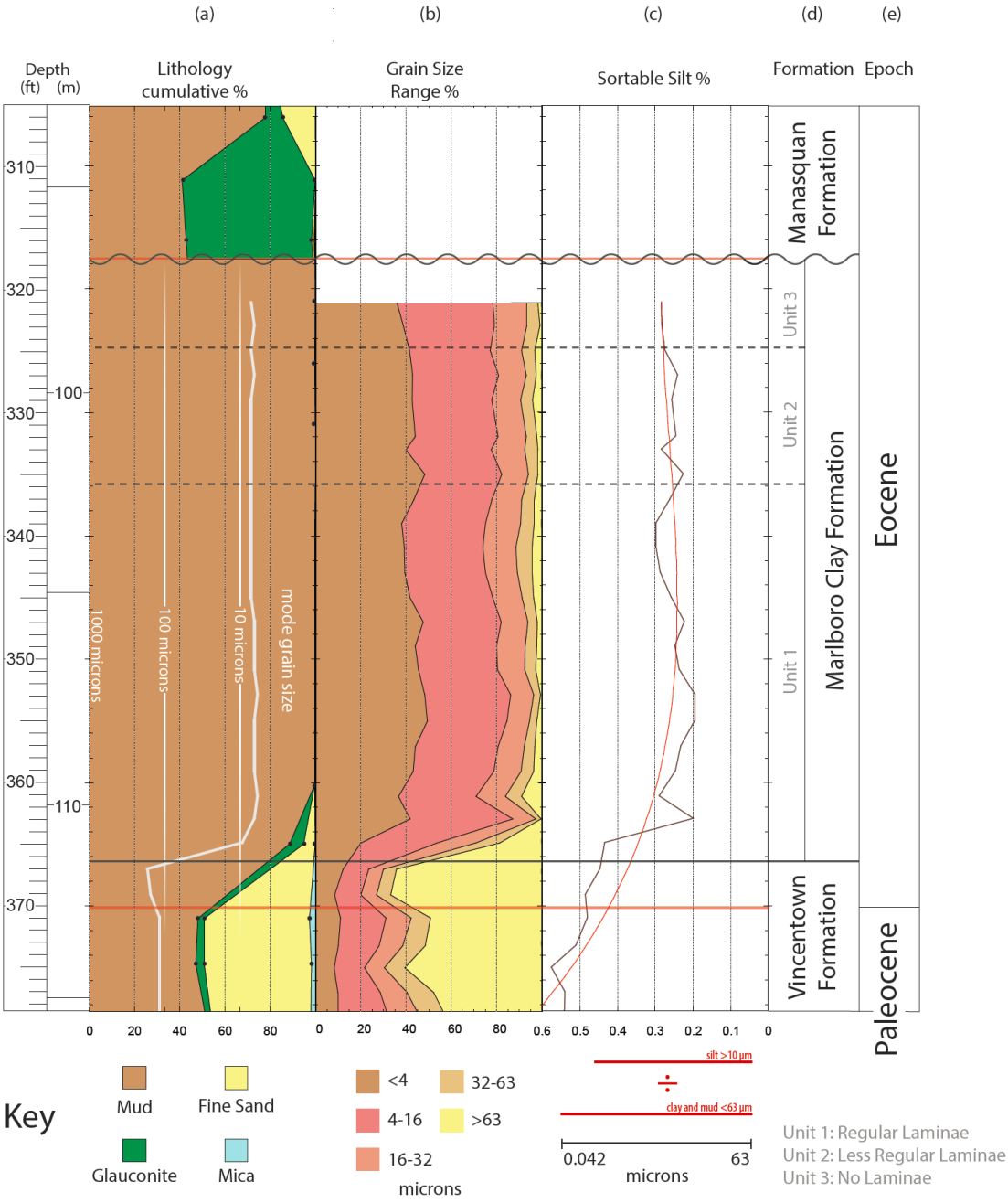

Figure 10. Grain Size and Sortable Silt Depth Plot.

Plots of grain size statistics for the Marlboro Formation that shows the vertical consistency of the section. Sortable silt shows the ratio of volume % non-cohesive mud to cohesive mud (10-63µ/<63µ ; black line) and 3rd order polynomial trend line (red) representing a possible interpretation. Cumulative lithology % column includes average (mode) grain size curve (white) on a logarithmic scale plot. Mean average is not shown.

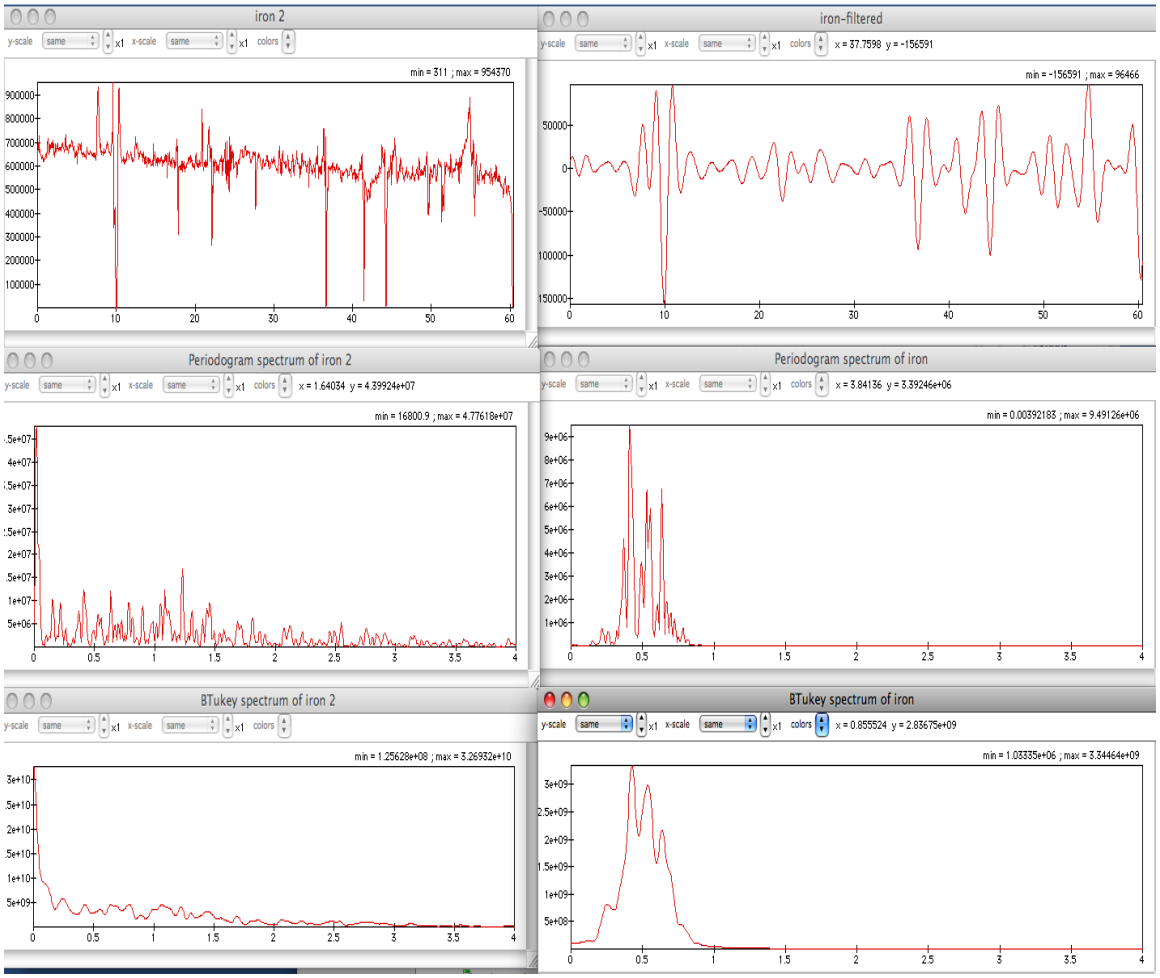

Figure 11. Spectral Analysis of Iron.

Top-left iron depth plot. Middle-left periodogram analysis of iron. Bottom-left BTukey spectrum of iron. Top-right filtered iron depth plot. Middle-right Periodogram of filtered iron. Bottom-right BTukey spectrum of filtered iron.

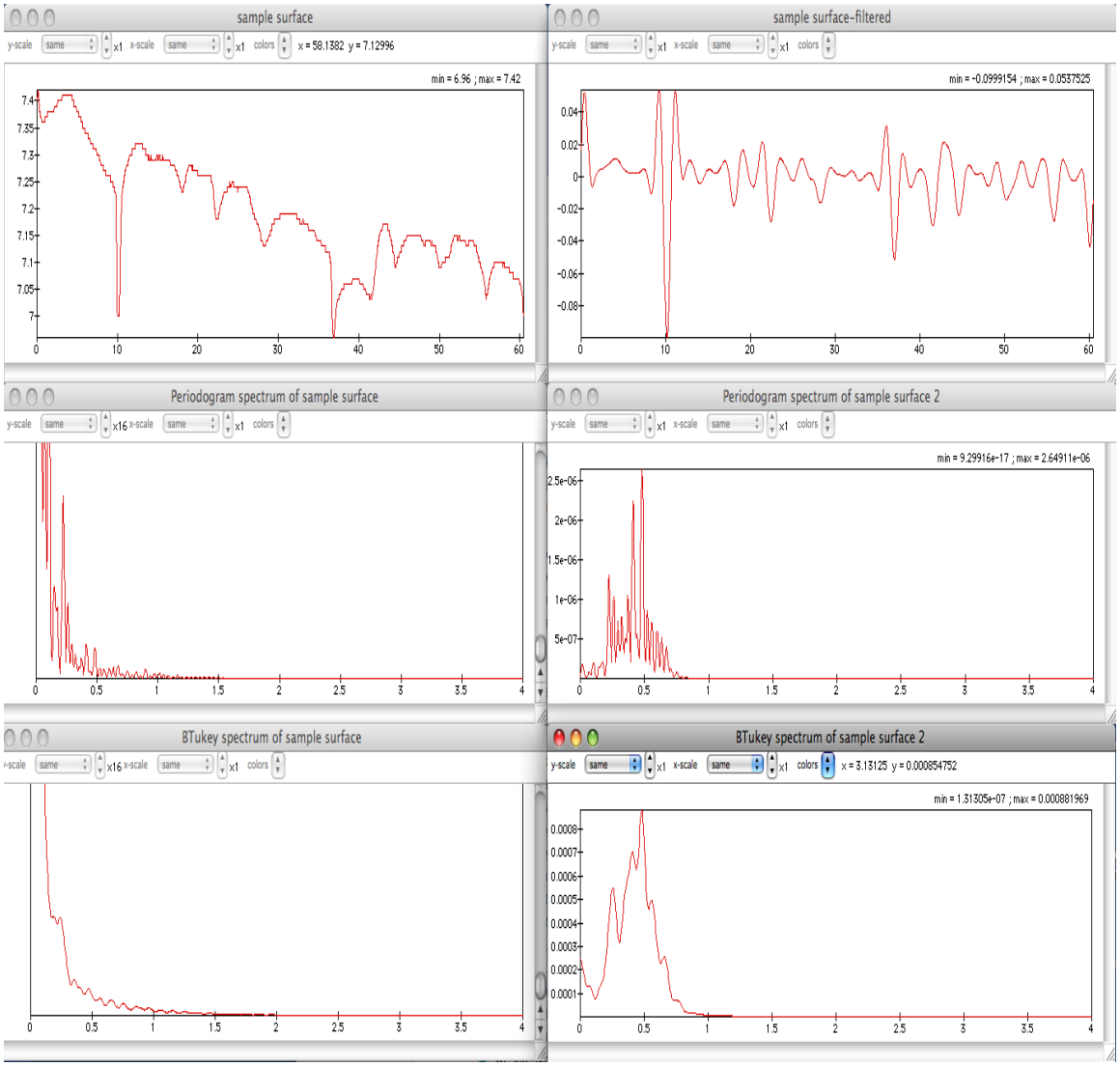

Figure 12. Spectral Analysis of sample surface.

Top-left sample surface depth plot. Middle-left periodogram analysis of sample surface. Bottom-left BTukey spectrum of sample surface. Top-right filtered sample surface depth plot. Middle-right Periodogram of filtered sample surface. Bottom-right BTukey spectrum of filtered sample surface.

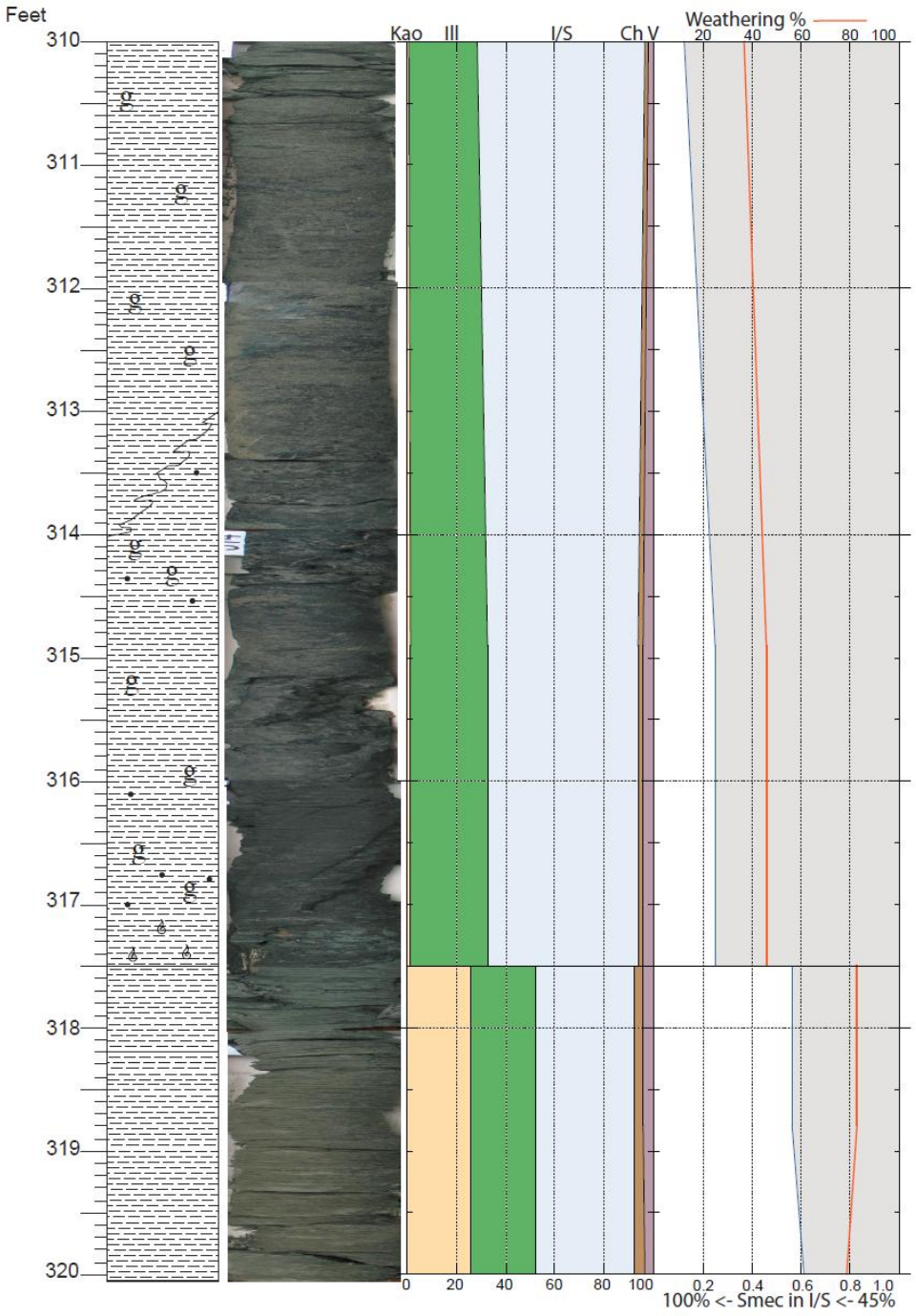

Figure 13. Barrel Sheet 310-320.

Lithologic column adapted from original on-site core descriptions. Core photographs were taken shortly after drilling and are shown here compressed. Quantitative measurement of clays obtained by XRD show kaolinite (tan) illite (green) illite/smectite (light blue), chlorite (brown), and vermiculite (purple). Horizontal lines (red) in the clay mineral column denote approximate locations of every swelling clay lamination recorded in the core. The % smectite in interlayered illite/smectite, which approximates illite alteration and sedimentation rate, is reported by the saddle ratio (right column) shaded in gray. Weathering % (orange line) is a comparison of kaolinite to chlorite to determine the relative contribution of weathering to the total clay assemblage.

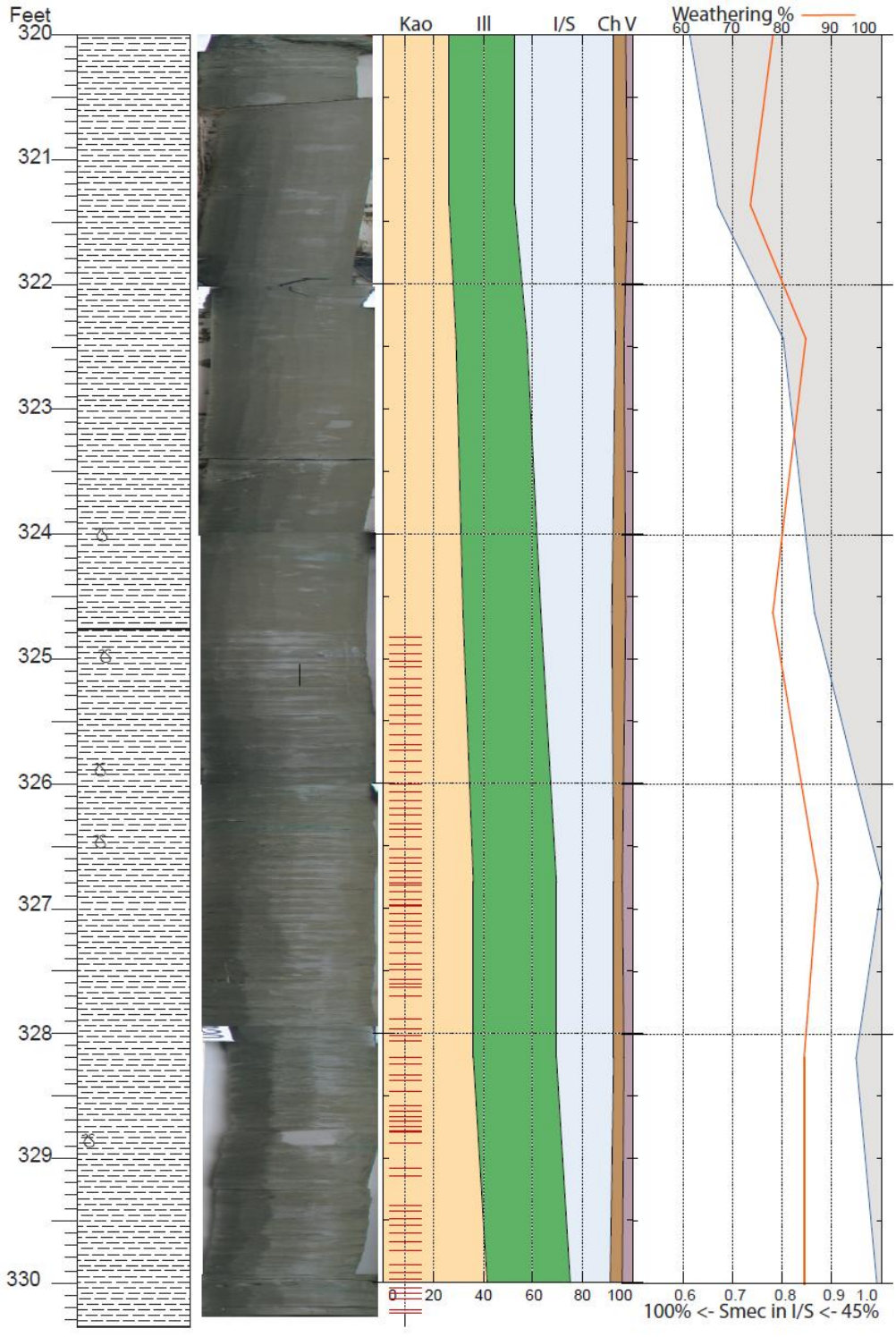

Figure 14. Barrel Sheet 320-330.

See Figure 14 Caption

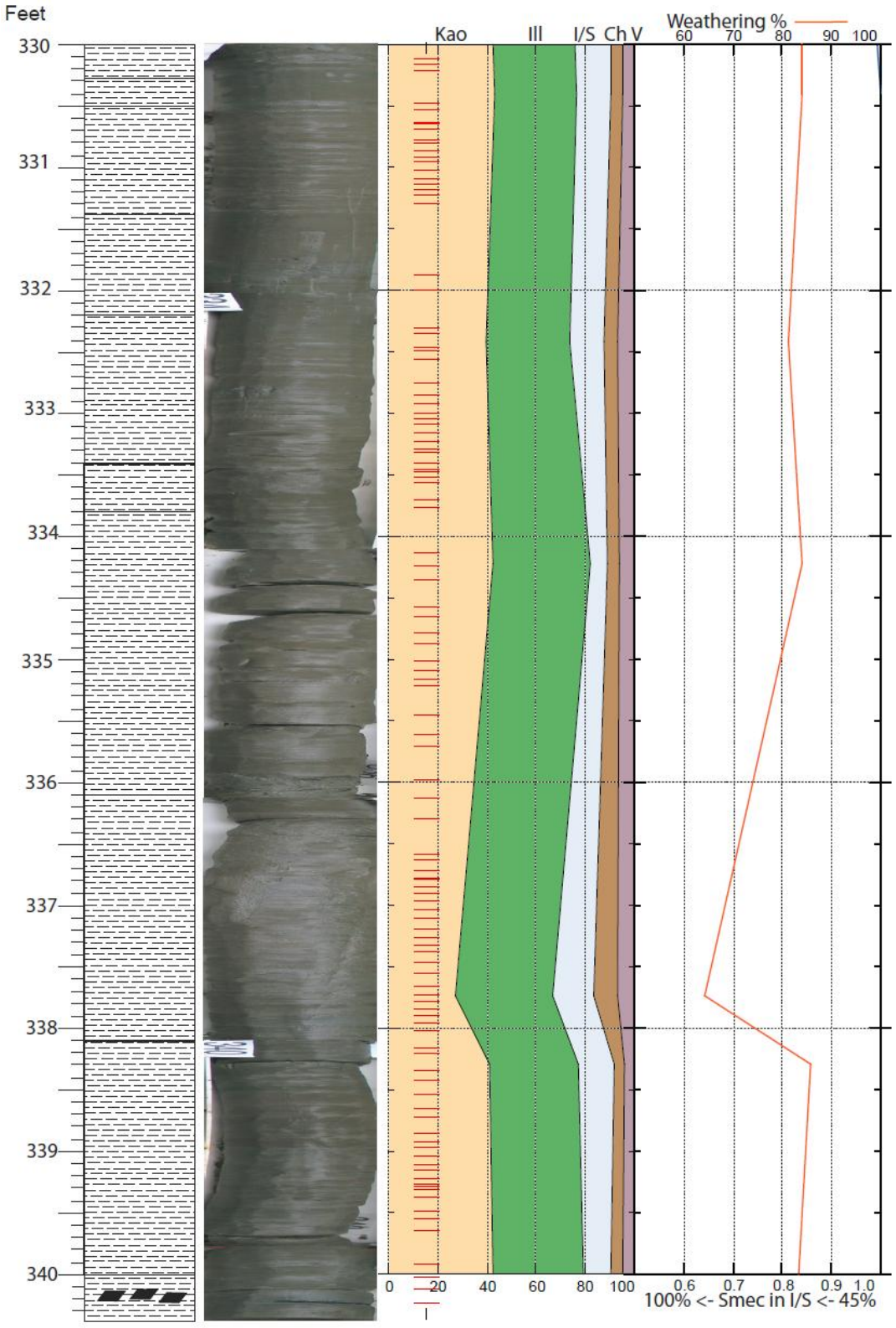

Figure 15. Barrel Sheet 330-340.

See Figure 13 Caption

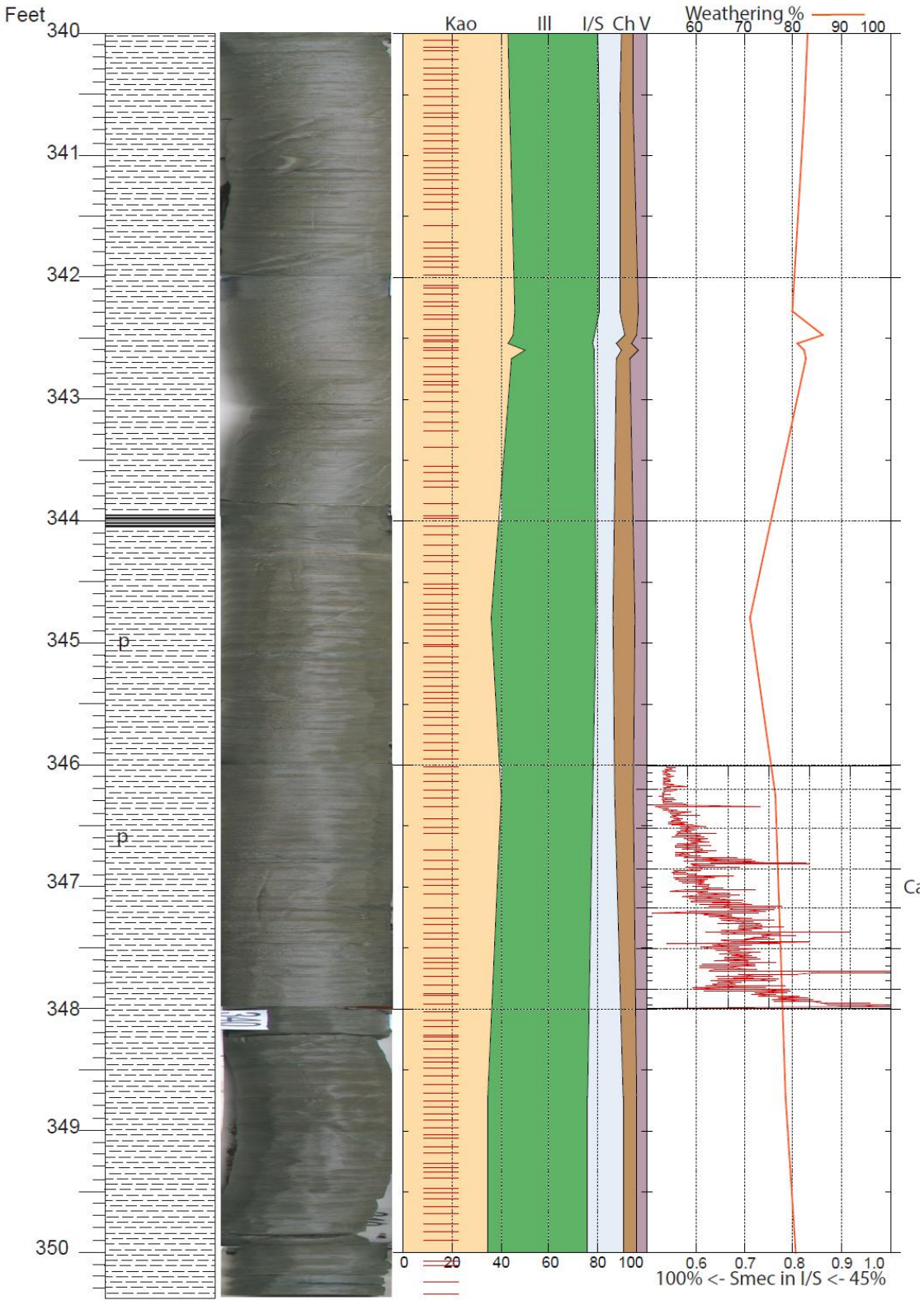

Figure 16. Barrel Sheet 340-350.

See Figure 13 Caption. Right column shows the interval scanned for XRF (red line).

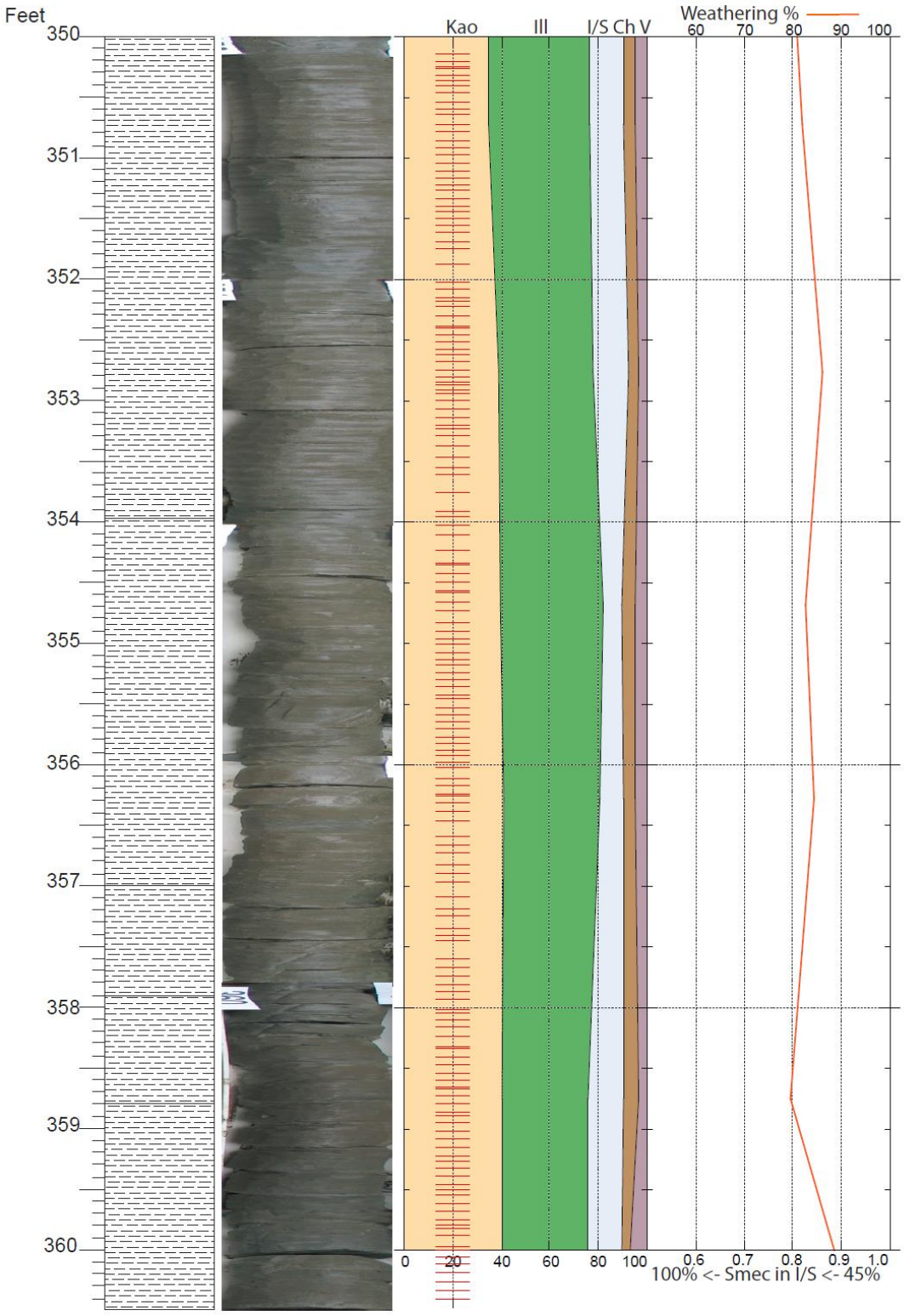

Figure 17. Barrel Sheet 350-360.

See Figure 13 Caption

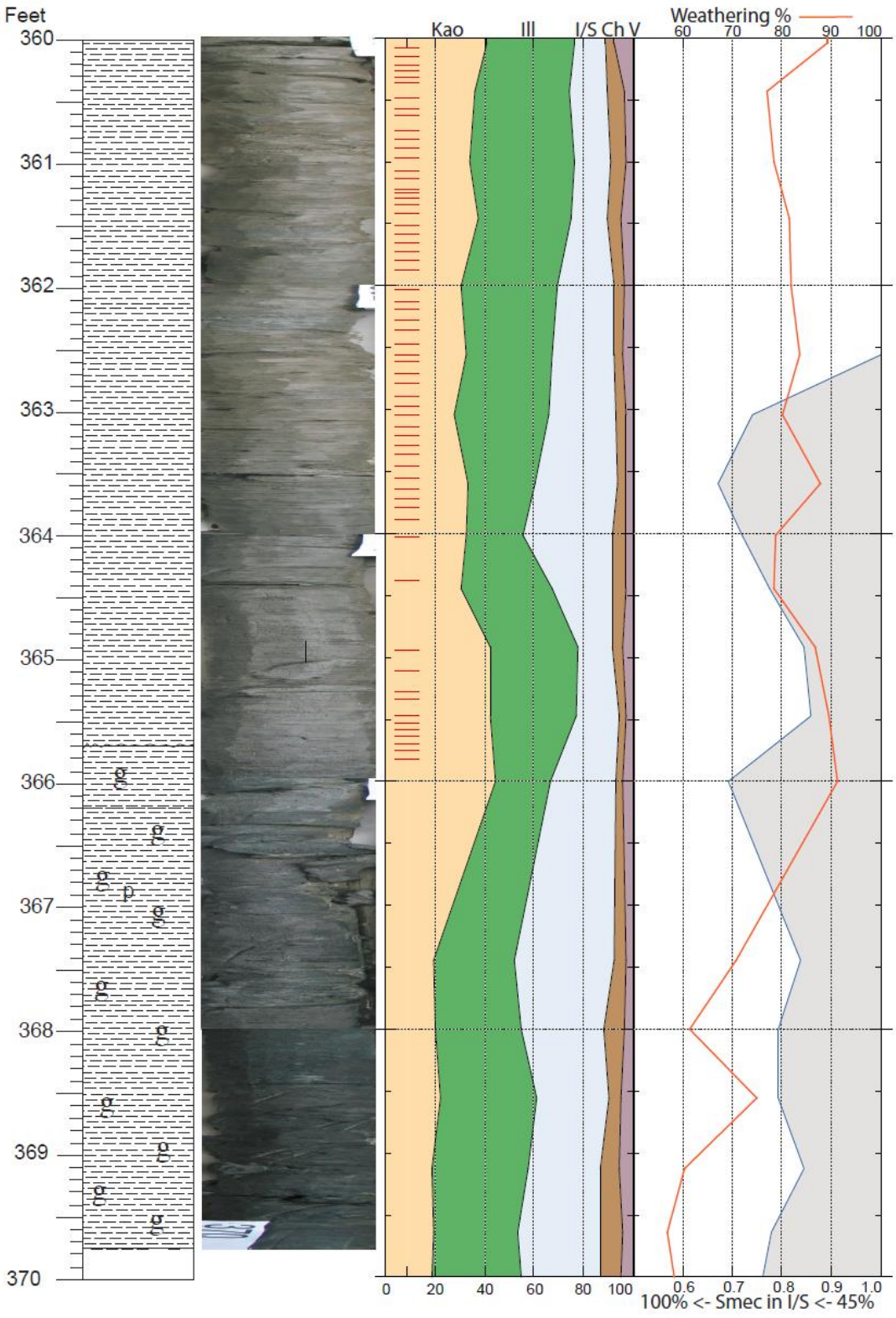

Figure 18. Barrel Sheet 360-370.

See Figure 13 Caption

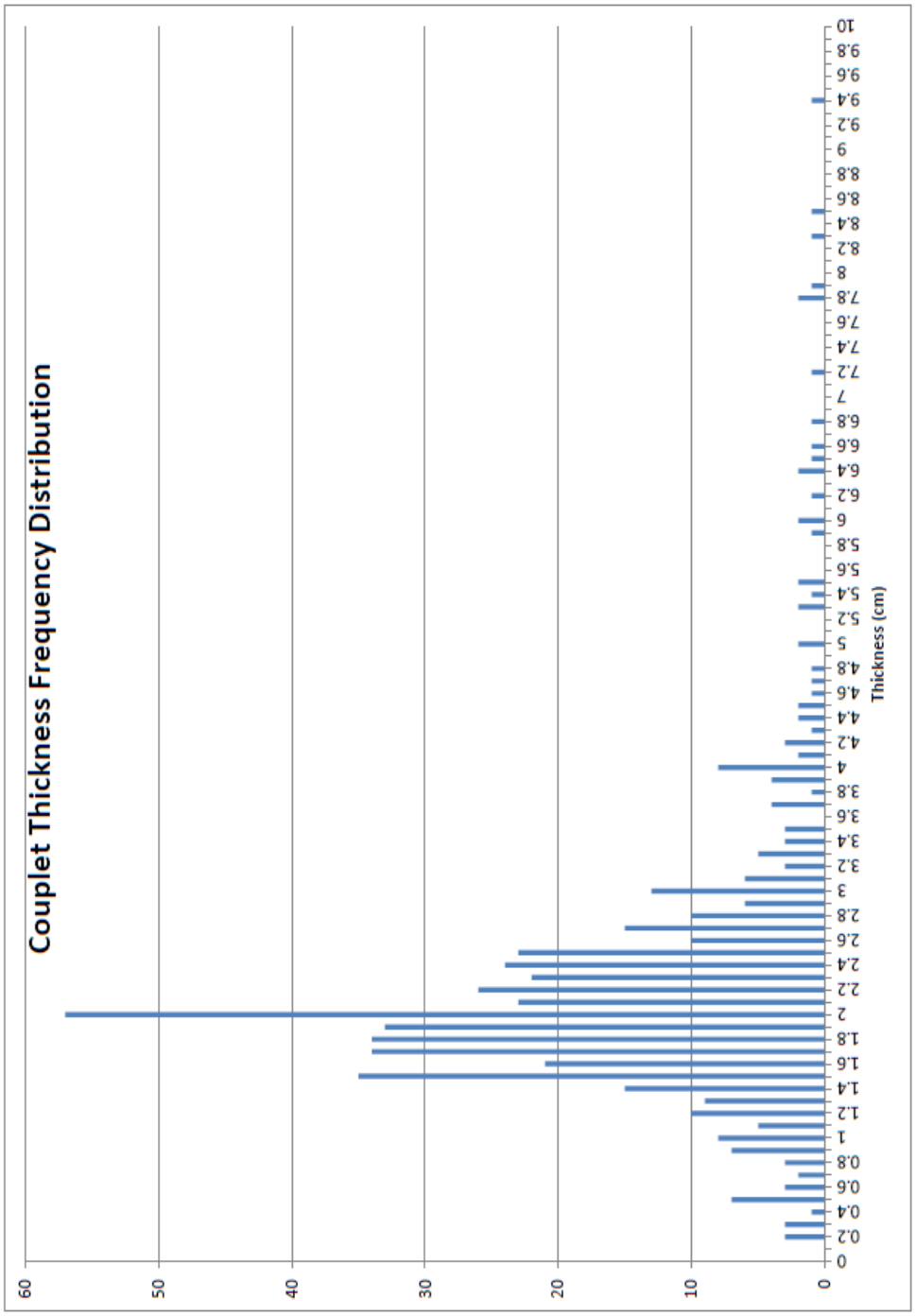

Figure 19. Couplet Thickness Frequency Distribution.

Distance between successive couplets, measured to the nearest 1 mm, used to assess the frequency of couplet sizes.

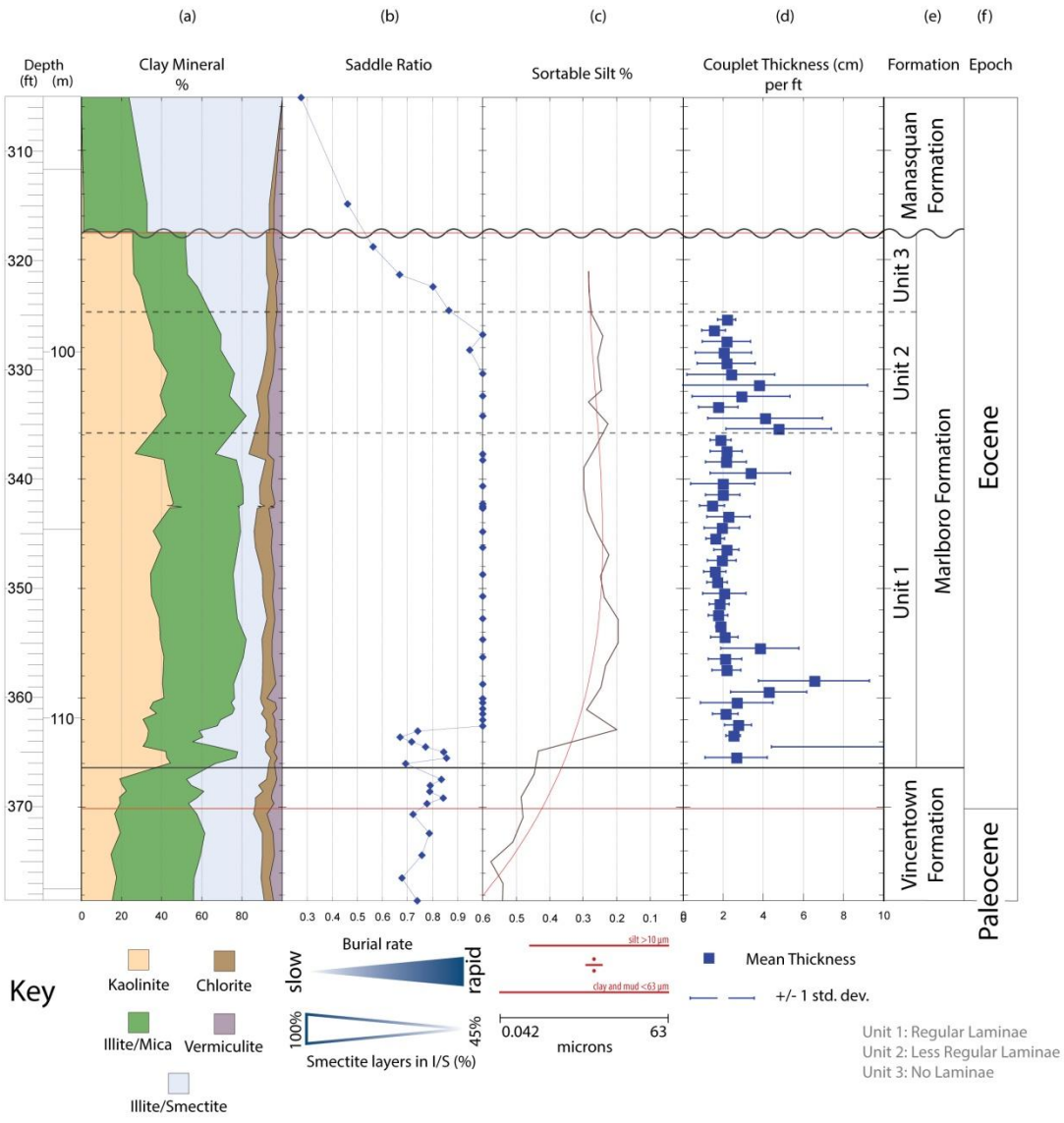

Figure 20. Determination of Depositional Units.

The Units 1-3 (e) were determined based primarily on these data sets. Changes in the abundance of kaolinite within the Marlboro Formation are distinct between Units 1 and 3 (a). The saddle ratio (b) decreases in Unit 3 compared to most of the Marlboro Formation. Sortable silt (c) shows an increasing trend towards Unit 3. Couplet thickness (d) exhibits differences between each unit: 1 (laminated), 2 (less laminated), 3 (unlaminated).

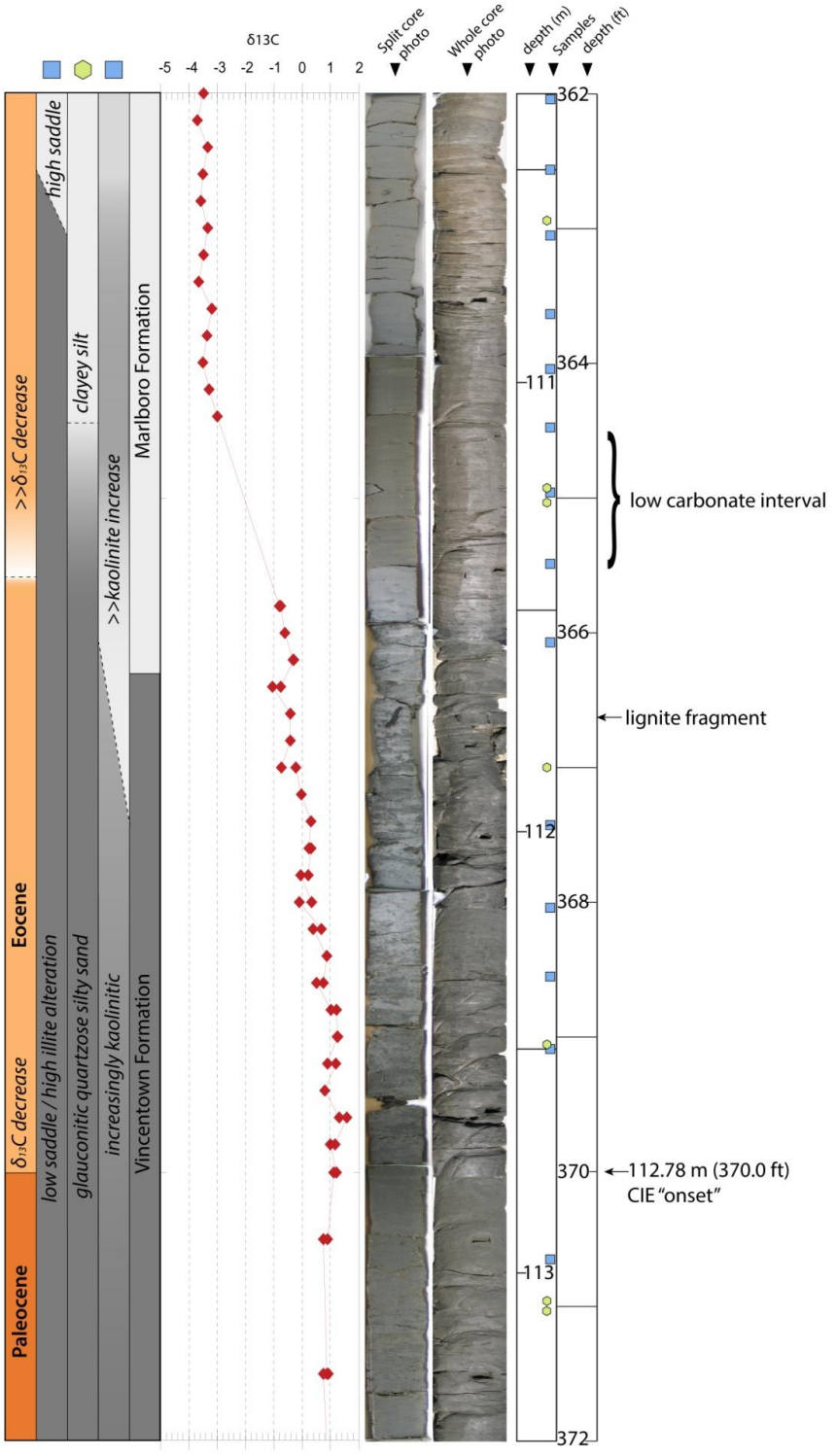

Figure 21 Vincentown Formation / Marlboro Formation Contact.

Placement of the Paleocene-Eocene boundary is based on carbon isotope data provided by J.D. Wright. The Lithologic contact with the Marlboro Formation is above the CIE, but closely corresponds with the larger carbon isotope decrease.

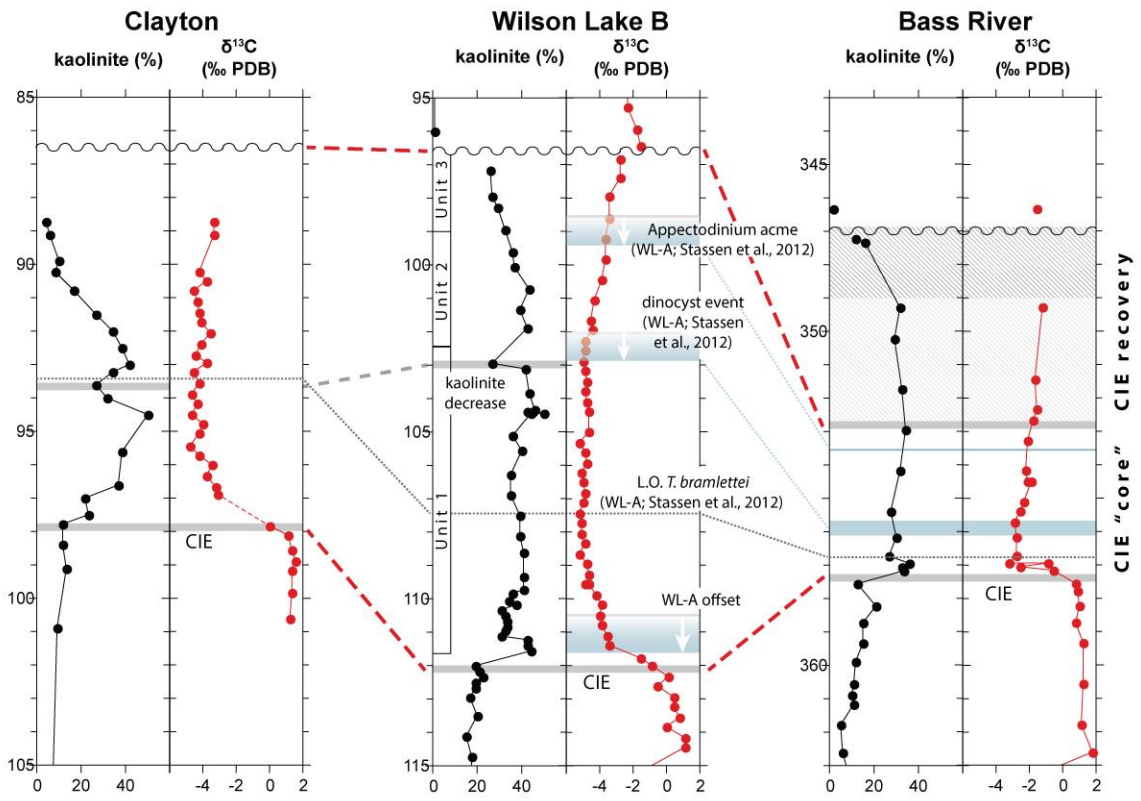

Figure 22. Regional Comparison of Clay and Isotopic Records.

Between site correlations are based on biostratigraphic determinations made by Stassen et al. (2012). Kaolinite at Wilson Lake B and Clayton shows a distinct decrease midway through the Marlboro Formation that may be coincident with a salinity change and dinocyst event recognized in Wilson Lake A. Correction for the offset between holes A and B is made based on carbon isotopes and gamma logs (not shown). Downdip Bass River shows notable condensation in the lower part of the Marlboro Formation, attributed to the "core" interval by Stassen et al. (2012). Modified after Miller et al. (2002)

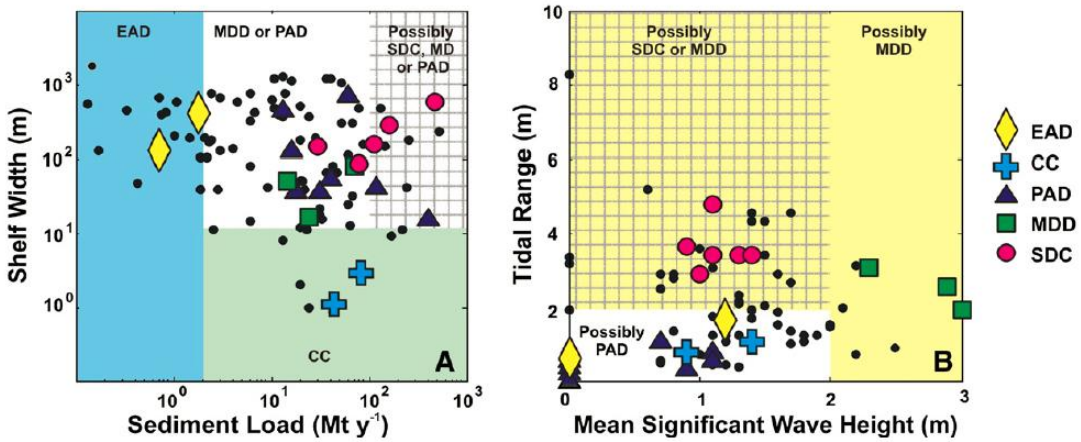

Figure 23. Mud-dominated Shelf Classification.

Scatter plots of Shelf Width, Sediment Load, Tidal Range, and Mean Significant Wave Heights used to characterize Estuarine Accumulation Dominated (EAD), Canyon Captured (CC), Proximal Accumulation Dominated (PAD), Marine Dispersal Dominated (MDD), and Subaqueous Delta Clinoform (SDC) morphologies. From Walsh and Nittrouer (2009).

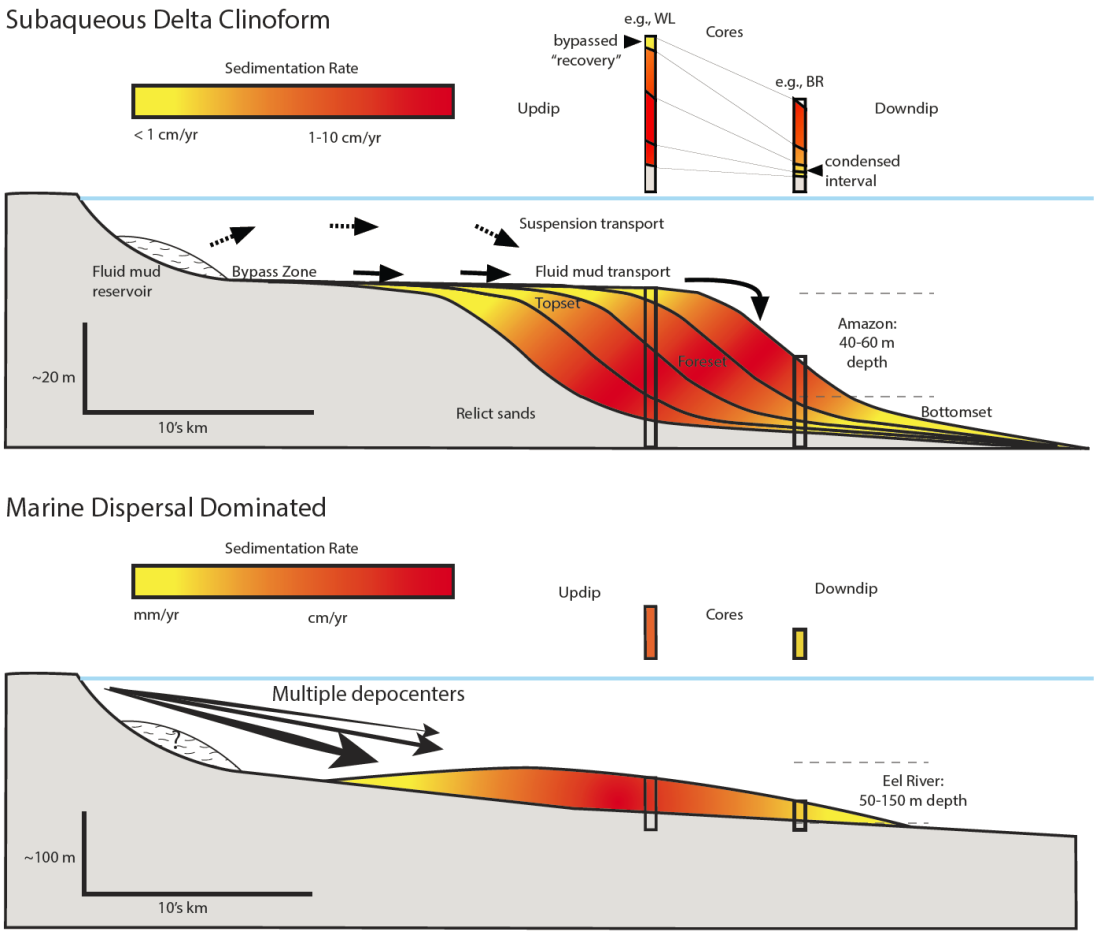

Figure 24 Muddy Shelf Depositional Models.

Shown are the processes and major depocenters in the Subaqueous Delta Clinoform and Marine Dispersal Dominated muddy shelf depositional models. Wave and tidal energies concentrate the large sediment supplied to both systems to offshore depocenters by differing methods. SDC sedimentation begins with a nearshore fluid mud reservoir that supplies sediment to clinoform regions by resuspension of sediment in the water column, or by transport in a fluid mud state along the seabed. Sedimentation rates are estimated from the Amazon River shelf. MDD systems may contain fluid mud but its importance is not well understood. Sediment pathways frequently diverge leading to multiple simultaneous depocenters that change through time. Because of the dominance of waves, MDD deposition usually happens at greater depths. Modified after Walsh and Nittrouer (2009).

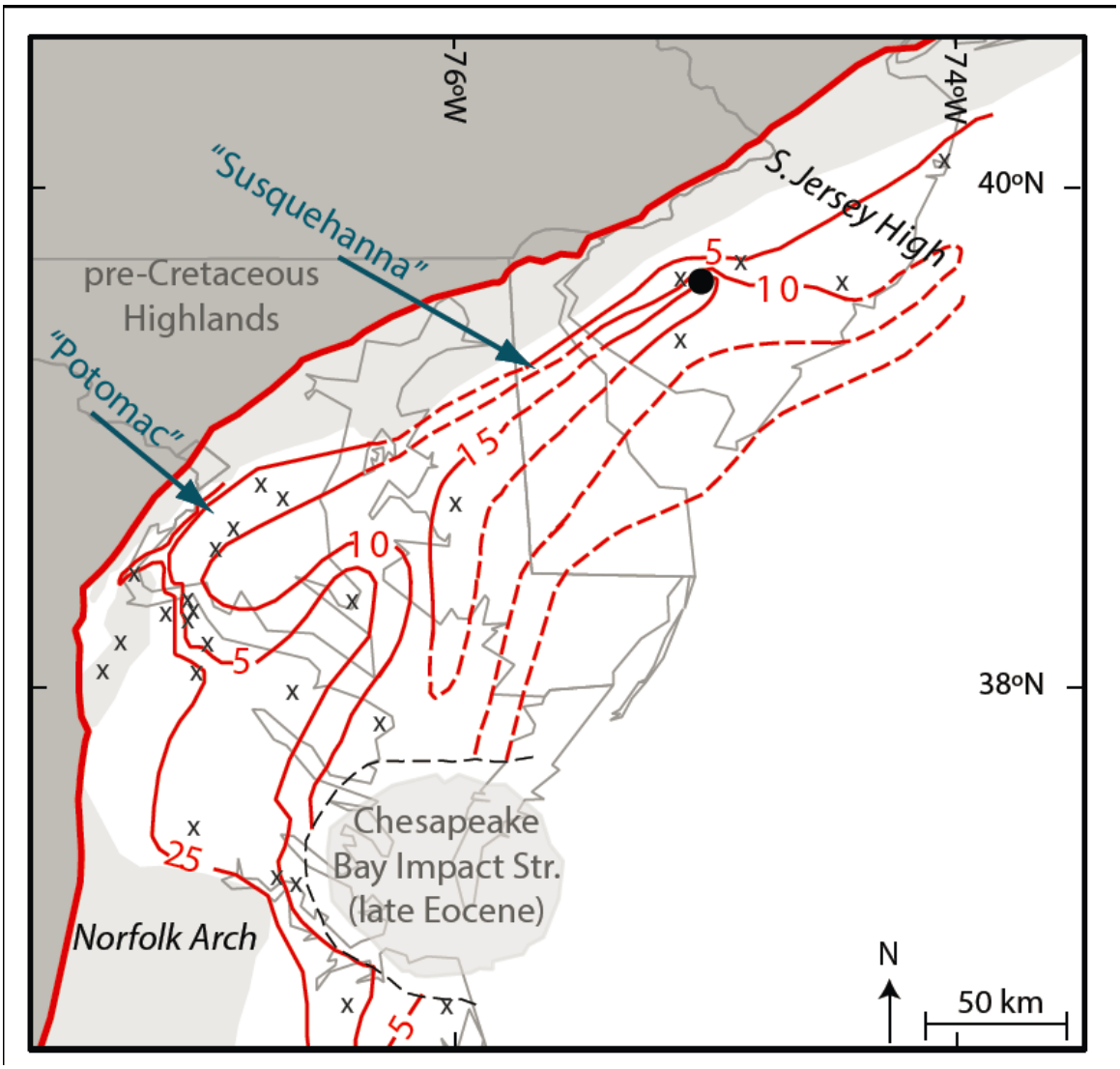

Figure 25. Isopach Map of Marlboro Formation in the Salisbury Embayment.

Contour lines are drawn based on the basement structures (labeled) and coreholes (x marks). Note that the maximum thickness of Marlboro Formation sediments would have been located offshore. Light gray shading is used where Marlboro Formation is not preserved (thickness = 0 ft). Fall line (thick red) separates pre-Cretaceous from Cenozoic strata. Possible locations of Potomac and Susquehanna river sources are shown. Modified after Kopp et al. (2009)

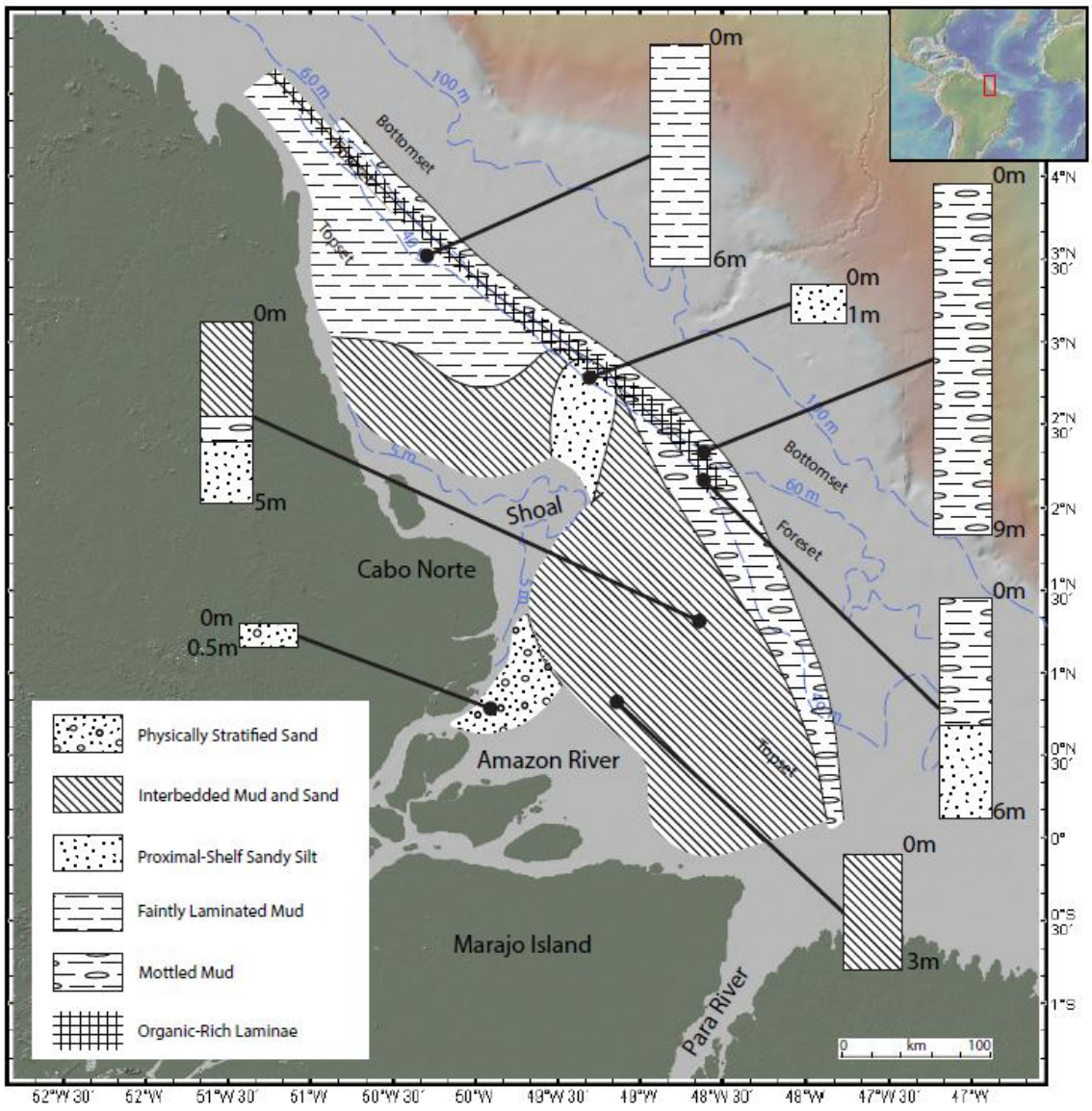

Figure 26 Amazon Shelf Sedimentary Facies.

Sedimentary facies distribution based on 121 sediment cores. Representative cores are shown for each facies. Lithologically homogenous muds analogous to the Marlboro Formation in New Jersey are found north of the Cabo Norte Shoal. A zone of organic-rich laminae is concurrent with the foreset region of the Amazon subaqueous delta. Modified after Kuehl et al. (1986b).

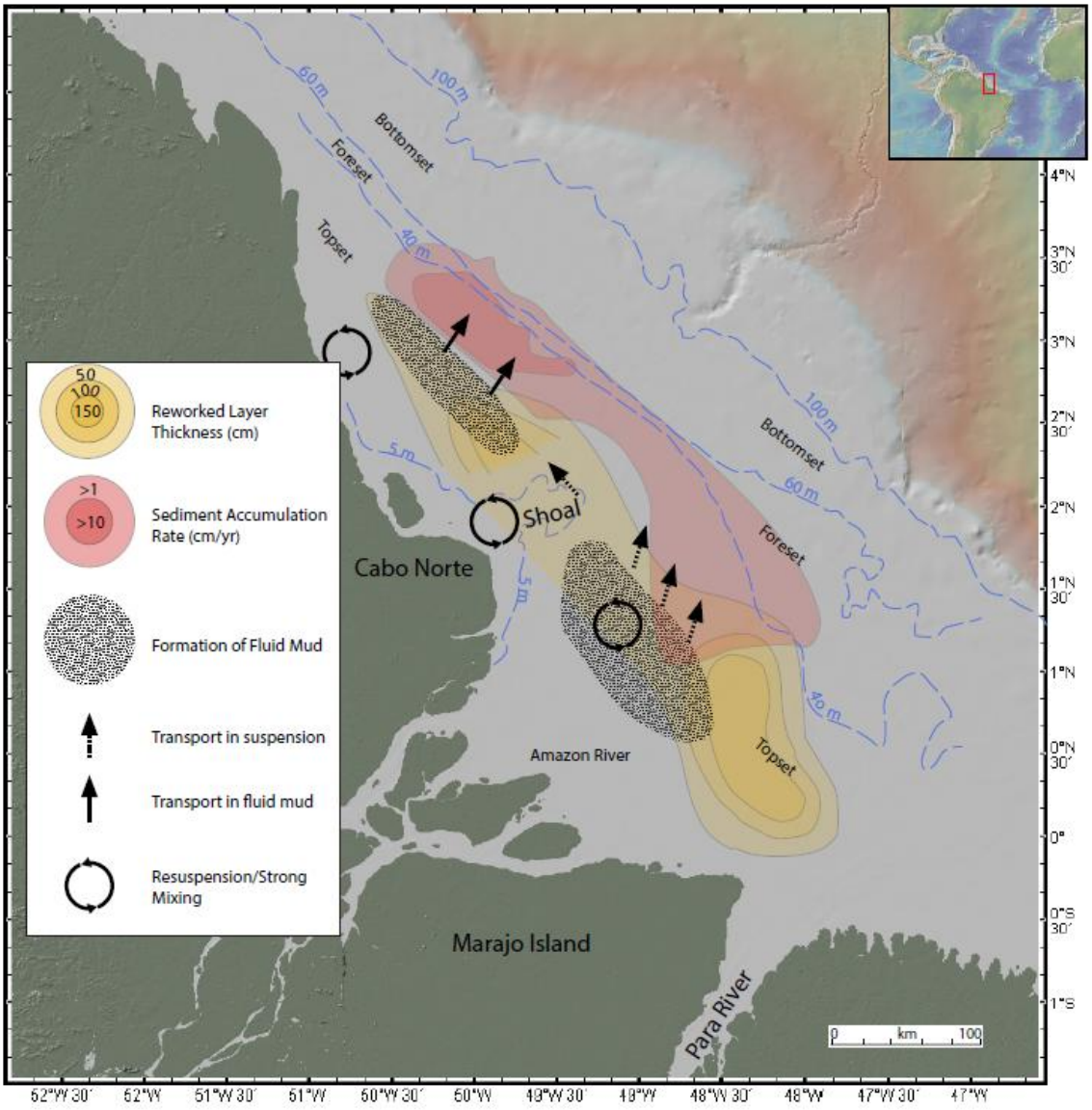

Figure 27 Amazon Shelf Processes.

Simplified illustration of the three major processes that are affecting deposition on the Amazon shelf. Reworked layer thickness shows areas of perpetual seafloor reworking and how far they penetrate in cores. Fluid mud formation areas are frequently changing with seasonal river discharge but are cleared of nearly all sediment on an annual basis. Fluid mud forms primarily from trapping river discharge and from a minor component of reworked material. Sediment accumulation occurs over most of the topset and foreset region, but shown here are highest accumulation areas. Those that receive sediment as fluid mud are the areas of highest accumulation, other areas that receive sediment in suspension from fluid mud reservoirs are slightly less so. Resuspension and strong mixing primarily affect nearshore muds, but tend to occur near fluid muds that propagate wave energy further toward land. Oceanographic conditions are the major control on these processes. Modified after Kineke et al. (1996) and Kuehl et al. (1986a).

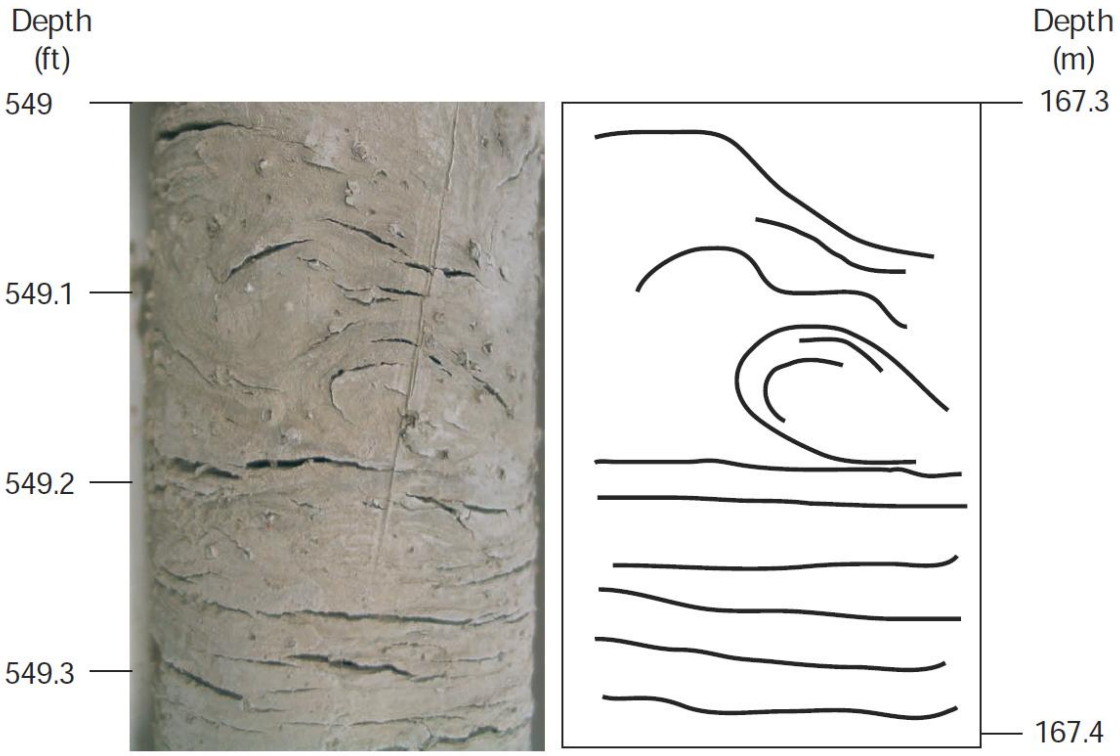

Figure 28 Convoluted bedding at Ancora.

Example of bedding found in the Marlboro Formation from Ancora (left). Drawn interpretation (right) shows possible deformation of sediment. Nothing similar was noted at Wilson Lake, but convoluted bedding may have a shared origin with 2-cm couplets. Deformation may be the result of deposition on a surface with a high angle of relief. Interval described as convoluted bedding is bounded by intervals of laminated mud. From Harris (2010).

Table 1 XRF Correlation Matrix

ELEMENT	Al	Fe	Si	Ca	Ga	P	S	Cl	Ar	K
Al	1	0.57	0.9	-0.8	0.22	0.05	-0.8	-0.1	-0.2	0.83
Fe	0.568	1	0.76	-0.2	0.46	-0	-0.2	-0.4	-0.5	0.83
Si	0.896	0.76	1	-0.6	0.37	0.03	-0.7	-0.2	-0.3	0.97
Ca	-0.75	-0.2	-0.6	1	-0	0.23	0.93	-0.1	-0.1	-0.5
Ga	0.222	0.46	0.37	-0	1	-0.2	0.06	-0.2	-0.3	0.47
P	0.053	-0	0.03	0.23	-0.2	1	-0.1	-0	-0.1	-0
S	-0.81	-0.2	-0.7	0.93	0.06	-0.1	1	-0.1	-0.1	-0.6
Cl	-0.12	-0.4	-0.2	-0.1	-0.2	-0	-0.1	1	0.8	-0.3
Ar	-0.17	-0.5	-0.3	-0.1	-0.3	-0.1	-0.1	0.8	1	-0.4
K	0.83	0.83	0.97	-0.5	0.47	-0	-0.6	-0.3	-0.4	1
Mn	0.255	0.73	0.41	0.06	0.29	0.09	0.01	-0.3	-0.5	0.46
Ti	0.404	0.16	0.38	-0.4	0.16	-0.1	-0.4	0.79	0.54	0.36
V	0.402	0.65	0.58	-0.2	0.48	-0.2	-0.1	-0.3	-0.4	0.66
Cr	0.652	0.79	0.81	-0.4	0.52	-0.2	-0.3	-0.3	-0.4	0.87
Ni	0.392	0.58	0.54	-0.1	0.37	-0.1	-0.1	-0.2	-0.3	0.58
Cu	0.498	0.25	0.49	-0.4	0.18	0.02	-0.5	-0.1	-0	0.47
Zn	0.096	0.21	0.08	-0.1	-0	-0	-0.1	0.07	-0	0.06
Ge	0.093	0.07	0.11	-0.1	0.09	-0.1	-0.1	-0	-0	0.11
As	-0.35	-0.5	-0.4	0.22	-0.2	0.08	0.2	0.64	0.51	-0.4
Se	-0.03	-0.1	-0	0.04	0.14	-0.2	0.1	0.25	0.19	0.01
Br	-0.13	-0.3	-0.2	-0.1	-0.3	-0	-0.1	0.03	0.3	-0.3
Rb	0.418	0.75	0.62	-0.1	0.64	-0.2	-0	-0.1	-0.3	0.74
Sr	-0.21	0.05	-0.1	0.66	0.02	0.73	0.39	0.01	-0.1	-0.1
Y	-0.09	-0	-0.1	0.39	-0.2	0.91	0.08	-0	-0.1	-0.1
Zr	0.441	0.63	0.61	-0.1	0.6	-0.2	-0.1	0.02	-0.2	0.71
In	-0.66	-0.2	-0.6	0.83	0.01	0.08	0.82	0.04	-0	-0.5
Sn	-0.45	-0.2	-0.4	0.55	-0	0.17	0.51	0.34	0.24	-0.4
Sb	-0.5	-0.5	-0.6	0.42	-0.2	0.1	0.39	0.86	0.67	-0.6
Ba	0.16	-0	0.11	-0.3	0.04	-0.1	-0.2	0.76	0.57	0.09
La	0.075	-0	0.04	-0.1	0.03	-0	-0.1	0.51	0.37	0.04
Ce	0.199	0.34	0.3	0.15	0.04	0.65	-0.1	-0.2	-0.3	0.3
Pr	0.378	0.46	0.45	-0.2	0.19	0.14	-0.2	-0.2	-0.3	0.47
Gd	0.289	0.38	0.32	-0.1	0.11	0.18	-0.2	-0.1	-0.2	0.32
Tb	0.131	0.55	0.31	0.17	0.26	-0	0.17	-0.2	-0.4	0.38
Tm	-0.19	0.13	-0.1	0.36	0.42	-0.1	0.38	0.04	-0.1	0
Ta	0.282	0.2	0.3	-0.3	-0.2	-0	-0.3	-0	-0.1	0.28
W	0.053	0.05	0.07	-0	0.03	-0	-0	-0	-0	0.08
Re	-0.58	-0.1	-0.5	0.8	0.04	0.08	0.78	0.09	-0	-0.4
Os	-0.01	0.15	0.07	0.14	0.11	-0.1	0.17	-0.1	-0.1	0.12
Ir	-0.05	-0	-0	0.08	-0.4	-0	0.08	0.02	0.02	-0
Au	-0.04	0.09	0.01	0.16	0.17	0.08	0.14	0.27	0.15	0.04
Pb	0.547	0.78	0.67	-0.3	0.38	-0.1	-0.3	-0.2	-0.3	0.7
Bi	0.219	0.38	0.33	-0	0.56	-0.1	0.01	0.1	-0.1	0.4
O	0.143	0.3	0.23	0.11	0.19	0.24	0.02	-0.1	-0.2	0.25
sample surf.	0.765	0.47	0.77	-0.6	0.14	0.1	-0.7	-0.1	-0.1	0.71
Mo inc	0.485	0.66	0.65	-0.2	0.59	-0.1	-0.1	0.06	-0.2	0.74
Mo Coh	0.369	0.65	0.55	0.01	0.58	-0	-0	0.08	-0.2	0.65

ELEMENT	Mn	Ti	V	Cr	Ni	Cu	Zn	Ge	As	Se
Al	0.26	0.4	0.4	0.65	0.39	0.5	0.1	0.09	-0.3	-0
Fe	0.73	0.16	0.65	0.79	0.58	0.25	0.21	0.07	-0.5	-0.1
Si	0.41	0.38	0.58	0.81	0.54	0.49	0.08	0.11	-0.4	-0
Ca	0.06	-0.4	-0.2	-0.4	-0.1	-0.4	-0.1	-0.1	0.22	0.04
Ga	0.29	0.16	0.48	0.52	0.37	0.18	-0	0.09	-0.2	0.14
P	0.09	-0.1	-0.2	-0.2	-0.1	0.02	-0	-0.1	0.08	-0.2
S	0.01	-0.4	-0.1	-0.3	-0.1	-0.5	-0.1	-0.1	0.2	0.1
Cl	-0.3	0.79	-0.3	-0.3	-0.2	-0.1	0.07	-0	0.64	0.25
Ar	-0.5	0.54	-0.4	-0.4	-0.3	-0	-0	-0	0.51	0.19
K	0.46	0.36	0.66	0.87	0.58	0.47	0.06	0.11	-0.4	0.01
Mn	1	0.01	0.39	0.48	0.34	0.05	0.05	0.03	-0.3	-0.1
Ti	0.01	1	0.13	0.31	0.17	0.25	0.09	0.06	0.34	0.26
V	0.39	0.13	1	0.65	0.41	0.19	0.06	0.09	-0.4	0.08
Cr	0.48	0.31	0.65	1	0.55	0.36	0.02	0.11	-0.4	0.07
Ni	0.34	0.17	0.41	0.55	1	0.2	-0	0.03	-0.1	0.04
Cu	0.05	0.25	0.19	0.36	0.2	1	0	0.08	-0.2	-0
Zn	0.05	0.09	0.06	0.02	-0	0	1	0.04	-0	-0
Ge	0.03	0.06	0.09	0.11	0.03	0.08	0.04	1	-0.1	0.13
As	-0.3	0.34	-0.4	-0.4	-0.1	-0.2	-0	-0.1	1	0.2
Se	-0.1	0.26	0.08	0.07	0.04	-0	-0	0.13	0.2	1
Br	-0.3	-0.1	-0.3	-0.3	-0.2	-0.1	-0	-0.1	0	-0.1
Rb	0.46	0.33	0.7	0.77	0.51	0.23	0.02	0.07	-0.3	0.24
Sr	0.18	-0.1	-0	-0.1	0.05	-0.1	-0.1	-0.1	0.16	-0
Y	0.1	-0.1	-0.2	-0.2	-0.1	-0	-0	-0.1	0.13	-0.2
Zr	0.35	0.48	0.63	0.72	0.48	0.26	-0	0.06	-0.2	0.24
In	0.04	-0.3	-0.1	-0.3	-0.1	-0.4	-0.1	-0.1	0.27	0.08
Sn	-0	0.08	-0.1	-0.3	-0.1	-0.3	-0	-0.1	0.34	0.15
Sb	-0.3	0.48	-0.4	-0.4	-0.3	-0.3	-0	-0.1	0.7	0.25
Ba	-0.1	0.79	-0	0.14	0.01	0.1	0.07	0.06	0.4	0.28
La	-0.1	0.52	-0	0.08	-0	0.06	0.07	0	0.26	0.12
Ce	0.35	-0	0.04	0.14	0.22	0.15	-0.1	-0	-0.1	-0.2
Pr	0.36	0.12	0.05	0.32	0.28	0.24	0	0.04	-0.3	-0.1
Gd	0.31	0.09	0.09	0.24	0.21	0.19	0.09	-0	-0.2	-0.1
Tb	0.43	0	0.45	0.46	0.31	0	0.09	0.05	-0.2	0.11
Tm	0.1	0.04	0.16	0.07	0.2	-0.4	-0	-0	0.09	0.19
Ta	0.11	0.14	0.13	0.24	0.12	0.11	0.08	0.11	-0.1	0.02
W	0.01	0.03	-0	0.04	0.04	0.14	0.1	0.02	-0	0.01
Re	0.1	-0.2	-0	-0.2	-0	-0.4	-0.1	-0.2	0.21	0.16
Os	0.1	0.01	0.17	0.12	0.17	-0.1	0.06	0.15	-0.1	0.23
Ir	-0	0.01	-0	-0	0.04	-0.1	-0	0.06	0	0.09
Au	0.07	0.29	0.09	0.07	0.15	-0	0.01	-0.1	0.2	0.12
Pb	0.53	0.28	0.53	0.65	0.46	0.3	0.21	0.08	-0.5	-0.1
Bi	0.26	0.36	0.4	0.41	0.34	0.11	-0	0.07	-0	0.29
O	0.27	0.08	0.21	0.21	0.22	0.08	-0	-0.1	-0.1	-0.5
sample surface	0.18	0.35	0.33	0.54	0.44	0.42	0.03	0.04	-0.2	0
Mo inc	0.37	0.53	0.63	0.73	0.51	0.27	-0	0.06	-0.1	0.22
Mo Coh	0.42	0.49	0.59	0.67	0.51	0.18	0.01	0.04	-0.1	0.23

ELEMENT	Br	Rb	Sr	Y	Zr	In	Sn	Sb	Ba	La
Al	-0.1	0.42	-0.2	-0.1	0.44	-0.7	-0.4	-0.5	0.16	0.07
Fe	-0.3	0.75	0.05	-0	0.63	-0.2	-0.2	-0.5	-0	-0
Si	-0.2	0.62	-0.1	-0.1	0.61	-0.6	-0.4	-0.6	0.11	0.04
Ca	-0.1	-0.1	0.66	0.39	-0.1	0.83	0.55	0.42	-0.3	-0.1
Ga	-0.3	0.64	0.02	-0.2	0.6	0.01	-0	-0.2	0.04	0.03
P	-0	-0.2	0.73	0.91	-0.2	0.08	0.17	0.1	-0.1	-0
S	-0.1	-0	0.39	0.08	-0.1	0.82	0.51	0.39	-0.2	-0.1
Cl	0.03	-0.1	0.01	-0	0.02	0.04	0.34	0.86	0.76	0.51
Ar	0.3	-0.3	-0.1	-0.1	-0.2	-0	0.24	0.67	0.57	0.37
K	-0.3	0.74	-0.1	-0.1	0.71	-0.5	-0.4	-0.6	0.09	0.04
Mn	-0.3	0.46	0.18	0.1	0.35	0.04	-0	-0.3	-0.1	-0.1
Ti	-0.1	0.33	-0.1	-0.1	0.48	-0.3	0.08	0.48	0.79	0.52
V	-0.3	0.7	-0	-0.2	0.63	-0.1	-0.1	-0.4	-0	-0
Cr	-0.3	0.77	-0.1	-0.2	0.72	-0.3	-0.3	-0.4	0.14	0.08
Ni	-0.2	0.51	0.05	-0.1	0.48	-0.1	-0.1	-0.3	0.01	-0
Cu	-0.1	0.23	-0.1	-0	0.26	-0.4	-0.3	-0.3	0.1	0.06
Zn	-0	0.02	-0.1	-0	-0	-0.1	-0	-0	0.07	0.07
Ge	-0.1	0.07	-0.1	-0.1	0.06	-0.1	-0.1	-0.1	0.06	0
As	0	-0.3	0.16	0.13	-0.2	0.27	0.34	0.7	0.4	0.26
Se	-0.1	0.24	-0	-0.2	0.24	0.08	0.15	0.25	0.28	0.12
Br	1	-0.4	-0.2	-0.1	-0.4	-0.1	-0.1	-0	-0.1	-0
Rb	-0.4	1	0.13	-0.2	0.93	-0	-0.1	-0.2	0.17	0.07
Sr	-0.2	0.13	1	0.85	0.15	0.48	0.44	0.33	-0.1	-0
Y	-0.1	-0.2	0.85	1	-0.1	0.23	0.26	0.18	-0.1	-0
Zr	-0.4	0.93	0.15	-0.1	1	-0	-0	-0.1	0.3	0.15
In	-0.1	-0	0.48	0.23	-0	1	0.2	0.44	-0.1	-0.1
Sn	-0.1	-0.1	0.44	0.26	-0	0.2	1	0.58	0.13	0.14
Sb	-0	-0.2	0.33	0.18	-0.1	0.44	0.58	1	0.55	0.39
Ba	-0.1	0.17	-0.1	-0.1	0.3	-0.1	0.13	0.55	1	0.45
La	-0	0.07	-0	-0	0.15	-0.1	0.14	0.39	0.45	1
Ce	-0.2	0.16	0.59	0.67	0.16	0.02	0.06	-0.1	-0.3	-0
Pr	-0.2	0.31	0.09	0.13	0.29	-0.2	-0.2	-0.3	-0.1	-0.3
Gd	-0.1	0.18	0.1	0.16	0.15	-0.2	-0.1	-0.2	-0	0.01
Tb	-0.3	0.56	0.22	0.02	0.49	0.24	-0.1	-0.1	0.05	-0
Tm	-0.1	0.33	0.28	0.04	0.32	0.26	0.35	0.21	0.02	0.04
Ta	-0	0.11	-0.1	-0.1	0.11	-0.2	-0.2	-0.2	0.13	0.01
W	-0	0.01	-0	-0	-0	-0	-0	-0	0	0.04
Re	-0.1	0.06	0.51	0.22	0.03	0.7	0.54	0.47	-0	-0
Os	-0.1	0.19	0.06	-0.1	0.16	0.12	0.09	0.01	0.06	-0
Ir	-0	-0	0.03	-0	-0	0.06	0.09	0.07	0.02	-0
Au	-0.1	0.19	0.24	0.11	0.23	0.16	0.25	0.32	0.24	0.13
Pb	-0.2	0.61	-0.1	-0.2	0.53	-0.3	-0.2	-0.3	0.11	0.06
Bi	-0.2	0.54	0.12	-0.1	0.56	0.02	0.09	0.06	0.25	0.17
O	-0.1	0.17	0.32	0.28	0.24	0.06	0.07	-0	-0	0.01
sample surface	-0	0.32	-0.1	-0	0.38	-0.6	-0.4	-0.4	0.13	0.06
Mo inc	-0.4	0.92	0.2	-0	0.96	-0.1	-0	-0.1	0.33	0.18
Mo Coh	-0.4	0.9	0.34	0.06	0.94	0.06	0.09	0.05	0.31	0.18

ELEMENT	Ce	Pr	Gd	Tb	Tm	Ta	W	Re	Os	Ir
Al	0.2	0.38	0.29	0.13	-0.2	0.28	0.05	-0.6	-0	-0.1
Fe	0.34	0.46	0.38	0.55	0.13	0.2	0.05	-0.1	0.15	-0
Si	0.3	0.45	0.32	0.31	-0.1	0.3	0.07	-0.5	0.07	-0
Ca	0.15	-0.2	-0.1	0.17	0.36	-0.3	-0	0.8	0.14	0.08
Ga	0.04	0.19	0.11	0.26	0.42	-0.2	0.03	0.04	0.11	-0.4
P	0.65	0.14	0.18	-0	-0.1	-0	-0	0.08	-0.1	-0
S	-0.1	-0.2	-0.2	0.17	0.38	-0.3	-0	0.78	0.17	0.08
Cl	-0.2	-0.2	-0.1	-0.2	0.04	-0	-0	0.09	-0.1	0.02
Ar	-0.3	-0.3	-0.2	-0.4	-0.1	-0.1	-0	-0	-0.1	0.02
K	0.3	0.47	0.32	0.38	0	0.28	0.08	-0.4	0.12	-0
Mn	0.35	0.36	0.31	0.43	0.1	0.11	0.01	0.1	0.1	-0
Ti	-0	0.12	0.09	0	0.04	0.14	0.03	-0.2	0.01	0.01
V	0.04	0.05	0.09	0.45	0.16	0.13	-0	-0	0.17	-0
Cr	0.14	0.32	0.24	0.46	0.07	0.24	0.04	-0.2	0.12	-0
Ni	0.22	0.28	0.21	0.31	0.2	0.12	0.04	-0	0.17	0.04
Cu	0.15	0.24	0.19	0	-0.4	0.11	0.14	-0.4	-0.1	-0.1
Zn	-0.1	0	0.09	0.09	-0	0.08	0.1	-0.1	0.06	-0
Ge	-0	0.04	-0	0.05	-0	0.11	0.02	-0.2	0.15	0.06
As	-0.1	-0.3	-0.2	-0.2	0.09	-0.1	-0	0.21	-0.1	0
Se	-0.2	-0.1	-0.1	0.11	0.19	0.02	0.01	0.16	0.23	0.09
Br	-0.2	-0.2	-0.1	-0.3	-0.1	-0	-0	-0.1	-0.1	-0
Rb	0.16	0.31	0.18	0.56	0.33	0.11	0.01	0.06	0.19	-0
Sr	0.59	0.09	0.1	0.22	0.28	-0.1	-0	0.51	0.06	0.03
Y	0.67	0.13	0.16	0.02	0.04	-0.1	-0	0.22	-0.1	-0
Zr	0.16	0.29	0.15	0.49	0.32	0.11	-0	0.03	0.16	-0
In	0.02	-0.2	-0.2	0.24	0.26	-0.2	-0	0.7	0.12	0.06
Sn	0.06	-0.2	-0.1	-0.1	0.35	-0.2	-0	0.54	0.09	0.09
Sb	-0.1	-0.3	-0.2	-0.1	0.21	-0.2	-0	0.47	0.01	0.07
Ba	-0.3	-0.1	-0	0.05	0.02	0.13	0	-0	0.06	0.02
La	-0	-0.3	0.01	-0	0.04	0.01	0.04	-0	-0	-0
Ce	1	0.48	0.33	0.15	0.04	0.05	0.06	0.07	0.01	0.02
Pr	0.48	1	0.44	0.08	0.02	0.13	0.1	-0.1	0.1	0.03
Gd	0.33	0.44	1	-0	-0	0.08	0.05	-0.1	-0	-0.1
Tb	0.15	0.08	-0	1	0.03	0.29	-0	0.24	0.26	0.13
Tm	0.04	0.02	-0	0.03	1	-0.5	-0.1	0.42	0.22	-0
Ta	0.05	0.13	0.08	0.29	-0.5	1	0.14	-0.2	0.14	0.25
W	0.06	0.1	0.05	-0	-0.1	0.14	1	-0	0.15	0.13
Re	0.07	-0.1	-0.1	0.24	0.42	-0.2	-0	1	0.27	0.17
Os	0.01	0.1	-0	0.26	0.22	0.14	0.15	0.27	1	0.23
Ir	0.02	0.03	-0.1	0.13	-0	0.25	0.13	0.17	0.23	1
Au	0.04	-0.1	-0	0.16	0.28	-0.1	-0.2	0.35	0.19	0.09
Pb	0.17	0.34	0.29	0.41	0.07	0.19	0.03	-0.1	0.17	-0
Bi	0.06	0.11	0.07	0.27	0.35	-0	-0	0.19	0.27	-0.2
O	0.29	0.2	0.14	0.15	0.18	0.03	0.01	0.22	0.15	0.01
sample surface	0.21	0.32	0.22	0.15	-0.1	0.24	0.02	-0.5	-0	-0
Mo inc	0.23	0.32	0.18	0.49	0.32	0.11	-0	0.01	0.15	-0
Mo Coh	0.27	0.31	0.19	0.51	0.4	0.07	-0	0.15	0.18	-0

ELEMENT	Au	Pb	Bi	Po
Al	-0	0.55	0.22	0.14
Fe	0.09	0.78	0.38	0.3
Si	0.01	0.67	0.33	0.23
Ca	0.16	-0.3	-0	0.11
Ga	0.17	0.38	0.56	0.19
P	0.08	-0.1	-0.1	0.24
S	0.14	-0.3	0.01	0.02
Cl	0.27	-0.2	0.1	-0.1
Ar	0.15	-0.3	-0.1	-0.2
K	0.04	0.7	0.4	0.25
Mn	0.07	0.53	0.26	0.27
Ti	0.29	0.28	0.36	0.08
V	0.09	0.53	0.4	0.21
Cr	0.07	0.65	0.41	0.21
Ni	0.15	0.46	0.34	0.22
Cu	-0	0.3	0.11	0.08
Zn	0.01	0.21	-0	-0
Ge	-0.1	0.08	0.07	-0.1
As	0.2	-0.5	-0	-0.1
Se	0.12	-0.1	0.29	-0.5
Br	-0.1	-0.2	-0.2	-0.1
Rb	0.19	0.61	0.54	0.17
Sr	0.24	-0.1	0.12	0.32
Y	0.11	-0.2	-0.1	0.28
Zr	0.23	0.53	0.56	0.24
In	0.16	-0.3	0.02	0.06
Sn	0.25	-0.2	0.09	0.07
Sb	0.32	-0.3	0.06	-0
Ba	0.24	0.11	0.25	-0
La	0.13	0.06	0.17	0.01
Ce	0.04	0.17	0.06	0.29
Pr	-0.1	0.34	0.11	0.2
Gd	-0	0.29	0.07	0.14
Tb	0.16	0.41	0.27	0.15
Tm	0.28	0.07	0.35	0.18
Ta	-0.1	0.19	-0	0.03
W	-0.2	0.03	-0	0.01
Re	0.35	-0.1	0.19	0.22
Os	0.19	0.17	0.27	0.15
Ir	0.09	-0	-0.2	0.01
Au	1	0.15	0.33	0.25
Pb	0.15	1	0.41	0.3
Bi	0.33	0.41	1	0.23
O	0.25	0.3	0.23	1
sample surface	-0	0.47	0.23	0.15
Mo inc	0.26	0.55	0.59	0.29
Mo Coh	0.31	0.51	0.59	0.32